DEPARTMENT OF PHYSICS
UNIVERSITY OF JYVÄSKYLÄ
RESEARCH REPORT No. 8/2017

Discovery of the new isotopes ^{240}Es and ^{236}Bk and in-beam spectroscopic studies of ^{244}Cf

by

Joonas Konki

Academic Dissertation
for the Degree of
Doctor of Philosophy

To be presented, by permission of the
Faculty of Mathematics and Science
of the University of Jyväskylä,
for public examination in Auditorium FYS1 of the
University of Jyväskylä on December 18, 2017
at 12 o'clock noon

Jyväskylä, Finland
December 2017

Abstract

Konki, Joonas
Discovery of the new isotopes ^{240}Es and ^{236}Bk and in-beam spectroscopic studies of ^{244}Cf
Jyväskylä: University of Jyväskylä, 2017, 95 p.
Department of Physics Research Report No. 8/2017
ISSN: 0075-465X; 8/2017
ISBN: 978-951-39-7290-5 (paper version)
ISBN: 978-951-39-7291-2 (electronic version)
Diss.

The hitherto unknown neutron-deficient nuclei ^{240}Es and ^{236}Bk were synthesised using the fusion-evaporation reaction ^{209}Bi(^{34}S,3n)^{240}Es. The RITU gas-filled recoil separator and the GREAT spectrometer were used in this decay spectroscopic study. The measured electron-capture delayed fission (ECDF) branches in both of the new isotopes complement the experimental data available in the heavier odd-odd Es and Bk isotopes. Furthermore, the ECDF branches show a continuation in the exponential increase of the ECDF probabilities as a function of $Q_{\mathrm{EC}} - B_{\mathrm{sf}}$ when approaching the proton dripline. In addition, an in-beam γ-ray spectroscopic study of the neutron-deficient isotope ^{244}Cf was made using the fusion-evaporation reaction ^{198}Pt(^{48}Ca,2n)^{244}Cf. The JUROGAMII array coupled to RITU and GREAT was used to detect the prompt γ rays emitted at the target position. The excited states in ^{244}Cf were studied for the first time using the recoil-decay tagging method. The ground-state rotational band of ^{244}Cf was measured up to a tentative spin and parity of $I^{\pi} = 20^{+}$. The behaviour of the moments of inertia revealed an up-bend due to a possible alignment of coupled nucleons in high-j orbitals starting at a rotational frequency of about $\hbar\omega = 0.2$ MeV. The results were compared to the systematic behaviour of the heavy even-even $N = 146$ isotones as well as to theoretical calculations where available.

Keywords: decay spectroscopy, in-beam spectroscopy, nuclear structure, electron-capture delayed fission, recoil-decay tagging, neutron-deficient nuclei

Author Joonas Konki
Department of Physics
University of Jyväskylä
Finland

Supervisor Prof. Paul Greenlees
Department of Physics
University of Jyväskylä
Finland

Reviewers Prof. Piet Van Duppen
Instituut voor Kern- en Stralingsfysica
Departement Natuurkunde en Sterrenkunde
KU Leuven
Belgium

Prof. Zsolt Podolyák
Department of Physics
University of Surrey
United Kingdom

Opponent Prof. Dirk Rudolph
Department of Physics
Lund University
Sweden

Preface

This work has been carried out at the Accelerator Laboratory, Department of Physics, University of Jyväskylä, Finland in 2012–2017. Financial support from the Alfred Kordelin Foundation (2015, 2016), the Rector of the University of Jyväskylä and the Academy of Finland under the Doctoral Programme in PArticle and NUclear Physics and the Finnish Center of Excellence Programme is gratefully acknowledged.

The endeavour throughout a project such as this thesis, my studies, the experiments and life in general would not have been possible without the assistance and support of many people.

First of all, I want to thank my supervisor Prof. Paul Greenlees who introduced me to the challenges of experimental nuclear physics in the first place and his continuous efforts, guidance and encouragement throughout the years. I would also like to thank Dr. Jadambaa Khuyagbaatar for the numerous fruitful discussions, his guidance and input to the analysis and interpretation of the results related to the synthesis of the two new isotopes. Warm thanks also go to Dr. Barbara Sulignano for her help and guidance during the preparation, experiment and analysis phases of the in-beam study.

I would like to thank all of the past and present colleagues in the Nuclear Spectroscopy research group whom I had the privilege to work with and for being always willing to help. Special thanks go to Dr. Panu Rahkila for being a mentor in the matters of data acquisition and computing. Thanks to Dr. Juha Uusitalo and Dr. Catherine Scholey for your enthusiasm for explaining things in order to spread the knowledge. Thanks also to Dr. Sanna Stolze, Dr. Kalle Auranen, Mr. Jari Partanen and Mr. Hussam Badran among others for the pleasant company and for the times well spent while working in the lab.

I want to thank the pre-examiners, Prof. Piet Van Duppen and Prof. Zsolt Podolyák, for the careful reading of the manuscript. Gratitude also goes to Dr. Mikael Sandzelius for proof-reading the manuscript and the good atmosphere while sharing the same office.

Kiitokset rakkaille vanhemmilleni, siskoilleni ja isovanhemmilleni loputtomasta tuesta ja kannustuksesta. Suuret kiitokset kuuluvat myös kaikille ystävilleni monista yhteisistä kokemuksista vuosien varrella. Viimeisenä, mutta vähintäänkin tärkeimpänä, kiitos rakas Milka kaikesta.

Joonas Konki,
Jyväskylä, December 2017

List of publications

The author has been involved in carrying out the experiments, wrote the proposal for the in-beam study of ^{244}Cf that was accepted by the JYFL Programme Advisory Committee (JYFL-PAC) and acted as the co-spokesperson, performed the analysis of the experimental data and acted as the main author in the writing process of the articles. The main results of this thesis have been reported in two scientific publications:

1. *Towards saturation of the electron-capture delayed fission probability: The new isotopes ^{240}Es and ^{236}Bk*
   J. Konki, J. Khuyagbaatar, J. Uusitalo, P.T. Greenlees, K. Auranen, H. Badran, M. Block, R. Briselet, D.M. Cox, M. Dasgupta, A. Di Nitto, Ch.E. Düllmann, T. Grahn, K. Hauschild, A. Herzán, R.-D. Herzberg, F.P. Heßberger, D.J. Hinde, R. Julin, S. Juutinen, E. Jäger, B. Kindler, J. Krier, M. Leino, B. Lommel, A. Lopez-Martens, D.H. Luong, M. Mallaburn, K. Nishio, J. Pakarinen, P. Papadakis, J. Partanen, P. Peura, P. Rahkila, K. Rezynkina, P. Ruotsalainen, M. Sandzelius, J. Sarén, C. Scholey, J. Sorri, S. Stolze, B. Sulignano, Ch. Theisen, A. Ward, A. Yakushev, V. Yakusheva
   Physics Letters B 764, 265–270 (2017)

2. *In-beam spectroscopic study of ^{244}Cf*
   J. Konki, B. Sulignano, P.T. Greenlees, Ch. Theisen, K. Auranen, H. Badran, R. Briselet, D.M. Cox, F. Defranchi Bisso, J. Dobaczewski, T. Grahn, A. Herzán, R.-D. Herzberg, R. Julin, S. Juutinen, J. Khuyagbaatar, M. Leino, A. Lightfoot, J. Partanen, J. Pakarinen, P. Papadakis, P. Rahkila, M. Sandzelius, J. Sarén, C. Scholey, Y. Shi, M. Smolen, J. Sorri, S. Stolze, J. Uusitalo
   Submitted to Physical Review C.

In addition, the author[1] has contributed to the experimental part and the writing process of 58 peer-reviewed publications where the experiments were performed at JYFL, Finland (38), CERN-ISOLDE, Switzerland (18), ANL/LBNL, USA (1) and GSI, Germany (1).

[1] Open Researcher and Contributor ID (ORCID iD): 0000-0001-6200-323X

Contents

1 Introduction **1**
1.1 Discoveries of Bk, Cf and Es isotopes . . . 2
1.2 Motivation . . . 4

2 Theoretical background **7**
2.1 Nuclear models and structure . . . 7
2.1.1 The liquid-drop model . . . 8
2.1.2 The shell model . . . 8
2.1.3 The Nilsson model and deformation . . . 9
2.1.4 The Strutinsky method . . . 11
2.2 Nuclear rotation and moments of inertia . . . 12
2.3 Radioactive decay . . . 14
2.3.1 α decay . . . 15
2.3.2 β^+/EC and β^- decay . . . 16
2.3.3 Fission . . . 17
2.3.4 Electron-capture delayed fission (ECDF) . . . 18
2.4 Electromagnetic transitions . . . 20
2.4.1 γ-ray emission . . . 20
2.4.2 Internal conversion . . . 21

3 Experimental techniques **23**
3.1 Fusion-evaporation reaction . . . 23
3.2 Instrumentation . . . 26
3.2.1 The RITU gas-filled recoil separator . . . 27
3.2.2 The GREAT focal-plane spectrometer . . . 28
3.2.3 The JUROGAMII array . . . 29
3.2.4 Total-data readout (TDR) data-acquisition system . . . 31
3.3 Data-analysis methods . . . 32
3.3.1 The recoil-decay tagging (RDT) technique . . . 32
3.3.2 Half-life determination . . . 33
3.3.3 Cross-section estimation . . . 37

4 Discovery of the new isotopes ^{240}Es and ^{236}Bk **41**
4.1 Experimental details . . . 41

4.1.1 Energy calibrations 43
4.2 Results 43
4.2.1 Recoil identification 44
4.2.2 α-particle energy spectrum 45
4.2.3 ER-α correlations 47
4.2.4 ER-α-α correlations 51
4.2.5 ER-fission and ER-α-fission correlations 54
4.3 Discussion 56
4.3.1 Decay schemes 56
4.3.2 Electron-capture delayed fission probabilities 59
4.4 Future prospects 62

5 In-beam spectroscopy of ^{244}Cf 63
5.1 Experimental details 63
5.1.1 Calibration 64
5.2 Results 64
5.2.1 Recoil identification 65
5.2.2 α-particle energy spectrum 65
5.2.3 α-decay branch of ^{244}Cf 67
5.2.4 Excitation functions 68
5.2.5 Correlation analysis and half-lives 70
5.2.6 Ground-state rotational band of ^{244}Cf 72
5.3 Discussion 77
5.3.1 Systematics in the $N = 146$ isotones 79
5.3.2 Theoretical calculations 81
5.4 Future prospects 84

6 Summary 85

Chapter 1

Introduction

The atomic nucleus is a complex quantum mechanical many-body system that consists of protons and neutrons. The characterisation of individual nuclear species, nuclides, is made by the atomic number Z denoting the number of protons in the nucleus. Nuclei with the same number of protons (Z) are called elements. The number of neutrons is given by the neutron number N. Furthermore, the mass number $A = Z + N$ is used to characterise the total number of protons or neutrons, *i.e.* nucleons, in the nucleus. Nuclei with a specific number of protons (Z) but varying number of neutrons (N) are called isotopes. The number of electrons orbiting a neutral atom is the same as its number of protons. Additionally, both of the protons and neutrons are composite particles called hadrons that are each built of three elementary particles in the Standard Model known as quarks.

Most of the elements found on Earth are stable but few have very long-lived radioactive isotopes. The isotopes that exist naturally on Earth are called primordial nuclides. Around 300 primordial isotopes range from the lightest, hydrogen ($Z = 1$), up to the heaviest, uranium ($Z = 92$). However, most of the about 3000 different known isotopes that have been discovered so far are unstable and have been produced and observed only in the laboratory. According to different theoretical calculations around 3000 to 4000 additional unknown isotopes could exist and are waiting to be discovered in future experiments in accelerator laboratories [Thoennessen11, Erler12].

1.1 Discoveries of Bk, Cf and Es isotopes

The discovery of a new element requires the first observation of any of the isotopes of a nucleus with a new atomic number (Z). The criteria for what is considered as an observation of a new element have been defined precisely and are controlled by an international scientific board, the International Union of Pure and Applied Chemistry (IUPAC). The same scientific board is responsible for confirming the names given to the newly found elements in accordance with their discoverers and following a period of public review. Recently, four new superheavy elements that have been discovered were named by IUPAC as nihonium (Nh, $Z = 113$), moscovium (Mc, $Z = 115$), tennessine (Ts, $Z = 117$) and oganesson (Og, $Z = 118$) [Öhrström16].

In contrast to the discoveries of the new elements, the definitions and criteria for the discovery of new isotopes are not controlled or well defined. Despite the fact that the naming conventions are based solely on the atomic mass number Z, in fact, all of the different isotopes are unique systems that consist of a discrete number of protons and neutrons and have distinctive structural nuclear properties.

The element berkelium (with atomic number $Z = 97$) was first discovered at Berkeley, California in 1950 [Thompson50a, Thompson50c]. In the experiment the isotope ^{243}Bk was produced when an ^{241}Am target was irradiated with an accelerated ^{4}He ion beam. The name berkelium was proposed for the new element after the city where it had been discovered.

Fifteen berkelium isotopes with masses ranging from $A = 233$ to $A = 251$ have been discovered prior to this work [Fry13, Devaraja15, Kaji16], and none of them are stable. The half-lives of the discovered isotopes range from about 21 seconds (^{233}Bk; [Devaraja15]) up to as long as 1380 years (^{247}Bk; [Milsted65]).

The discovery of the element californium (atomic number $Z = 98$) was named following its first observation (of isotope ^{245}Cf) made at Berkeley in 1950 [Thompson50b, Thompson50d]. The name was proposed after the state of California and the University of California in Berkeley. This first isotope was made by irradiating a ^{242}Cm target with a ^{4}He beam. The californium isotope ^{244}Cf was first discovered at Berkeley in 1956 [Chetham-Strode56b] by using an intense α-particle beam and the reactions ^{244}Cm(α,4n)^{244}Cf and ^{242}Cm(α,2n)^{244}Cf. An α-decay half-life of 25(3) min was determined from the emission of 7.17(1) MeV α particles.

Currently, twenty californium isotopes ($A = 237$–256) are known [Fry13], and none of them are stable. The half-lives of the discovered isotopes range from 21 ms (^{238}Cf; [Lazarev95]) up to as long as about 900 years (^{251}Cf; [Metta69]). Prior to this work, the lightest even-even californium isotope, where excited states of a rotational ground-state band have been experimentally measured is ^{248}Cf. No information concerning measurement of the excited states in ^{244}Cf has been published.

The californium isotope ^{243}Cf was discovered in 1967 at two different laboratories simultaneously. At Argonne [Fields67] ^{242}Cm and ^{244}Cm targets were bombarded with ^{3}He ions. The discovery at Berkeley [Sikkeland67b, Sikkeland67a] was done by bombarding various uranium isotopes with a ^{12}C beam and the reactions ^{235}U(^{12}C,4n)^{243}Cf and ^{236}U(^{12}C,5n)^{243}Cf. They estimated that the dominant decay mode of ^{243}Cf is EC-decay with a branching ratio of about EC/$\alpha \sim 10$. The α-particle energies of the isotope were determined based on about 300 α-decay events to be 7.05(2) MeV and 7.17(1) MeV with a half-life of 10.3(5) min. In that study the half-life of ^{244}Cf was estimated with a greater precision to be 19.4(6) min based on about 2000 decay events followed over 8 half-lives.

The discovery of the element einsteinium (atomic number $Z = 99$) was reported for the first time in a scientific publication in 1954 [Ghiorso54] as the observation of the isotopes ^{246}Es and ^{247}Es. The isotopes were produced using accelerated nitrogen ion beams impinging on a ^{238}U target. However, the short letter to the editor included a statement "There is unpublished information relevant to element 99 at the University of California, Argonne National Laboratory, and Los Alamos Scientific Laboratory. Until this information is published the question of the first preparation should not be prejudged on the basis of this paper.". The same statement was included in a publication reporting the discovery of the isotope ^{253}Es that was received for publication one month later [Thompson54]. The official announcement of the discovery of the element 99 (and of element 100, fermium) was reported one year later in 1955 [Ghiorso55] and the name 'einsteinium' was suggested for the new element after Albert Einstein. In the beginning of the report, it was clarified that the first observation of einsteinium was in fact made already in November 1, 1952 after the first full-scale test of a thermonuclear explosion designated as "Ivy Mike" conducted by the United States on the island of Elugelab, Enewetak Atoll in the Pacific Ocean. The einsteinium isotopes were produced in the explosion by the high neutron flux on uranium. The results of the explosive test were classified and delayed the publication of the results on the first observation.

Seventeen einsteinium isotopes ($A = 241$–257) have been discovered prior to this work [Meierfrankenfeld11], and none of them are stable. The half-lives of the discovered isotopes range from 8 seconds (^{241}Es; [Ninov96]) up to as long as 471.7 days (^{252}Es; [Ahmad77]).

A detailed view of the region of interest of the chart of nuclides[1] related to this work is shown in Fig. 1.1. The neutron-deficient isotopes of berkelium (^{236}Bk), californium (^{244}Cf) and einsteinium (^{240}Es) studied in detail in this work are highlighted with black boxes.

[1] Also known as "The Segré chart"

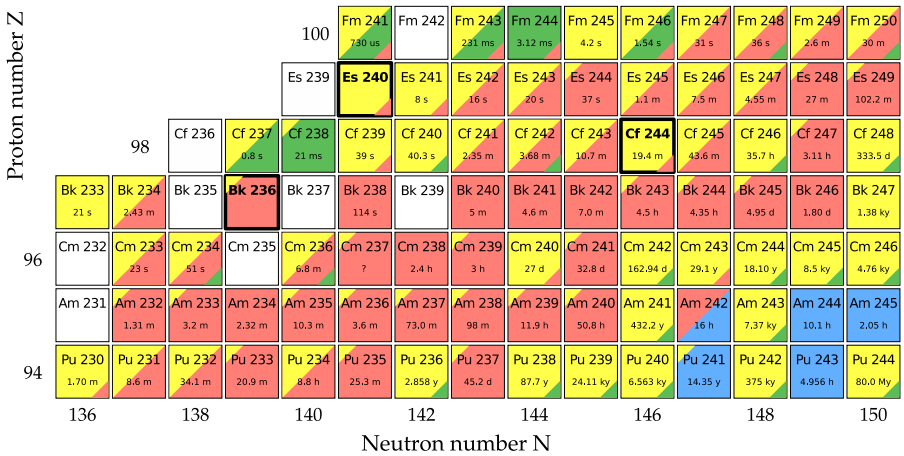

Figure 1.1. Detailed view of the chart of nuclides in the neutron-deficient californium region. The isotopes studied in this work are highlighted with black boxes. The different decay modes and intensities for each nuclide are represented by the different colours in the boxes. Yellow represents α decay, red stands for β^+/EC decay, blue for β^- decay and green for spontaneous fission. Undiscovered isotopes are marked with white boxes.

1.2 Motivation

One of the greatest challenges in nuclear structure physics is understanding the stability of the atomic nucleus. The stability is a key factor in the formation and the present isotopic distribution of elements that are found in nature. For many decades, persistent studies have been made on transfermium superheavy nuclei (SHN) to search for the extreme limits of the stability of the nucleus. The ultimate quest is to find an answer to intriguing questions such as what is the heaviest element of all and how many stable isotopes are there before reaching the proton and neutron driplines. The heaviest elements with $Z > 100$ are stable against fission only due to nuclear shell effects. In fact, according to the classical liquid-drop model they should fission instantly. It has been proposed that the existence of an enhanced and non-zero fission barrier in these nuclei results in lifetimes long enough for them to be observed.

Theoretical calculations predict different locations for the next spherical shell closure beyond $Z = 82$ and $N = 126$. The location of this predicted region of enhanced stability on the nuclear chart is often called the “island of stability”. In order to constrain predictions from various theoretical models, more information on the ordering, spacing and the structure of the single-particle orbitals is needed.

The validation and development of theoretical models is only possible by testing their

predictive power under extreme conditions. Such regions are the unstable nuclei with extreme ratios of proton and neutron numbers when approaching the proton and neutron driplines. Therefore, previously unknown isotopes are synthesised and studied in the accelerator laboratories around the world. Often the limiting factor in these experiments are the low production cross sections of the nuclei of interest when moving further away from the valley of stability which makes detailed studies challenging.

Experimental methods of decay and in-beam spectroscopy have been applied extensively in the recent years to study the structure of deformed heavy nuclei [Herzberg08, Theisen15]. Due to the quadrupole deformation these nuclei have Fermi surfaces near the same single-particle orbitals that originate from a much higher nucleon number. At higher nucleon number the single-particle states are filled until a closed shell is reached where the nuclei are expected to be spherical. These are states that intrude down in energy with increasing deformation and are thus active in lighter deformed nuclei. Therefore, the studies of the deformed heavy nuclei are driven by the interest to find information on the structure of the spherical SHN.

With in-beam γ-ray spectroscopy it is possible to probe the spin dependent properties of the deformed nucleus for instance when it rotates or vibrates. The rotational bands and their moments of inertia can provide information on deformation, deformed shell closures and about the particles that are active in the single-particle orbitals around the Fermi surface. The variation of the moment of inertia as a function of spin is sensitive to pairing correlations and the high-j intruder orbitals. Furthermore, many details on the structure of nuclei can be extracted by studying their radioactive decays. The stability of a nucleus is quantified in terms of the half-life of its radioactive decays such as α, $\beta^{\pm}$, electron capture (EC) and spontaneous fission.

This thesis is based on the results of two separate experiments. In the first part of this work two new neutron-deficient isotopes of the elements einsteinium and berkelium, ^{240}Es and ^{236}Bk, were discovered in a decay spectroscopic study. The second part was devoted to an in-beam spectroscopic study of the neutron-deficient californium isotope ^{244}Cf.

The theoretical concepts, nuclear structure models and theory on radioactive decay that are closely related to the interpretation of the experimental results of this work are introduced in Chapter 2. The experimental techniques and instrumentation that were used in the measurements are presented in Chapter 3.

The details of the experiment, data analysis, results and discussion related to the identification of the new isotopes in the decay spectroscopic study are presented in Chapter 4. Their decay properties such as the half-lives and decay branches were measured. In addition, electron-capture delayed fission (ECDF) branches was observed in both of the new isotopes. The obtained information on the ECDF probabilities are compared the existing experimental data on the heavier odd-odd einsteinium and berkelium isotopes.

In Chapter 5 the details of the experiment, data analysis, results and discussion related to the in-beam γ ray spectroscopic study of ^{244}Cf are described in detail. No excited states were known in the nucleus were known previously. The ground-state rotational band of ^{244}Cf was identified and was measured up to a tentative spin $I^{\pi} = 20^{+}$. The results on the moments of inertia were compared to the systematic behaviour of the heavy even-even $N = 146$ isotones as well as to theoretical calculations where available. To date, ^{244}Cf is the most neutron-deficient even-even californium nucleus where excited states have been measured.

Chapter 2

Theoretical background

Studying the interactions between the nucleons in the dense atomic nucleus is a challenging task for both the experimentalists and the theoreticians. One of the main objectives in nuclear structure physics is to understand the behaviour and motion of the nucleons inside the nucleus and to derive the characteristic features of the whole nucleus from those interactions.

In this chapter an introduction to some of the basic and most important theoretical nuclear structure models and their features are presented. The models are used to interpret and predict various quantities that can be measured such as the half-life and the energy that is released when a nucleus decays, the energies of transitions in an excited nucleus and its moments of inertia.

2.1 Nuclear models and structure

Various theoretical nuclear models have been developed to describe the atomic nucleus by employing a few simple arguments. The nucleus is held together by one of the fundamental forces of nature, the strong force. It is attractive, short-range and is able to overcome the repulsive Coulomb force between the protons inside the nucleus. Additionally, the nucleons are fermions and must obey the Pauli exclusion principle.

The major challenge for the models is that the number of nucleons that interact with each other is discrete. Moreover, the number of interacting particles is often too high to treat the ensemble microscopically and at the same time too small to treat them statistically in the calculations. Consequently, the different models are often applicable in certain regions of the nuclear chart or in reproducing certain features of the nuclei but not accurate in describing the detailed structure in all of them simultaneously.

2.1.1 The liquid-drop model

One of the earliest theoretical descriptions and quantitative models of the nucleus is the liquid-drop model (LDM) [Gamow30]. In this simple model an analogy is made in which the nucleus is assumed to behave like an incompressible liquid drop of constant density. The atomic mass of a nucleus with Z protons and N neutrons[1] can be estimated by using the so-called semi-empirical mass formula (Bethe-Weizsäcker formula) [Weizsäcker35] $m(Z,N) = Nm(^1\mathrm{n}) + Zm(^1\mathrm{H}) - B(Z,A)/c^2$, where the binding energy of the nucleus is given by

$$B(Z,A) = a_{\mathrm{vol}}A - a_{\mathrm{surf}}A^{2/3} - a_{\mathrm{asym}}\frac{(A-2Z)^2}{A} - a_{\mathrm{C}}\frac{Z(Z-1)}{A^{1/3}} + \delta(A,Z). \tag{2.1}$$

Here a_{vol}, a_{surf}, a_{asym} and a_{C} are the volume, surface, asymmetry and Coulomb term coefficients that are obtained from a fit to experimental atomic masses, and $m(^1\mathrm{H})$ and $m(^1\mathrm{n})$ are the atomic masses of the hydrogen atom and the neutron, respectively. The last term, δ, is a correction term due to the pairing effect which is the tendency of the protons or neutrons to form pairs and gain extra stability in nuclei with even number of nucleons.

Despite its simplicity, the liquid-drop model can describe the general evolution of the binding energies and atomic masses of nuclei from very light to heavy elements. It can also explain phenomena related to the nuclear fission decay process via elongation and deformation of the nucleus and give simple estimates about the heights of the fission barriers. However, it fails to reproduce the effects of shell structure in nuclei that are evident from many experimental observations. One such effect is the extra stability of nuclei with certain proton and neutron numbers that are often called the "magic numbers". Further refinements of the LDM are essentially higher order expansions of the original concept such as the the droplet model [Myers69]. The similar finite-range droplet model (FRDM) and finite-range liquid drop model (FRLDM) are currently used to estimate nuclear masses and fission barriers (see *e.g.* [Möller16, Möller09] and references therein).

2.1.2 The shell model

The spherical shell model [Mayer49, Haxel49] of the nucleus assumes that the nucleons in the nucleus orbit independently in a spherical central potential created by the other nucleons. The central potential is created by one of the fundamental forces in nature, the attractive and short-range nuclear strong force, that is not well understood even today. In addition, the protons in the nucleus feel the repulsive and long-range Coulomb force due to their electric charge. Various different forms can be used for the shape of the potential from simple square-well or harmonic-oscillator potential (H.O.) to

[1] The mass number $A = Z + N$

a more realistic Woods-Saxon potential (W.-S.). A schematic representation of the single-particle states and their evolution when using different and more realistic central potentials is shown in Fig. 2.1.

The spherical shell model best describes light spherical nuclei near the closed major shells. The magic numbers of spherical nuclei are successfully recreated by the model by including a spin-orbit coupling term ($\vec{l} \cdot \vec{s}$) in the potential. The magic numbers for the protons and neutrons are $Z, N = 2, 8, 20, 28, 50, 82$ and additionally $N = 126$ for neutrons. The spin-orbit interaction splits the states with the same orbital angular momentum l into two states with total angular momenta $j = l + s$ and $j = l - s$, where $s = 1/2$ is the intrinsic spin of the nucleon. When approaching mid-shell the nuclei become more collective in their behaviour and the ground states of the nuclei become deformed. The further extension of the spherical shell model to deformed nuclei is called the Nilsson model or the deformed shell model.

2.1.3 The Nilsson model and deformation

In the Nilsson model [Nilsson55] the single-particle states are calculated in a deformed central potential that is axially symmetric. The original model used a harmonic oscillator potential in the calculations. The small assumed quadrupole deformation (β_2) give rise to either prolate or oblate nuclear shapes that are axially symmetric.

In the Nilsson model the states are labelled with the notation

$$\Omega^{\pi}[Nn_z\Lambda], \tag{2.2}$$

where the conserved (good) quantum numbers are Ω, the projection of the angular momentum $\vec{j} = \vec{l} + \vec{s}$ onto the symmetry axis (Z axis) of the nucleus and the parity $\pi = (-1)^N$. Here N is the principal quantum number that denotes the major shell, n_z is the number of crossings (nodes) of the wave function in the Z direction and Λ is the projection of the orbital angular momentum $\vec{l}$ onto the symmetry axis. Each Nilsson state can hold a maximum of two like nucleons (time-reversal symmetry). In case of a state with many nucleons, the total projection to the symmetry axis of the angular momenta Ω_i is denoted as $K = \sum_i \Omega_i$. The angular momentum vectors and labeling are elaborated in the diagram of Fig. 2.2.

The general behaviour of the splitting and the energies of the single-particle states as illustrated in Fig. 2.1 with increasing deformation can be understood with some simple arguments. A large overlap with a prolate nucleus ($\beta_2 > 0$) occurs with low-Ω orbitals and lowers their energy with increasing deformation. In contrast, the high-Ω orbitals are lowered in energy for an oblate nucleus ($\beta_2 < 0$) with increasing deformation.

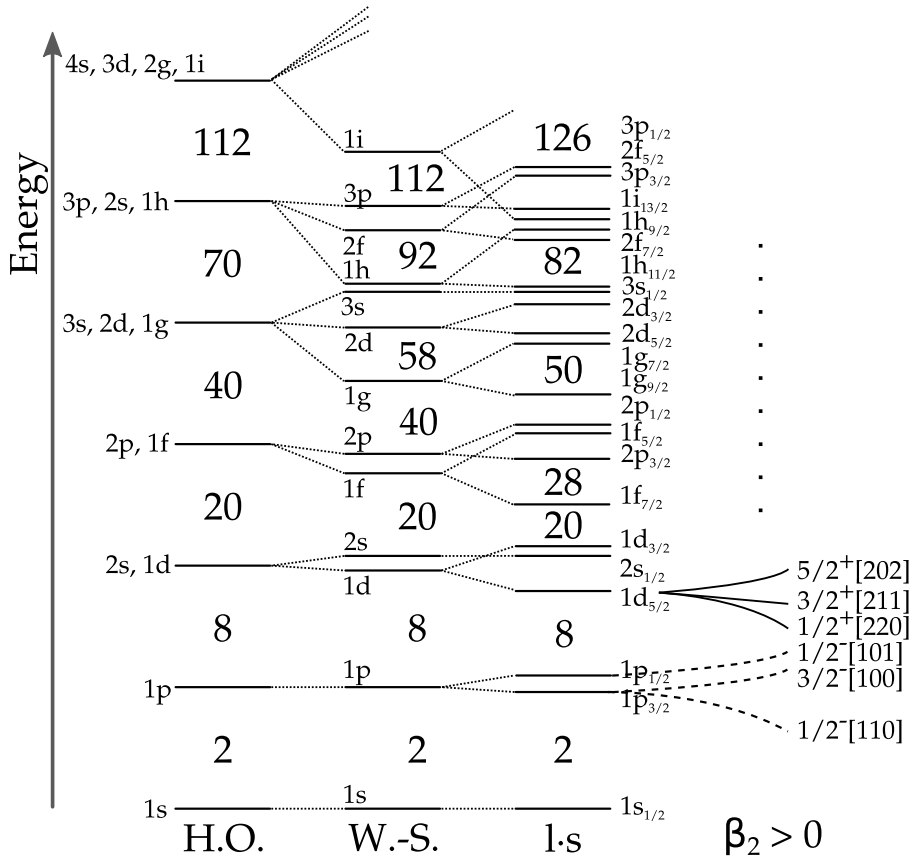

Figure 2.1. Schematic representation of the behaviour of the single-particle energy levels in the nuclear shell model when using different mean-field potentials. The degeneracy in the energy levels is lifted and gaps corresponding to the indicated magic numbers are formed when moving from left to right in the figure from the harmonic oscillator (H.O.) potential to the more realistic Woods-Saxon (W.-S.) potential and including a spin-orbit coupling term with the Woods-Saxon potential ($\vec{l} \cdot \vec{s}$). Finally, the splitting of the single-particle energy levels as a function of increasing prolate deformation of the nucleus ($\beta_2 > 0$) in the Nilsson model is illustrated for few levels. Note that the absolute energy of the levels is not to scale and the exact ordering of the levels depends on the chosen potential.

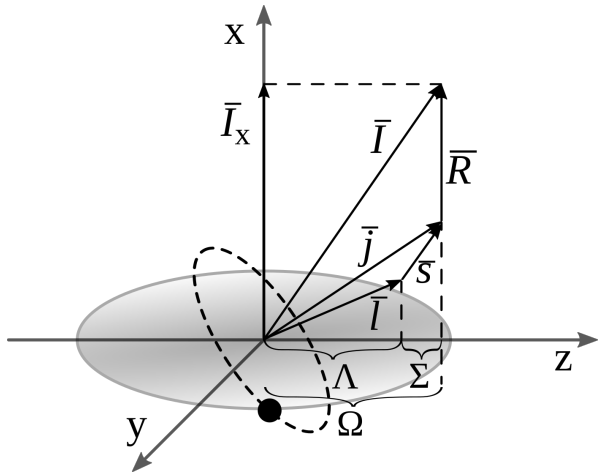

Figure 2.2. General diagram showing the angular momentum vectors and quantities related to the single-particle states and their labeling in the Nilsson model. The total angular momentum $\vec{I}$ is composed of the angular momentum of the valence nucleon $\vec{j} = \vec{l} + \vec{s}$ and the collective angular momentum of the core $\vec{R}$. The component of $\vec{I}$ along the rotation axis is denoted as $\vec{I_x}$. For an axially symmetric nucleus $\vec{R} \perp \hat{z} \Rightarrow \Omega = K$.

2.1.4 The Strutinsky method

Calculating the potential energy surfaces of a nucleus and the heights of the fission barriers by using either the liquid-drop model (LDM) or deformed single-particle models alone are inadequate in many cases. However, a combination of the two inherently different methods first suggested by Strutinsky [Strutinsky67] has proven more successful. In the Strutinsky shell-correction method which is the basis of modern macroscopic-microscopic models, the main idea is that the average and long-range features including the average deformation of the total energy of the nucleus (E_{macro}) are calculated using a macroscopic approach with the LDM. A shell-correction energy obtained from a microscopic model such as the shell model is then applied on top of the liquid-drop energy.

The total energy of the nucleus is written as

$$E_{\text{tot}} = E_{\text{macro}} + E_{\text{micro}} = E_{\text{macro}} + \sum_i \epsilon_i - \widetilde{E}_{\text{shell}}, \tag{2.3}$$

where $\sum_i \epsilon_i$ is the sum over all of the individual single-particle energies of the nucleons and $\widetilde{E}_{\text{shell}}$ is a smoothed average of the total energy calculated by using a smeared level density in the microscopic model. In this way, the variations to the total energy from the shell structure are taken into account as small magnitude shell-corrections that provide stability for a nucleus against fission required to explain the enhanced stability and existence of superheavy nuclei.

A schematic illustration of the total potential energy of an arbitrary superheavy nucleus as a function of the deformation along the easiest path through the multi-dimensional deformation space leading to fission is shown in Fig. 2.3. The potential energy calculated by using only the LDM (dashed line) showing the smooth average trend of the potential. A bound ground state cannot be achieved in this superheavy nucleus with the LDM due to a missing potential barrier against fission. When the shell-correction energy is applied on top of the LDM calculation (solid line) the small fluctuations provided by the correction are enough to create a minimum in the potential energy and to provide a barrier against fission where a bound spherical ground state can be formed.

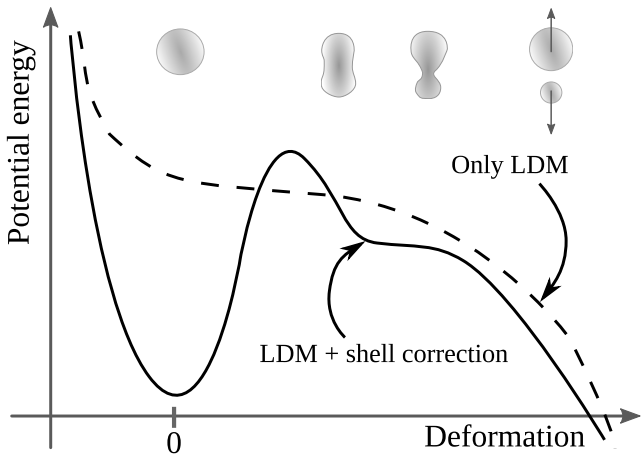

Figure 2.3. Schematic representation of the nuclear potential energy of an arbitrary spherical superheavy nucleus as a function of the increasing deformation along the path leading to fission by using only the liquid-drop model (LDM) and including the shell-correction energy in the LDM potential energy. The shape of a nucleus approaching fission with a preference for asymmetric mass distribution is illustrated at the top.

2.2 Nuclear rotation and moments of inertia

The collective rotation of a nucleus is possible in a quantum mechanical sense only when the nucleus is deformed. This allows the orientation of the nucleus to be defined and the probability to observe different effects when the nucleus rotates. Assuming pure collective rotation of an even-even nucleus ($\vec{R} = \vec{I}$, $K = \Omega = 0$) the excited energy levels in the ground-state band of an axially symmetric deformed rotor are given by the relation [Bohr53, Nilsson95]

$$E(I) = \frac{\hbar^2}{2\mathcal{J}} I(I+1), \quad I = 0, 2, 4, ..., \tag{2.4}$$

where I is the total angular momentum (spin) of the state and $\mathcal{J}$ is the static moment of inertia.

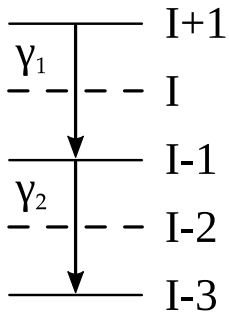

Figure 2.4. Transitions between three consecutive states in a rotational band and the labeling of their angular momenta in the calculation of the rotational frequencies and the moments of inertia. Here γ_1 represents the γ-ray transition from the state with $I+1 \rightarrow I-1$ with energy E_{γ_1}. Similarly, the transition between the states $I-1 \rightarrow I-3$ is denoted by γ_2 with an energy of E_{γ_2}.

Using the labeling given in Fig. 2.4, the rotational frequency at nuclear spin I can be defined as [Wu92a, Wu92b]

$$\omega(I) = \frac{1}{\hbar}\frac{dE}{dI_x} \approx \frac{1}{\hbar}\frac{E(I+1)-E(I-1)}{I_x(I+1)-I_x(I-1)} \approx \frac{E_{\gamma_1}}{2\hbar}, \tag{2.5}$$

where $I_x(I) = \sqrt{I(I+1)-K^2}$ and the assumption that $K = 0$ has been used and E_{γ_1} is the energy difference between the states with $I+1$ and $I-1$.

The kinematic moment of inertia is defined as

$$\mathcal{J}^{(1)}(I) = \hbar\frac{I_x}{\omega} = \hbar^2 I_x\left(\frac{dE}{dI_x}\right)^{-1} \approx \hbar^2\frac{2I-1}{E(I+1)-E(I-1)} = \hbar^2\frac{2I-1}{E_{\gamma_1}} \tag{2.6}$$

and the dynamic moment of inertia is

$$\mathcal{J}^{(2)}(I-1) = \hbar\frac{dI_x}{d\omega} = \hbar^2\left(\frac{d^2E}{dI_x^2}\right)^{-1} \approx \hbar^2\frac{4}{E_{\gamma_1}-E_{\gamma_2}} = \frac{4\hbar^2}{\Delta E_\gamma} \tag{2.7}$$

The rotational frequency used to calculate $\mathcal{J}^{(2)}$ corresponds to spin $I-1$ where the average frequency is

$$\omega(I-1) \approx \frac{E_{\gamma_1}+E_{\gamma_2}}{4\hbar}. \tag{2.8}$$

A parameterisation of the rotational band according to the Harris formalism [Harris65] leads to the relation of the kinematic $\mathcal{J}^{(1)}$ and dynamic $\mathcal{J}^{(2)}$ moments of inertia by the equations

$$\mathcal{J}^{(1)} = \mathcal{J}_0 + \mathcal{J}_1\omega^2, \tag{2.9}$$

$$\mathcal{J}^{(2)} = \mathcal{J}_0 + 3\mathcal{J}_1\omega^2, \tag{2.10}$$

where $\mathcal{J}_0$ and $\mathcal{J}_1$ are the so-called Harris parameters. The parameters $\mathcal{J}_0$ and $\mathcal{J}_1$ can be fitted to the low-spin part of a rotational band of an even-even nucleus and used to extrapolate and determine the energies of often highly-converted low-energy transitions 4^+ to 2^+ and 2^+ to 0^+ in the same band using the equation

$$I(\omega) = \mathcal{J}_0\omega + \mathcal{J}_1\omega^3 + {}^1\!/_2, \tag{2.11}$$

where I is the initial spin of the transition.

2.3 Radioactive decay

The radioactive decay of a nucleus or an excited state is statistical in nature and can be characterised by the linear differential equation [Heyde04]

$$dN = -\lambda N dt, \tag{2.12}$$

where N is the number of nuclei and λ is the decay constant. The solution of the differential equation 2.12 is of the form

$$N(t) = N_0 e^{-\lambda t}, \tag{2.13}$$

where N_0 is the number of nuclei at time $t = t_0$. The decay constant λ in the exponential decay law of Eq. 2.13 is related to the half-life and to the mean lifetime $\bar{\tau}$ by the relation

$$T_{1/2} = \frac{\ln 2}{\lambda} = \ln 2 \cdot \bar{\tau}. \tag{2.14}$$

The partial half-life $T^i_{1/2}$ is a useful quantity used to compare different decay modes or decays to different final states. It is defined by using the branching ratio b_i of the decay mode i as

$$T^i_{1/2} = \frac{T_{1/2}}{b_i}. \tag{2.15}$$

The ground state or an excited state of a nucleus can decay or de-excite spontaneously in different ways mostly depending on the energy that is available between the initial and final state. The decay can proceed by emission of particles such as a proton, a neutron or an α particle where the nucleus transforms itself into another nucleus. The nucleus can also split into two lighter nuclei in the fission process. Excited states in a nucleus can also decay in the former ways or there may be a transition to a state that is lower in energy in the same nucleus by the emission of electromagnetic radiation or internal conversion electrons. The decay processes most relevant to this work are introduced in the following sections.

2.3.1 α decay

One of the very first nuclear decay processes that was discovered as naturally occuring radioactivity was α decay. In this decay mode, a mother nucleus decays to a lighter daughter nucleus by emitting an α particle (^{4}He nucleus). The emission of an α particle in α decay of the mother nucleus X to the daughter nucleus Y and the α particle can be expressed by the process [Krane88]

$$\mathrm{X}_N \rightarrow {}^{A-4}_{Z-2}\mathrm{Y}_{N-2} + \alpha. \tag{2.16}$$

The Q value of the decay (Q_α) is defined using the atomic masses as [Krane88]

$$Q_\alpha = \left(m(\mathrm{X}) - m(\mathrm{Y}) - m({}^4_2\mathrm{He})\right)c^2. \tag{2.17}$$

When the mass of the initial nucleus is greater than the masses of the daughter and the α particle ($Q > 0$), α decay can happen spontaneously. The decay occurs spontaneously in heavy nuclei where it becomes energetically possible.

The Q_α value corresponds to the kinetic energy that is shared between the daughter nucleus and the α particle. The kinetic energy of the α particle (E_α) in the α decay is [Krane88]

$$E_\alpha = \left(\frac{1}{1 + m({}^4_2\mathrm{He})/m(\mathrm{Y})}\right) \cdot Q_\alpha. \tag{2.18}$$

The semi-empirical law found by Geiger and Nuttall in 1911 [Geiger11] is a rough estimate of the α decay half-life for each isotopic chain to be inversely proportional to the energy of the decay

$$\log(\lambda) = A(Z) + \frac{B(Z)}{\sqrt{Q_\alpha}}, \tag{2.19}$$

where λ is the decay constant ($\lambda = {}^{\ln 2}/_{T_{1/2}}$) and A,B are fitted parameters. A striking effect of this empirical finding is that a very small change in the Q value has a large effect on the decay half-life. Moreover, this simple relationship holds for half-lives that span over many orders of magnitude in the isotopic chains. For example, a factor of two change in the Q value causes a factor of 10^{22} change in the half-lives of the polonium isotopes. However, it has been shown that this very simple law may not hold exactly in some extreme cases such as in the most neutron-deficient polonium isotopes [Qi14].

The first theoretical quantum mechanical descriptions of α decay were made simultaneously and independently in 1928 by Gamow [Gamow28] and by Condon and Gurney [Gurney28]. In these models, the α particle is assumed to be preformed inside the daughter nucleus with a certain preformation probability. To escape the nucleus, the α particle has to tunnel through the Coulomb barrier and represents a prime example of quantum mechanical tunneling. One often used method to calculate theoretical

estimates of α-decay half-lives was introduced by Rasmussen in 1959 [Rasmussen59]. The model is based on a realistic potential obtained from scattering experiments and takes into account the effects of angular momentum.

Comparison of measured α-decay half-lives to theoretical calculations can provide valuable information on the structure of the initial and final states in the mother and daughter nuclei, respectively. The α-decay hindrance factor is a useful quantity for comparison and is typically defined for even-even nuclei as the ratio of the measured half-life to a calculated half-life from some theoretical model as

$$HF = \frac{T_{1/2}^{\alpha,\text{meas}}}{T_{1/2}^{\alpha,\text{theo}}}. \tag{2.20}$$

The theoretical half-life $T_{1/2}^{\alpha,\text{theo}}$ can be obtained, for example, with the calculation according to the Rasmussen method.

When considering the α decay of odd nuclei, the hindrance factor of a ground-state to ground-state ($0^+ \rightarrow 0^+$) decay in a neighbouring even-even nucleus is typically defined as 1. For an odd-A nucleus, a hindrance factor of $HF < 4$ is then usually obtained for a favoured transition where the initial and final states in the decay have the same spin, parity and configuration. Such a decay is also called unhindered α decay. If the spins of the initial and final state are different it means that angular momentum is carried away by the α particle and the barrier it has to tunnel through is higher and wider. Thus, the change in angular momentum results in a longer half-life and a larger hindrance factor.

In the case of α decays of nuclei with odd-A or both odd-Z and odd-N, there is often a change in the spins and parities between the initial state in the mother and the final state in the daughter nucleus. Therefore, the hindrance factors for odd nuclei are often defined as ratios to the closest neighbouring even-even nuclei.

2.3.2 β^+/EC and β^- decay

The β decay is a nuclear decay process mediated by the weak interaction. Three different types of β decays exist, namely β^-, β^+ and electron capture (EC). The nuclear processes for the decays can be described with the formulas

$$\beta^- : \quad {}^{A}_{Z}\mathrm{X}_N \rightarrow {}^{A}_{Z+1}\mathrm{Y}_{N-1} + e^- + \bar{\nu}_e, \tag{2.21}$$

$$\beta^+ : \quad {}^{A}_{Z}\mathrm{X}_N \rightarrow {}^{A}_{Z-1}\mathrm{Y}_{N+1} + e^+ + \nu_e, \tag{2.22}$$

$$\mathrm{EC} : \quad {}^{A}_{Z}\mathrm{X}_N + e^- \rightarrow {}^{A}_{Z-1}\mathrm{Y}_{N+1} + \nu_e, \tag{2.23}$$

where the elementary particles taking part in the decay processes are the proton (p), the neutron (n), the electron (e^-) and its antiparticle the positron (e^+), the electron neutrino (ν_e) and the electron antineutrino ($\bar{\nu}_\mathrm{e}$). Higher order and more rare processes include

the so-called ordinary double-β decay and the yet unobserved neutrinoless double-β decay.

Theoretical description of the variations of β decay is more complicated because the β particle and neutrino have to be created in the process and are not preformed inside the nucleus as in α decay. First such quantum-mechanical description was given by Fermi in 1934 [Fermi34].

2.3.3 Fission

Nuclear fission [Vandenbosch73] was the third nuclear decay mode that was discovered for the first time in 1938-1939 [Hahn38, Hahn39] and described successfully in 1939 [Meitner39]. Similar to the theoretical description of α decay, it can be considered as a quantum mechanical tunneling process. In this decay mode the mother nucleus breaks up into two smaller fragments and releases a total kinetic energy equal to the difference in the masses of the mother nucleus and the daughter nuclei. One of the earliest comprehensive theoretical descriptions of fission was made using the liquid-drop model by Bohr and Wheeler [Bohr39] already in 1939.

A schematic illustration of the fission process is shown in Fig. 2.5 where the total energy of the system is plotted as a function of a deformation parameter. For simplicity, a one-dimensional deformation parameter is considered here. In reality, the theoretical description of fission is a multi-deformation-parameter problem. Fission from the ground state (g.s.) of a nucleus is called spontaneous fission. The corresponding fission barrier of the spontaneous fission (B_{sf}) is shown as the energy difference of the g.s. and the top of the inner barrier. In some nuclei, for example in the actinides, a concept of an outer second barrier may be formulated and can cause significant fission hindrance. Such a barrier structure is often called a double-humped fission barrier. Normal and subbarrier fission occur after being induced by *e.g.* neutrons, protons or γ rays exciting the nucleus to an excited state where fission proceeds through a smaller fission barrier. Isomeric states at a second local minimum at larger deformation can occur due to the outer barrier where the nucleus is trapped before decaying via isomeric fission.

Fission is a very complex decay mode due to the large prompt energy release and the large elongation and deformation of the nucleus. The drastic rearrangement of nuclear matter involves both collective and single-particle effects at extreme conditions. Consequently, it has been studied for decades both experimentally and theoretically. Fission plays the key role in the production of, especially, the superheavy nuclei (SHN) via fusion-evaporation reactions due to the competition of fission with the survival probability of the compound nucleus. Furthermore, the concept of fission barriers including the effects of the nuclear shell structure explains the stability of the SHN and is vital in the search for the so-called “island of stability”. Recently, a distinctive type of fission called the electron-capture delayed fission has become popular as a powerful tool to study low-energy fission properties in nuclei.

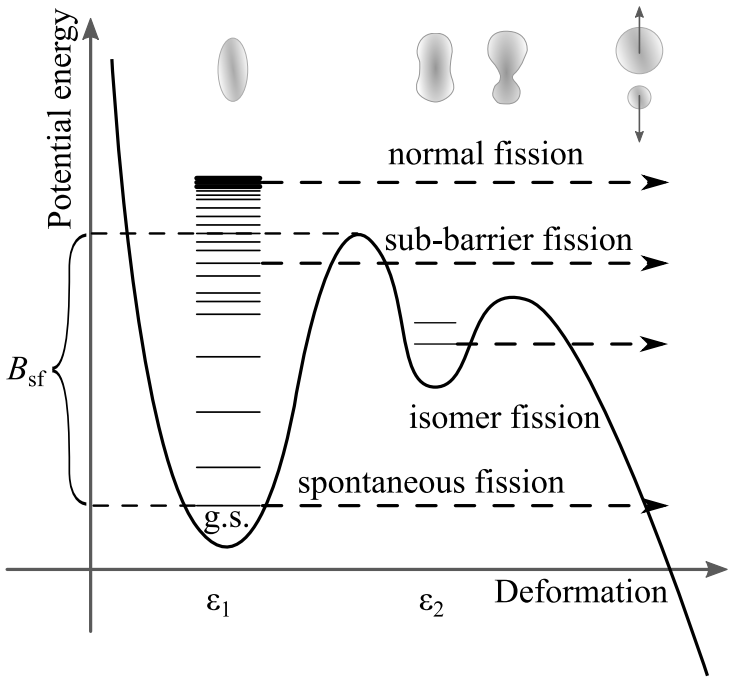

Figure 2.5. Schematic illustration of the various possibilities of the fission decay process of a nucleus. Fission from the ground state (g.s.) of a nucleus is called spontaneous fission and the associated fission barrier height is B_{sf}. Isomeric fission may proceed from an excited isomeric state that has a larger deformation (ϵ) than the ground state and a lower fission barrier at the second hump. Normal and subbarrier fission may be induced by *e.g.* impinging neutrons that first excites the nucleus to an excited state. The shapes of a nucleus approaching fission with a preference for asymmetric mass distribution is shown at the top.

2.3.4 Electron-capture delayed fission (ECDF)

Electron-capture delayed fission (ECDF), or more generally β-delayed fission (βDF), is a two-step nuclear decay mode that was discovered in 1966 (see *e.g.* [Kuznetsov99] and references therein) and described succesfully for the first time in 1969 [Berlovich69]. A simplified diagram of the ECDF process is shown in Fig. 2.6. In the first step the mother nucleus undergoes β^+/EC (neutron-deficient nuclei) or β^- (neutron-rich nuclei) decay and populates an excited state in the daughter nucleus. Depending on the decay Q value (Q_{EC}) of the precursor, the height of the fission barrier (B_{sf}) of the daughter nucleus and the population of the excited states close to and above the fission barrier in the daughter nucleus, fission can compete with other decay modes of the excited states such as γ-ray or particle emission.

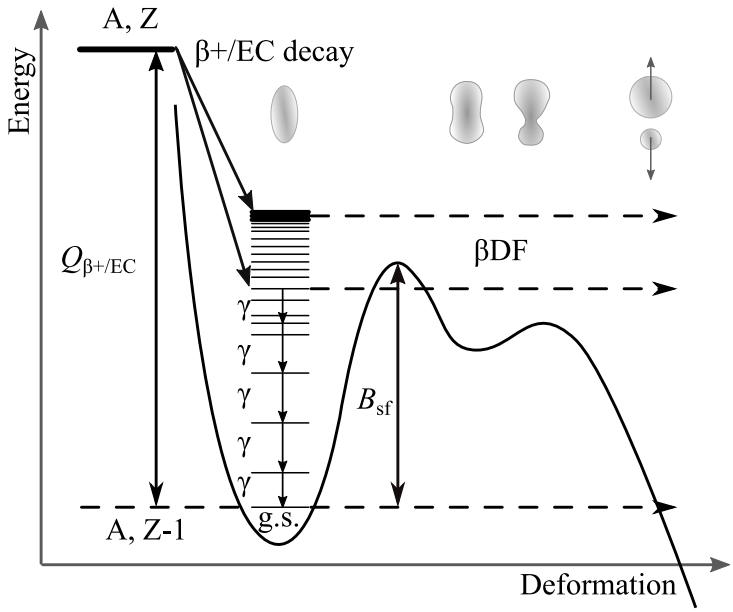

Figure 2.6. Schematic illustration of the β^+/EC-delayed fission process in a neutron-deficient nucleus. The ground state of the mother nucleus (A, Z) decays to excited states in the daughter nucleus $(A, Z-1)$ via β^+/EC decay. The excited states either decay via γ-ray transitions or fission directly. Potential energy in the daughter nucleus is shown as a function of increasing deformation when approaching fission. The $Q_{\beta^+/\mathrm{EC}}$-value of the decay and the fission barrier height in the daughter (B_{sf}) are indicated.

The Q_{EC} value limits the maximum excitation energy of the states that can be populated in the daughter nucleus in the decay. Furthermore, an enhanced probability for the ECDF decay is expected if the Q_{EC} value exceeds the fission barrier height B_{sf}. Recently, a review of the current status of delayed fission measurements was published [Andreyev13], indicating that not many experiments have been performed in cases where the energy difference $Q_{\mathrm{EC}} - B_{\mathrm{sf}}$ is positive and that there is a growing interest to probe the low-energy fission properties of nuclei via this process.

A typical quantity that can be measured is the experimental probability of ECDF that is defined as [Andreyev13]

$$P_{\mathrm{ECDF}} = \frac{N_{\mathrm{ECDF}}}{N_{\mathrm{EC}}}, \tag{2.24}$$

where N_{ECDF} is the number of EC decays resulting in fission and N_{EC} is the total number of EC decays of the mother nucleus. The temporal characteristics of the ECDF decays are determined by the half-life of the mother nucleus because fission directly from the excited states must be fast enough to compete with the other decay modes which typically occur on a time scale of picoseconds.

2.4 Electromagnetic transitions

An excited state of a nucleus can de-excite, releasing its excess energy by the emission of electromagnetic (EM) radiation. In the process the charge distribution of the nucleus is changed. The energy difference between the initial and final state is released as a fluctuation of the EM field in the form of a quantum of energy called a photon. The photons that are emitted from the nucleus are called γ rays. Another competing process for the de-excitation is called internal conversion where atomic electrons are emitted from the nucleus. Other competing processes include internal pair formation (IPF) above a 1.022 MeV threshold energy where an electron-positron pair is created and the emission of two γ rays. The emission of two γ rays is a higher order process and can be neglected in this study.

2.4.1 γ-ray emission

The probability of an electromagnetic transition depends on the energy that is available for the transition and on the angular momentum and the parity of the initial (I_i) and final (I_f) states. The multipolarity of the transition is determined by the angular momentum L that is carried away by the γ ray. The conservation of angular momentum and parity yields the selection rules giving the allowed multipolarities L of electric (EL) and magnetic (ML) transitions that are

$$|I_i - I_f| \leq L \leq I_i + I_f, \tag{2.25}$$

and the allowed parities

$$\pi_i \pi_f = \begin{cases} (-1)^L & \text{for electric (EL)} \\ (-1)^{L+1} & \text{for magnetic (ML).} \end{cases} \tag{2.26}$$

The transition probabilites and rates can be estimated by using, for example, the shell model. The Weisskopf estimates [Weisskopf51] are based on calculating reduced transition probabilities as transitions of a single nucleon between two single-particle states of the spherical shell model. An additional assumption that is made is that the radial parts of the initial and final wave functions are constant inside the nucleus and vanish on the outside. The estimated transition rates λ_{W} are given in Table 2.1 for the lowest multipolarities of electric and magnetic transitions. Measured transition rates can be normalised to the calculated Weisskopf estimates and given in Weisskopf units (W.u.). This allows to estimate whether a transition is of more collective or single-particle nature.

Table 2.1. Weisskopf single-particle transition rate estimates [Weisskopf51] (λ_W) for the lowest multipoles $L \leq 3$ of transitions of electric (σ = E) and magnetic (σ = M) character. The transition energies E_γ are in units of MeV and A is the mass number of the nucleus.

σL	λ_W (1/s)	σL	λ_W (1/s)
E1	$1.023 \cdot 10^{14} E_\gamma^3 A^{2/3}$	M1	$3.184 \cdot 10^{13} E_\gamma^3$
E2	$7.265 \cdot 10^{7} E_\gamma^5 A^{4/3}$	M2	$2.262 \cdot 10^{7} E_\gamma^5 A^{2/3}$
E3	$3.385 \cdot 10^{1} E_\gamma^7 A^{2}$	M3	$1.054 \cdot 10^{1} E_\gamma^7 A^{4/3}$

2.4.2 Internal conversion

Internal conversion [Hulme32, Kantele95] (IC) is an alternative and competing process in the de-excitation of the excited states of a nucleus alongside γ-ray emission. Internal conversion can be the dominant process especially in low-energy transitions in heavy nuclei with high Z. Therefore, spectroscopy of internal conversion electrons is a valuable tool in conjunction with γ-ray spectroscopy.

Internal conversion electrons (ICE) are emitted when a higher energy state of the nucleus decays to a lower state via an electromagnetic transition. An electron is ejected from one of the atomic orbitals when the electron interacts with the nucleus. There is a change in the charge distribution of the nucleus, and the energy of the transition is transferred to the atomic electron. Relaxation of the electron shells when the created holes in the electron orbitals are filled by electrons from higher orbitals results in the emission of characteristic X-rays and Auger electrons.

The internal conversion coefficient (ICC) is often used as a measure of the preferred mode of de-excitation by internal conversion or γ-ray emission. It is defined as the ratio of the electron emission rate to the γ-ray emission rate

$$\alpha = \frac{\lambda_e}{\lambda_\gamma}. \tag{2.27}$$

The decay rate is different for different electron shells and the total decay rate can be easily written as a sum of the partial decay rates λ_i corresponding to the different atomic orbitals i as $\lambda_e = \sum_i \lambda_i$. Then the conversion coefficient is a sum of the partial conversion coefficients of the electronic shells

$$\alpha = \frac{1}{\lambda_\gamma} \left(\lambda_{e_K} + \lambda_{e_{LI}} + \dots\right) = \alpha_K + \alpha_{L_I} + \dots. \tag{2.28}$$

The total decay rate of an excited state can now be written as

$$\lambda_t = \lambda_\gamma + \lambda_e = \lambda_\gamma(1 + \alpha) = \lambda_\gamma \left(1 + \alpha_K + \alpha_{L_I} + \dots\right). \tag{2.29}$$

The electron orbiting the nucleus in orbital i is bound with a binding energy B_i. Therefore, the kinetic energy of the emitted electron is the energy difference between the two states in the nucleus ΔE minus the electron binding energy

$$E_{\mathrm{e}}^{i} = \Delta E - B_i. \tag{2.30}$$

This means that for a given transition the emitted electron can have different energies depending on the atomic orbital (K, L_1, L_2, L_3, M_1, ...) from which it is ejected. If it is energetically possible, the electron is most often emitted from the K-shell, where the spatial overlap of the electron wavefunction and the nucleus is the largest.

Electric monopole (E0) transitions are special cases that cannot proceed by emission of a single γ ray. The emission of one γ ray is strictly forbidden, because the photon has a spin of unity and angular momentum has to be conserved. However, these transitions can proceed via internal conversion. The E0 transitions are either of a 0^+ state to another 0^+ state or transitions between initial and final states that have the same spin and parity $J^\pi \rightarrow J^\pi$.

Chapter 3

Experimental techniques

The heavy neutron-deficient nuclei that were studied in this work were produced in heavy-ion induced fusion-evaporation reactions at the Accelerator Laboratory of the Department of Physics, University of Jyväskylä, Finland (JYFL). The ions of stable projectile nuclei were extracted from an electron-cyclotron resonance (ECR) ion source and accelerated by the K130 cyclotron [Liukkonen92] and delivered to the target. The nuclei of interest are often produced in very small quantities compared to other unwanted reaction channels and must be separated from the background with carefully designed equipment and methods. The fusion-evaporation reaction mechanism and the experimental setup that were used in the measurements of this work are briefly described in the following sections.

3.1 Fusion-evaporation reaction

In order to study transuranium nuclei that are radioactive with short half-lives that cannot be found in nature, they have to be produced in nuclear reactions in accelerator laboratories. The fusion-evaporation reaction is a very useful tool in nuclear physics research that has been extensively utilised in recent decades. It has been used to artificially produce isotopes of new superheavy elements that do not exist in nature, and to study the properties and structure of exotic nuclei under laboratory conditions.

The heavy-ion induced fusion-evaporation reaction can be considered as a two-step fusion process described by the general reaction

$$a + A \rightarrow C^* \rightarrow B + b. \tag{3.1}$$

First, a target nucleus (A) is bombarded by an accelerated ion beam (a) with a kinetic energy high enough to overcome the Coulomb barrier. The barrier is a repulsive

electrical potential that is created by the positive charge of the protons in the nuclei of the target and projectile. The barrier height can be approximated with the height of the Coulomb barrier at the point where the surfaces of the projectile and target nuclei are touching and is given by the equation

$$V_C = \frac{e^2}{4\pi\epsilon_0} \cdot \frac{Z_P Z_T}{R_0(A_P^{1/3} + A_T^{1/3})} \approx \frac{Z_P Z_T}{A_P^{1/3} + A_T^{1/3}} \quad \text{[MeV]}, \tag{3.2}$$

where Z_P, Z_T and A_P, A_T are the atomic and mass numbers of the projectile and the target nuclei, respectively, and R_0 is the radius parameter from the equation describing the radius of the nucleus $R = R_0 A^{1/3}$. Often, an interaction and fusion barrier model by Bass [Bass74] is used for more accurate estimates for heavy elements. The Bass model uses a two-body nuclear model derived from the liquid-drop model for the collision and takes into account the transfer of energy and angular momentum via friction when the two nuclei fuse together.

The two nuclei fuse into a compound nucleus (C^*, CN) with a high amount of excitation energy and angular momentum. The excitation energy of the compound nucleus is given by the equation

$$E^* = E_{\text{cm}} + Q, \tag{3.3}$$

where E_{cm} is the kinetic energy of the collision system in the centre-of-mass frame of reference. Here the Q value of the reaction is calculated from

$$Q = (m(a) + m(A) - m(C))\, c^2, \tag{3.4}$$

where $m(a)$, $m(A)$ and $m(C)$ are the masses of the projectile, the target and the compound nucleus, respectively. The kinetic energy that is expressed in the centre-of-mass frame of reference can be calculated from

$$E_{\text{cm}} = \left(\frac{m(A)}{m(a) + m(A)}\right) E_{\text{lab}}, \tag{3.5}$$

where E_{lab} is the kinetic energy of the projectile in the laboratory frame of reference.

After formation, the excess energy of the compound nucleus is quickly dissipated as illustrated in Fig. 3.1 by evaporation of particles such as neutrons or protons (b) and becomes the final product (B) that is called the evaporation residue (hereafter: ER, recoil). There are many possibilities for the total number and type of the evaporated particles (1n, 2n, 3n, xn, pn, 1p, pxn, α, ...) which are called reaction or evaporation channels. Therefore, different final nuclei are produced depending on the reaction channel. The reaction channel is selected by choosing the kinetic energy of the accelerated ion beam in such a way that the wanted number of evaporated particles and the excitation energy of the nucleus is optimised. After the evaporation, more energy is released by the "hot" and fast rotating nucleus by emitting high-energy statistical γ rays from E1 transitions followed by de-excitation of the yrast energy states towards the ground state.

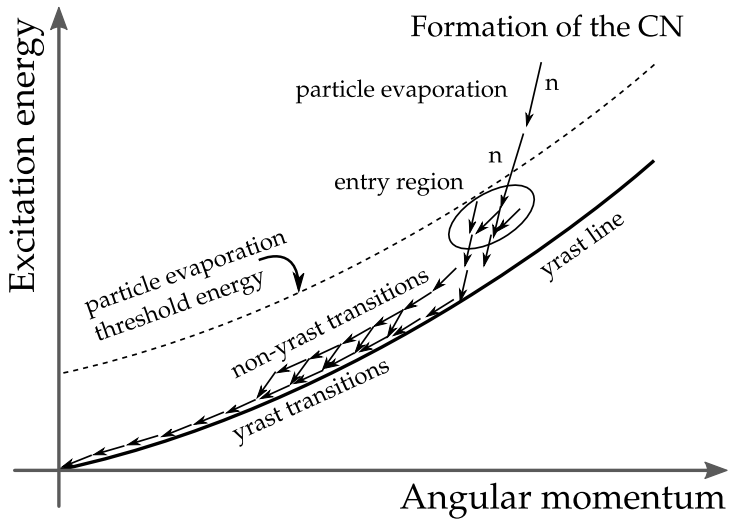

Figure 3.1. Schematic illustration of the energy dissipation in the fusion-evaporation reaction after the compound nucleus (CN) is formed. The CN releases its excitation energy first by evaporating particles until a threshold energy for evaporating more particles is reached. From the entry region the evaporation-residue cools down further by emitting statistical γ rays followed by more γ rays emitted from transitions in the non-yrast bands and the yrast line.

The cross section σ is an often used quantity that describes the probability that a particular final product is made in the fusion-evaporation reaction. It is calculated by

$$\sigma = \frac{R}{N_\mathrm{t} \cdot I_\mathrm{b}}, \tag{3.6}$$

where R is the total production rate of the evaporation residue, N_t is the number of target nuclei per unit area and I_b is the intensity of the ion beam impinging on the target. The number of target nuclei per unit area is calculated from

$$N_\mathrm{t} = \frac{\rho d}{A} N_A, \tag{3.7}$$

where N_A is the Avogadro's number, A is the mass number of the target and ρ, d are the density and thickness of the target material, respectively.

Combining the Equations 3.6 and 3.7 gives the relation

$$\sigma = \frac{RA}{\rho d N_A I_\mathrm{b}}. \tag{3.8}$$

3.2 Instrumentation

In majority of the cases the cross section to produce the desired fusion-evaporation residue is orders of magnitude lower than that of other reactions that can occur when the accelerated ion beam interacts with the target material. Reactions such as Coulomb excitation, transfer reactions and fission often have much higher cross sections than the fusion-evaporation channel of interest. Additionally, most of the beam particles actually pass through the target without interacting or are scattered without causing nuclear reactions.

In order to identify the recoils of interest and to perform measurements on them, they need to be separated from the enormous number of background events, various special tools designed specifically for that purpose have to be used. The experimental setup used in this study is shown in Fig. 3.2, where the RITU gas-filled recoil separator is coupled to the GREAT focal-plane spectrometer and the JUROGAM array (the predecessor of JUROGAMII). These devices are briefly presented in the following sections.

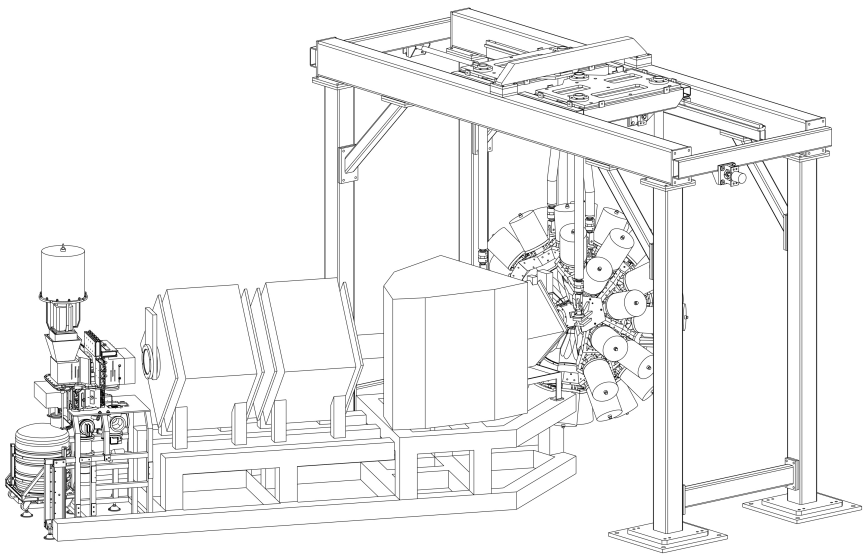

Figure 3.2. Schematic of the experimental setup consisting of the GREAT spectrometer (on the left), the RITU separator (in the middle) and the JUROGAM array (on the right). Figure courtesy of D. Seddon.

3.2.1 The RITU gas-filled recoil separator

The Recoil Ion Transport Unit (RITU) [Leino95] is a gas-filled recoil separator that is used to separate the fusion-evaporation residues from the primary beam and other unwanted reaction products and transport the recoils to the focal-plane for further measurements. The separator is placed downstream of the target position. It consists of a total of four focusing components that are in a $Q_vDQ_hQ_v$ configuration. The first magnetic quadrupole (Q_v) is vertically focusing and improves the acceptance of the separator. The dipole magnet (D) is the separating element that is used to separate ions according to their magnetic rigidity. The last two quadrupole magnets (Q_h, Q_v) are horizontally and vertically focusing, respectively.

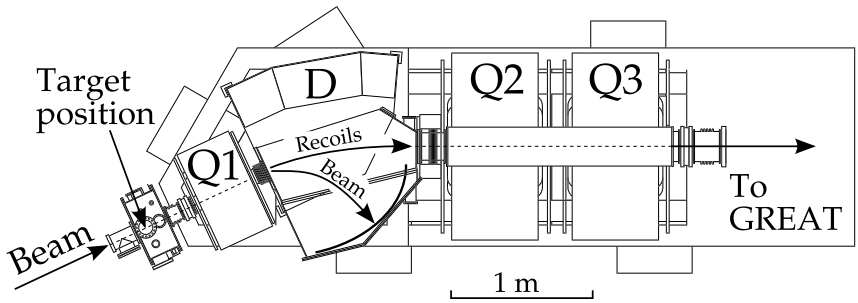

Figure 3.3. Schematic top view of the RITU gas-filled recoil separator.

The separation of the particles entering the recoil separator is based on their magnetic rigidities ($B\rho$) in the homogeneous magnetic field of the dipole as given by the equation

$$B\rho = \frac{p}{q} = \frac{mv}{Qe}, \tag{3.9}$$

where B is the magnetic field density, ρ is the radius of curvature of the particle trajectory and p, m, v and q are the momentum, mass, velocity and charge of the particle, respectively. The charge state of the particle is $Q = q/e$, where e is the elementary charge.

The internal volume of the separator is filled with a flow of helium gas with the pressure regulated at around 1 mbar. A pressure of about 0.6 mbar was used in the measurements of this work. Differential pumping is used to maintain the high vacuum at the beam line coming from the cyclotron to the separator. The recoils coming out of the target with various charge states undergo multiple charge-exchange collisions with the helium gas. As a result, the recoil ions follow a trajectory corresponding to the average charge state in the gas and are more focused at the focal plane compared to a vacuum-mode separator. In addition, the gas provides a cooling effect on the target material preventing it to be damaged by heat during the irradiation.

The efficiency of transporting the fusion recoils to the focal plane, *i.e.* the transmission, depends strongly on the angular spread, charge state and velocity of the recoils. The angular acceptance of the RITU separator is about 8 msr, which requires that the recoils that are detected at the focal plane have had to travel in nearly the same direction as the beam into the separator. The maximum acceptable angle in the horizontal direction is ±25 mrad in the vertical direction ±85 mrad ≈ ±5° [Sarén11].

3.2.2 The GREAT focal-plane spectrometer

After passing through the recoil separator, the evaporation-residues are focused at the focal plane of RITU where a set of detectors called The Gamma Recoil Electron Alpha Tagging (GREAT) spectrometer [Page03] is located. A schematic of the spectrometer is shown in Fig. 3.4 and it consists of a Multi-Wire Proportional Counter (MWPC), two adjacent Double-sided Silicon Detectors (DSSDs), twenty-eight silicon PIN diodes, a Planar germanium detector and three additional germanium detectors.

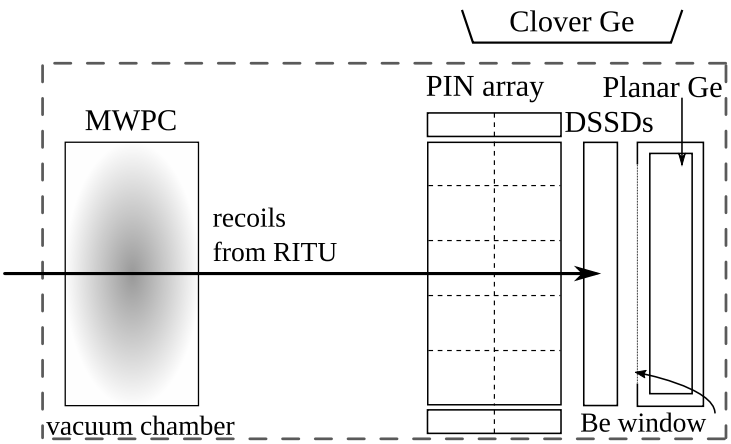

Figure 3.4. Schematic diagram of the recoils arriving from the RITU separator and entering the GREAT spectrometer as seen from above. The detector components are described in more detail in the text.

The MWPC is a gas-counter filled with isobutane that is placed upstream from the DSSDs. The detector provides a measurement of the energy loss (ΔE) of the recoils passing through it. In addition, timing information about the flight time of the ions from the MWPC to the DSSDs is recorded. Thin Mylar windows are used to separate the gas volume from the helium gas volume of RITU and the vacuum volume of GREAT.

The two adjacent DSSDs are the main detector instruments that are used in GREAT. The evaporation residues arriving from RITU are implanted and stopped in one of

the detectors. The energies of subsequent decays after the implantation can then be measured. The detectors each have an active area of $60 \times 40\,\mathrm{mm}^2$. The thickness of the detectors used in this work was 300 µm. The $2 \times 60 = 120$ vertical (X) and 40 horizontal (Y) strips in both of the DSSDs make a total of 4800 positions (pixels) that can be used for correlation analysis. The strips are electronically segmented with a strip pitch of 1 mm. There is a gap of about 4 mm between the two detectors.

Upstream of the DSSDs in a box configuration are 28 silicon PIN diodes. The active area of one detector element is $28 \times 28\,\mathrm{mm}^2$ with a thickness of 500 µm. The PIN diodes having a geometrical efficiency of about 30% are used to detect internal-conversion electrons and α particles that escape from the DSSDs in the backward direction.

A double-sided germanium strip detector, or the Planar detector, is placed directly behind the DSSDs inside the same vacuum chamber. A thin window made of beryllium is used as an entrance window to the detector in order to minimise the attenuation of X-rays and low-energy γ rays. The active area of the rectangular detector is $120 \times 60\,\mathrm{mm}^2$ with a thickness of 15 mm. The electrical segmentation is made to 24 strips in the horizontal direction (X) at the front face and 12 strips in the vertical direction (Y) at the back face with a 5 mm strip pitch.

A segmented large-volume GREAT Clover germanium detector is placed above the DSSDs outside of the vacuum chamber housing. The four crystals in this detector are each segmented in four, have a diameter of 70 mm and a length of 105 mm. The detector is surrounded by a Compton-suppression shield made of bismuth germanate (BGO). Only the core signals from the germanium crystals were read out and the BGO shield was used only as a passive shield in this work. Two Clover-type detectors [Duchêne99] were positioned at the sides of the DSSDs outside of the vacuum chamber. The absolute efficiencies of the detectors relies on simulations made in Geant3 [Andreyev04].

3.2.3 The JUROGAMII array

Prompt γ rays that are emitted at the target position were detected with an array of Compton-suppressed High-Purity germanium detectors (HPGe) called the JUROGAMII array illustrated in Fig. 3.5. The array consists of a total of 39 germanium detectors arranged in four rings at different angles (θ) relative to the direction of the ion beam. The 24 Clover-type detectors [Duchêne99] are positioned in two rings at angles of 75.5° and 104.5°. Two more rings consist of 15 of either EUROGAM Phase1 [Beausang92] or GASP [Rossi Alvarez93] type of detectors at angles of 133.57° (10 detectors) and 157.6° (5 detectors). All of the germanium detectors in the array are equipped with active Compton-suppression shields made of bismuth germanate (BGO) and Hevimet collimators in front of the detectors to improve the peak-to-total ratio by rejecting (veto) events where a Compton scattered γ ray is detected in the surrounding shield. The add-back method of summing the coincident γ-ray energies in separate crystals in the same Clover detector within a 200 ns time window was used in this work.

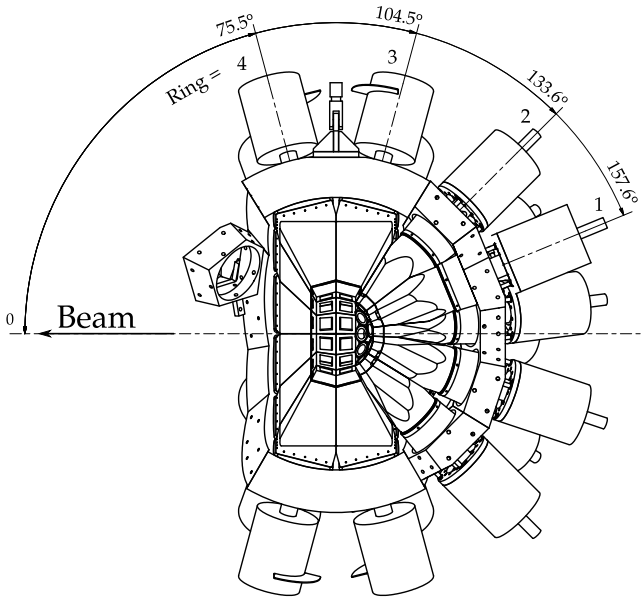

Figure 3.5. Schematic representation of the right hemisphere of the JUROGAMII array of Compton-suppressed High-Purity germanium (HPGe) detectors.

The ERs that recoil out of the target material typically travel at a velocity of a few percent of the speed of light (c). Therefore, the measured γ-ray energies in the laboratory frame of reference have to be corrected for Doppler shift to recover the correct energies of the γ-ray transitions (E_γ). The correction is made using the equation [Kantele95]

$$E_\gamma^{'} = E_\gamma \frac{\sqrt{1-\beta^2}}{1-\beta\cos\theta} \approx E_\gamma(1+\beta\cos\theta), \tag{3.10}$$

where $E_\gamma^{'}$ is the measured (shifted) γ-ray energy, $\beta = v/c$ and v is the velocity of the recoil. In this work the velocity of the recoils used in the Doppler correction was found iteratively by obtaining as narrow as possible peak shapes after the calculated correction.

The energy calibration and the relative efficiency calibration of the germanium detectors were made using standard radioactive ^{133}Ba and ^{152}Eu calibration sources. The EFFIT program from the RadWare software package [Radford95b, Radford95a] was used to normalise the data sets measured using the two sources and to fit the relative efficiency as a function of the γ-ray energy of the form [Radford95b]

$$\epsilon(E_\gamma) = \exp\left\{\left[\left(A+Bx+Cx^2\right)^{-G}\left(D+Ey+Fy^2\right)^{-G}\right]^{-1/G}\right\}, \tag{3.11}$$

where $x = \ln(E_\gamma/100)$, $y = \ln(E_\gamma/1000)$, E_γ is the γ-ray transition energy in units of keV and A, B, C, D, E, F and G are the parameters to be fitted.

3.2.4 Total-data readout (TDR) data-acquisition system

The energies from all of the detector channels of GREAT and JUROGAMII are read out independently using a Total-Data Readout (TDR) [Lazarus01] data-acquisition system. The most important and valuable feature of the acquisition system is that it is triggerless and the data is timestamped using a 100-MHz clock giving a time resolution of 10 ns. This eliminates the common deadtime caused when a conventional hardware trigger is used. When all of the time-ordered data is stored, it makes the offline data-analysis more flexible and allows the experiment to be replayed afterwards with the possibility of freely adjusting the search times, triggering and using various analysis methods in software.

The signal paths in the TDR data-acquisition system is shown schematically in Fig. 3.6. In this study the DSSDs and the MWPC were instrumented with analogue electronics where the Analogue to Digital Converters (ADC) were fed with the signals from the shaping amplifiers, Timing Filter Amplifiers (TFA) and Constant Fraction Discriminators (CFD). All of the germanium detectors and the PIN diodes were instrumented with digital Lyrtech/Nutaq VHS-ADC cards. The energies of the digital detector signals were determined by using a Moving-Window Deconvolution (MWD) [Georgiev93] algorithm programmed to the field-programmable gate array (FPGA) circuit of the VHS-ADC cards.

The separate data streams from the ADC cards are time-ordered by a Merge software and saved to disk in a binary format. The temporal and spatial correlations of the recoil implantations, decays and γ rays in the time-ordered event data were analysed using the GRAIN [Rahkila08] software package in this work. The RADWARE software [Radford95b, Radford95a] were used to fit peaks in the measured γ-ray spectra.

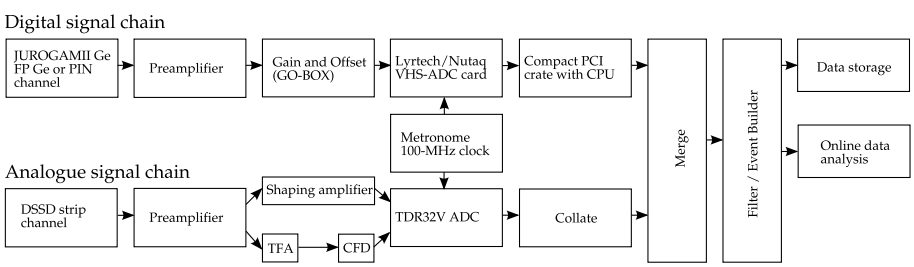

Figure 3.6. Block diagram of the TDR electronics illustrating the digital and analogue signal paths of the different detector channels.

3.3 Data-analysis methods

3.3.1 The recoil-decay tagging (RDT) technique

The recoil-decay tagging (RDT) [Schmidt86, Simon86, Paul95] technique is based on using temporal and spatial correlations of events in the measured data. The method is extremely useful in extracting information on nuclei from fusion-evaporation channels with very low cross sections from a dominant background of other reaction products. The technique allows to associate the prompt γ rays emitted by the recoil earlier in time at the target position with the recoil implantation and a subsequent decay signals detected in the detectors of the GREAT spectrometer. A cleaner subset of the prompt γ-ray data is obtained by requiring the characteristic decay event that allows the γ rays to be tagged to a specific nucleus.

The use of the technique is illustrated in Fig. 3.7. The temporal correlations in the data stored with the TDR data-acquisition system are possible because a timestamp is associated with each event from the detectors. The recoil selection and identification (gating) are made by using various conditions on the data in the analysis phase. Because the flight time through RITU is about 1 µs, the prompt γ rays associated with each recoil are found by searching backwards in time from a recoil implantation event in the data. After a recoil implantation a decay event such as α decay is searched for in the same pixel of the DSSD detector. If only the recoil identification without the decay information is used to select the prompt γ rays, the method is called *recoil gating*. Furthermore, isomeric states and decay properties can be studied at the focal plane following the recoil implantation by searching for more correlated events.

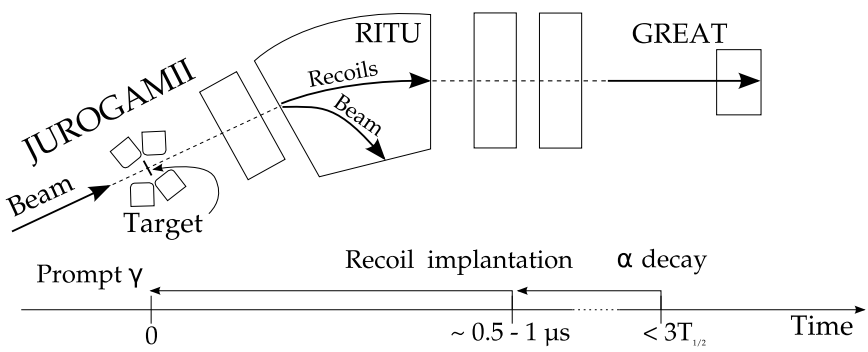

Figure 3.7. Schematic illustration of the recoil-decay tagging technique with the experimental setup of this work. The prompt γ rays emitted at the target position are detected in JUROGAMII and selected by searching backwards in time of an implanted recoil event at the focal plane of the RITU separator. A characteristic α decay following the recoil implantation in the same pixel of the DSSD is used to identify and tag the recoil event and its prompt γ rays.

The half-life, decay branches and production cross section of the nucleus of interest together with the total counting rate of the DSSDs at the focal plane of the recoil separator may impose limitations on the use of the RDT method. An increasing amount of random correlations and unwanted background will result if the half-life of the decaying nucleus is long compared to the counting rate in the individual pixels of the DSSDs. Thus, resolving a clean γ-ray spectrum or determining the half-life of the nucleus can become challenging tasks that may require the use of some carefully selected data analysis methods that are introduced in the following sections.

3.3.2 Half-life determination

Information on the decay times of radioactive decays in the DSSDs at the focal plane of RITU can be extracted by searching for temporally correlated events occurring in the same pixel of the DSSD. Typically, a search for correlated decay events following a recoil implantation within a defined time window is used to determine the half-life of a radioactive species. The length of the chosen search time depends on the half-life of the species of interest. Usually a search time of three or up to five half-lives is used in order to observe the vast majority of the decay events from the activity. The half-life can be then extracted from the measured time differences between the recoil implantation and the decay events using different analysis methods.

The selection of the best method to use in each particular case depends on the level of statistics and the random correlation probabilities in the measurement. A random correlation is an unwanted effect caused by an event occurring between the correct recoil implantation and the decay event. The probability for random events to occur depends on the count rate of each individual pixel in the DSSDs. Random correlations can cause the observed half-life to be shorter than it actually is. On the contrary, losses of real events caused by dead time in the data-acquisition system increase the observed half-life. The most commonly used methods and their applicability to different scenarios to determine the mean lifetime and the half-life are presented in the following sections. The same methods apply also when determining the half-lives of excited states such as isomeric states in cases where the search for correlated events is made in a similar manner.

The maximum-likelihood method

The most simple and often used method to extract the mean lifetime $\bar{\tau}$ of a radioactive species is the maximum-likelihood method that has been demonstrated for this type of specific application in [Schmidt84]. In this method the mean lifetime is calculated as an arithmetic mean of all of the measured time differences t_i between the recoil

implantation and the decay as

$$\bar{\tau} = \frac{1}{N}\sum_{i=1}^{N} t_i, \tag{3.12}$$

where N is the total number of observed correlated decay events. The uncertainty of the mean lifetime is asymmetric because of the probability density distribution, and the upper (τ_+) and lower (τ_-) limits corresponding to a $1\sigma = 68\%$ confidence limit are given by the approximations [Schmidt84]

$$\tau_+ \approx \frac{\bar{\tau}}{1 - \frac{1}{\sqrt{N}}} \quad \text{and} \tag{3.13}$$

$$\tau_- \approx \frac{\bar{\tau}}{1 + \frac{1}{\sqrt{N}}}, \tag{3.14}$$

that apply well for cases where $N \geq 10$. For large N the standard deviations converge to the expected dependence on $\sqrt{N}$. In cases of very small number of events ($N << 10$), the uncertainties have to be calculated exactly.

The maximum-likelihood method is best used with low statistics and in event-by-event analysis. Furthermore, the following particular requirements have to be met in order to be able use Equation 3.12. The number of random correlations has to be negligible and radioactive decays originated from only one species must be present. The search time for the correlations must be long enough to cover most of the decay events of interest. For example, using search times of $3 \times T_{1/2}$ and $5 \times T_{1/2}$ cover approximately 87.5% and 96.9% of the decay events, respectively.

The exponential decay-curve method

In the case of large level of statistics, it is convenient to sort the individual decay times t_i into a histogram of the number of decays within constant time intervals (bins) of width Δt. The obtained histogram has a shape of a single exponentially decaying function if there are no contributions from other radioactive species or randomly correlated events. However, some random correlations often arise due to the manner in which the correlation search is performed and there is a finite probability that an unwanted event can occur between, for example, a real recoil and a decay event pair, or that an event can be missed due to the dead time and other electronic effects.

The contribution of the random background can make the experimentally observed half-life appear shorter than it actually is ($\lambda_{\text{obs}} = \lambda_{\text{real}} + r$). In order to extract the real decay constant of a single source of activity from a time difference histogram, a simultaneous least-squares fit can be made using a double exponential function of the form [Leino81, Chatillon06]

$$f(t) = ae^{-(\lambda+r)t} + be^{-rt}, \tag{3.15}$$

where a, b are parameters used in the fitting, λ is the decay constant of the activity and r is the apparent rate of the component arising from random correlations.

Another way to extract the decay constant is by linearising the fitting procedure by presenting the number of events in the histogram on a logarithmic scale (on the y-axis). In this representation the data points should follow a straight line with a slope that directly gives the decay constant. In addition, contributions from other radioactive species or random background can be identified and extracted.

The applicability of this method is limited to cases where the level of statistics is high enough so that the statistical fluctuations in the number of events in the selected time intervals are small.

The logarithmic time-scale method

An alternative way to represent the individual decay times t_i is to use the logarithmic time-scale method [Schmidt84, Schmidt00] where the number of decay events are sorted in a histogram with logarithmic time bins. This allows different radioactive species that have different decay times to be discriminated. In addition, the logarithmic scale allows a very broad range of decay times to be presented with only a moderate number of channels for the histogram.

The corresponding probability density distribution in the logarithmic time scale is obtained using the substitution $\Theta = \ln t$ from Eq. 2.13 and is given by

$$\left|\frac{dN}{d\Theta}\right| = \lambda N_0 e^{-\lambda e^{\Theta}} e^{\Theta}. \tag{3.16}$$

The obtained distribution is a bell-shaped and asymmetric curve with a maximum positioned at $\Theta_{\max} = \ln\left(\frac{1}{\lambda}\right)$. It should be noted that the shape of this curve does not depend on the value of λ. However, it determines the position of the maximum of the curve which makes it a useful tool in extracting the decay constant of the activity of interest by fitting a function of the form given by Eq. 3.16. The width of the distribution is universal and its standard deviation is $\sigma_{\Theta} \approx 1.28$. The height of the distribution scales with the number of observed decay events N_0.

In the case that multiple radioactive species with different decay constants λ_i are present in the spectrum, a sum of functions obtained from Eq. 3.16 can be used for the fitting procedure of the form

$$f(\Theta) = \sum_{i=1}^{m} \lambda_i N_i e^{-\lambda_i e^{\Theta}} e^{\Theta}, \tag{3.17}$$

where m is the number of different radioactive species.

The applicability of this method is better suited to low-statistics cases than the exponential decay-curve method because of the difference in the binning of the histogram.

However, the fitting procedure can be done reliably only if there is enough statistics to form the shape of the curve and the statistical fluctuation in the number of events in each bin is small. In cases of small level of statistics such as in the observation of only a few decay events of superheavy elements, the distribution from Eq. 3.16 is often plotted using a half-life obtained from the maximum-likelihood method together with the individual lifetimes in the same figure. This allows to assess the quality of the data. Note that the number of observed decay events (N_0) should be scaled according to the binning of the histogram. Furthermore, the properties of this method and the shape of the distribution can be exploited in a so-called logarithmic time-scale test.

The logarithmic time-scale test

The feature that the universal width of the logarithmic time distribution is constant is exploited in the logarithmic time-scale test [Schmidt00]. The test is useful to estimate whether the observed decay events originate from one activity or if there is another species contributing to the measurement. If only one radioactive species is present in the measurement, the standard deviation of the experimental logarithmic time distribution $\sigma_{\Theta_{\mathrm{exp}}}$ approaches the theoretical value of $\sigma_\Theta \approx 1.28$ when the number of events is large. The standard deviation of the logarithm of the experimental time distribution is calculated with

$$\sigma_{\Theta_{\mathrm{exp}}} = \sqrt{\frac{\sum_{i=1}^{N}\left(\Theta_i - \bar{\Theta}_{\mathrm{exp}}\right)^2}{N}}, \tag{3.18}$$

where

$$\bar{\Theta}_{\mathrm{exp}} = \frac{\sum_{i=1}^{N}\Theta_i}{N}, \tag{3.19}$$

and $\Theta_i = \ln(t_i)$, where t_i is the measured lifetime of event i and N is the total number of events.

The expectation value of $\sigma_{\Theta_{\mathrm{exp}}}$ is lower than 1.28 with a low number of events ($N << 100$). The 90% confidence limits along with the expected standard deviation of $\sigma_{\Theta_{\mathrm{exp}}}$ for a small number of events ($N < 100$) are calculated in [Schmidt00] using Monte Carlo techniques. The experimental $\sigma_{\Theta_{\mathrm{exp}}}$ falling below the confidence limit for a certain N can be rejected with less than 5% error to originate from radioactive decay. In this case it may be that the search time was not long enough or the measurement is not sensitive to the whole range of the lifetimes, *e.g.* if the lifetime is too short to measure it. Another possibility is that there is periodic noise present in the system creating at least part of the events as random correlations. Values above the confidence limit may indicate that there is another radioactive species with different half-life present in the measured set of events. If the $\sigma_{\Theta_{\mathrm{exp}}}$ value passes the test by falling between the confidence limits, it is very likely that the set of events originate from a single radioactive species. However, it should be noted that passing the test is only consistent with 90% confidence with the assumption of a single radioactive species but it does

not guarantee that. It should also be noted that the test is unable to distinguish if two activities that have similar or the same half-life are present in the measurement.

Recently, a further generalisation of the logarithmic time-scale test has been proposed and applied to assess the validity of measured decay chains and their assignments to superheavy elements 115 and 117 [Forsberg16a, Rudolph16, Forsberg16b].

3.3.3 Cross-section estimation

Estimating the cross section of a fusion-evaporation reaction channel using Eq. 3.6 requires that the production rate of the evaporation residue R, the beam intensity I_b and the number of target nuclei per unit area N_t remain constant. However, in reality, the beam intensity fluctuates throughout the long experimental runs. Consequently, the production rate of the recoils also fluctuates. In addition, the target may be damaged from the irradiation with the ion beam in such a way that target atoms are sputtered out of the target. Thus, N_t is reduced over time. Furthermore, the production rate depends on the thickness of the target and the beam energy that must be constant throughout the experiment.

There is no direct, constant and precise monitoring of the beam intensity currently available at the RITU setup. Instead, the simplest way to estimate the average beam intensity is to occasionally stop the beam and measure the electrical current induced by the beam in a Faraday cup at the target position. In this work the beam intensity was increased in steps in the beginning of the measurements and was measured to provide a calibration and normalisation method to relate various detector count rates to the absolute electrical beam current[1]. An example of such a measurement is shown in Fig. 3.8(a) from the experiment where the fusion reaction ^{48}Ca+^{198}Pt was used where the total count rate measured at the focal plane DSSDs of the recoils that were identified mostly as transfer-reaction products is shown against time. The measured electrical beam currents at three different steps (20, 40 and 54 pnA) are indicated together with the corresponding averages of the count rates marked with blue horizontal lines. The lengths of the lines correspond to the time intervals used to calculate the average count rates.

The calibration of the count rates to the measured absolute beam current is made with a linear least-squares fit as shown in Fig. 3.8(b). After normalising the count rate to an absolute beam intensity using the obtained calibration, the total beam dose N_{beam} can be calculated by numerical integration of the total number of counts over the time of the measurement. The beam dose gives the number of beam particles incident on the target during the irradiation time of t_b. It can also be estimated with the average beam intensity by using the relation $N_{beam} = \bar{I}_b \cdot t_b$.

[1] Typically measured in units of pnA = $^{10^{-9}}/_{1.6022\cdot 10^{-19}}$ particles/s.

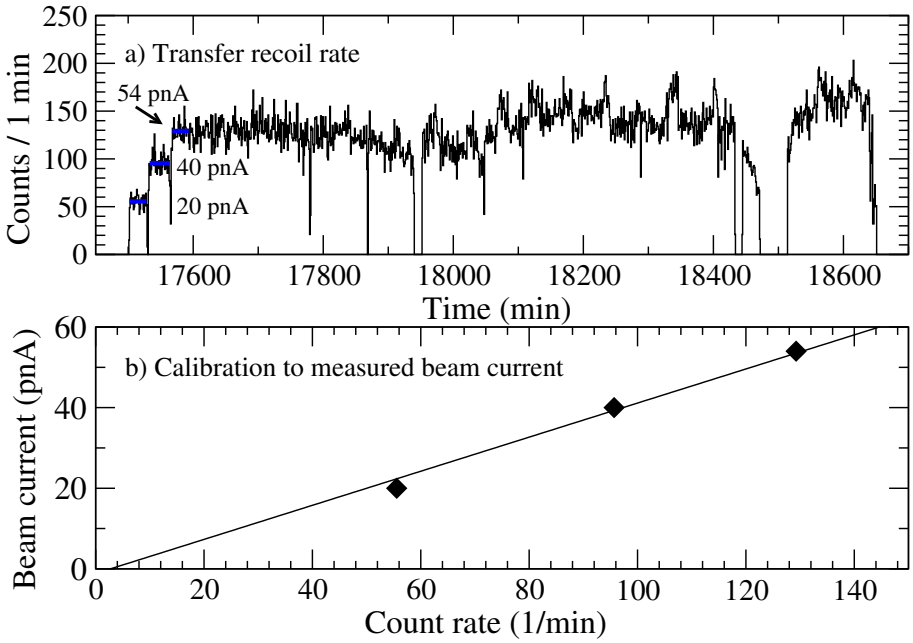

Figure 3.8. An example from the ^{48}Ca+^{198}Pt reaction of (a) the total count rate of mostly transfer-reaction products during a 19 h measurement in the DSSDs and (b) the calibration to the absolute beam current that was used to estimate the total beam dose. The beam intensities measured in a Faraday cup are indicated in (a) as electrical currents in units of pnA where the blue horizontal lines correspond to the averaged values of the corresponding count rate.

The production rate R can be estimated by determining the total number of evaporation residues that were produced in the experiment N_{tot} in time t_{b} from $R = N_{\text{tot}}/t_{\text{b}}$. However, some of the recoils never make it to the focal plane spectrometer and its detectors or their decays are not detected due to limitations of the experimental setup. These limitations are taken into account in the calculations as efficiencies ϵ_i.

The transmission efficiency of the RITU separator ϵ_r gives the percentage of the recoils that are transported through the separator. It depends mostly on the kinematics of the chosen fusion-evaporations reaction and the thickness of the target that determine the angular spread of the recoils. Some of the recoils ($\approx$ 30%) are also stopped in the gas counter (MWPC). Typically, in the heavy element region the transmission is $\epsilon_{\text{r}} \approx$ 30–50%.

In case we use the detected α particles to estimate the total number of nuclei that have decayed at the focal plane, we must take into account the full-energy α detection efficiency of the DSSD detectors of about $\epsilon_\alpha \approx 55\%$. In addition, the α-decay branch (b_α)

of the nucleus has to be known. The α detection efficiency is due to the measurement geometry and because the recoils are implanted usually only 5–10 µm in to the DSSD. The α particles that recoil backwards from the detector deposit only small part of their full energy in the DSSD and escape the detector.

The coverage of the DSSD detectors ϵ_c is the percentage of the area that is actually covered with active detector elements at the focal plane the recoils are focused. The distribution of the recoils forms a two-dimensional Gaussian distribution in X and Y directions, however, the whole distribution is not covered by the two DSSDs. In addition, some of the DSSD strips are usually not working in an experiment, there are gaps between the adjacent strips and a larger gap between the two adjacent DSSD detectors. In typical measurement conditions the efficiency from the coverage is $\epsilon_c \approx 80\%$.

Taking into account the relevant efficiencies the cross section estimate given by Eq. 3.8 becomes

$$\sigma = \frac{1}{\epsilon_r \epsilon_c \epsilon_\alpha b_\alpha} \frac{N_\alpha}{N_{\text{beam}}} \frac{A}{\rho d N_A}, \tag{3.20}$$

where ρd is the surface density of the target. The surface density describes the thickness of the target material and is usually given in units of µg/cm^2 or mg/cm^2.

Chapter 4

Discovery of the new isotopes ^{240}Es and ^{236}Bk

In this chapter the details of the experiment, data analysis, results and discussion related to the decay spectroscopic study and the synthesis of the new neutron-deficient isotopes ^{240}Es ($Z = 99, N = 141$) and ^{236}Bk ($Z = 97, N = 139$) are presented. The main aim of the experiment was to identify the new isotope ^{240}Es and to study its decay properties. Additionally, relatively high ECDF probabilities were predicted for both of the new isotopes based on earlier measurements in the heavier odd-odd einsteinium and berkelium isotopes. The half-lives and proposed decay schemes of the new isotopes are presented along with measurements of the ECDF probabilities.

4.1 Experimental details

The experiment was carried out with the RITU gas-filled recoil separator coupled to the GREAT focal-plane spectrometer system at the Accelerator Laboratory of the Department of Physics, University of Jyväskylä. The JUROGAMII germanium array was not used in this experiment, which was focused on decay spectroscopy of the nuclei of interest and to maximise their production with high beam intensities. Two bismuth-germanate (BGO) scintillator detectors were placed at the target position to measure the rate of γ rays emitted when the beam interacts with the target material. The rate information was used to determine the beam intensity and total dose needed for the calculation of cross section estimates. In order to reduce the γ-ray background in the focal plane detectors when the high-intensity beam impinges on the target, some additional shielding provided by blocks made of paraffin was constructed close to the dipole chamber.

The new neutron-deficient isotope ^{240}Es was synthesised in the fusion-evaporation reaction ^{209}Bi(^{34}S,3n)^{240}Es. The ^{34}S ion beam with a charge state of 7+ was produced in an ECR ion source and accelerated to final energies of 174 and 178 MeV by the K-130 cyclotron. Carbon degrader foils with thicknesses of 400 and 200 μg/cm^2 were used on the upstream side of the target to reduce the latter beam energy of 178 MeV down to 172 and 175 MeV, respectively, for part of the measurements. Typical beam intensities during the experiment were 100–200 pnA measured at a Faraday cup upstream and close to the target position. The current corresponds to a rate of the beam particles of about 0.6–1.2 · 10^{12} 1/s incident on the target. The beam energies, targets and degraders used and corresponding excitation energies of the compound nucleus ^{243}Es* are listed in Table 4.1.

Table 4.1. A summary of the fusion-evaporation reactions used in the synthesis and decay spectroscopic study of the new isotope ^{240}Es. The given energies correspond to energies at the centre of the target.

Final nucleus	Beam isotope	Target isotope	Thickness (μg/cm^2)	C-degrader (μg/cm^2)	E_{beam} (MeV)	E^* (MeV)	Reaction channel
^{240}Es	^{34}S	^{209}Bi	510–520	0	174	34	3n
^{240}Es	^{34}S	^{209}Bi	510–520	0	178	39	3n
^{240}Es	^{34}S	^{209}Bi	510–520	200	175	36	3n
^{240}Es	^{34}S	^{209}Bi	510–520	400	172	35	3n

The bismuth targets were evaporated on to 50 μg/cm^2 carbon foils and came in the chemical form of Bi_2O_3 with thicknesses of about 570–580 μg/cm^2 (Bi: 510–520 μg/cm^2) and were rotated during the measurement in order to prevent damage due to the irradiation by the beam. The targets were positioned so that the carbon backing foil was facing the entrance to the RITU separator (downstream), therefore, acting as a "charge reset" foil for the beam. The pressure of the helium gas inside the dipole chamber of the separator was regulated to be 0.6 mbar. The magnetic dipole (D) was tuned to match a magnetic rigidity of about 2.0 Tm in order to guide the ERs to the focal-plane of RITU and to focus the Gaussian distribution of the recoils evenly on the DSSDs.

During parts of the same experimental run the fusion reaction ^{34}S+^{208}Pb and also a ^{36}S ion beam was used in the fusion reactions ^{36}S+^{206}Pb and ^{36}S+^{208}Pb in order to produce neutron-deficient isotopes of ^{239,240,241,242}Cf in the neutron evaporation channels. The Pb targets used were in the form ^{206,208}PbS with thicknesses of 570–610 μg/cm^2 (Pb: 500–530 μg/cm^2). In the beginning and in the middle of the experiment a ^{181}Ta target with a thickness of 1 mg/cm^2 was mounted and irradiated with ^{36}S ion beam for calibration purposes. The RITU magnets were tuned to guide the resulting fusion-evaporation products such as ^{212,213}Ac to the focal-plane setup.

4.1.1 Energy calibrations

The horizontal (Y) strips on the back (downtream) side of the DSSDs were amplified with low gains in order to measure high-energy events such as fission and the high-energy recoils from transfer reactions. The vertical (X) strips on the front (upstream) side were used with higher gains to be sensitive to measure α particles and recoils from fusion reactions.

Both sides of the DSSDs were calibrated by using the known α-particle energies from the α decays of the transfer reaction products ^{213,212}Rn (8088 keV, 6264 keV), ^{212,211}At (7669.3 keV, 5869.5 keV) and ^{211}Po (7450.3 keV). To improve the statistics and to allow for an improved internal calibration, the transfer reaction products were guided to the focal plane and focused on the DSSDs by tuning the RITU magnet settings accordingly at the end of the experiment . The recoil energy difference when the same calibration is applied for α decays of both $A \approx 210$ and $A \approx 240$ nuclei was not taken into account in this study. The systematic error caused by this effect is about 6 keV and taken into account in the final uncertainty. The energy resolution of the DSSDs was about 25 keV at 8.09 MeV when determined from the summed α-particle energy spectrum of all of the X strips.

The PIN silicon detectors were calibrated with an external mixed three-line α source. The Planar detector was calibrated using the γ rays from an open ^{133}Ba source placed inside the vacuum chamber upstream from the DSSDs. The two Clover detectors placed at the sides of the focal-plane vacuum chamber and the large-volume GREAT Clover on the top of the chamber were calibrated using ^{152}Eu and ^{133}Ba sources placed outside the vacuum chamber.

4.2 Results

The analysis of the experimental data was performed using the GRAIN software package. The software trigger conditions for creating the events was set on any of the individual DSSD strips with an event length of 10 µs offset by a −2 µs delay. The triggering of another event within a 8 µs time window was prevented by using an artificial deadtime condition on the software trigger. In addition to the typical statistical analysis methods, event-by-event analysis was used to verify the correlations in the data. The GRAIN software was used as a preparser and as triggering software to sort the relevant data to list mode that was analysed by hand. The event-by-event analysis allowed a more detailed inspection and careful selection of the correlated events. The time structure of the event definition is illustrated in Fig. 4.1.

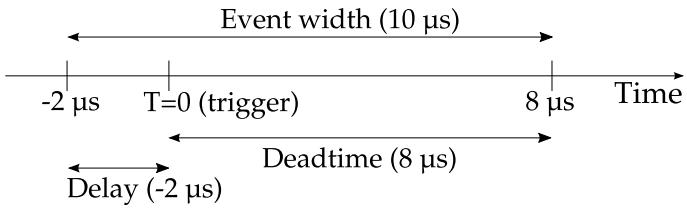

Figure 4.1. Definitions of the event structure that was used in the data analysis in the GRAIN software.

4.2.1 Recoil identification

The fusion-evaporation recoils (ERs) from the ^{34}S + ^{209}Bi reaction were distinguished from other reaction products by using the time-of-flight information (ToF) between the MWPC and the DSSD and the final energy deposit in the DSSD (E) measured on the X side of the detector. A matrix of the ToF versus energy deposit in the DSSD is shown in Fig. 4.2. The approximate location of the two-dimensional gate condition that was placed for the ERs is indicated by the red area. The recoils that did not pass the conditions were not considered as ERs and were discarded from further correlation analysis. The location of the final gate used in the analysis was further supported by using the more abundant information about the correlated recoils obtained from the observed ER-α(^{239,240}Cf) pairs in the ^{36}S+^{206}Pb and ^{34}S+^{208}Pb fusion reactions.

Similar to Fig. 4.2, a recoil identification matrix when using the Y side of the DSSD is shown in Fig. 4.3 where the final energy deposit of the recoils can be seen in a larger energy range up to 40 MeV. The strongest component in the recoil spectrum was identified as recoils originating from transfer reaction products (hereafter: TR) that were mostly fast and deposited a high energy in the DSSD. The approximate location of the two-dimensional gate condition that was placed for the TRs is indicated by the red area. Most of the TRs were followed by characteristic α decays of the transfer products within a short time window of $\Delta t_{\mathrm{TR}-\alpha} \leq 2$ s in the same pixel of the DSSD in the correlation analysis. Thus, in the further ER-α correlation analysis only the α particles without correlations to such TRs within 2 s were included. Note that the two-dimensional gates placed in Figs. 4.2 and 4.3 are partly overlapping. Consequently, the recoils that were considered as TRs did not pass the gate conditions set for the ERs.

Compared to the more abundant TRs that were present in the experiment due to the chosen reaction, the ERs from the fusion reactions have a more well-defined kinetic energy and a longer time-of-flight. Although the ERs were not completely separated from the low-energy tail of the TRs by the recoil separator as seen in Fig. 4.2, more stringent conditions on the energy and time-of-flight could be applied for them. Part of the low-velocity component of the TRs passes through the energy and time-of-flight gate conditions set for the ERs. Most of the observed transfer-reaction products were

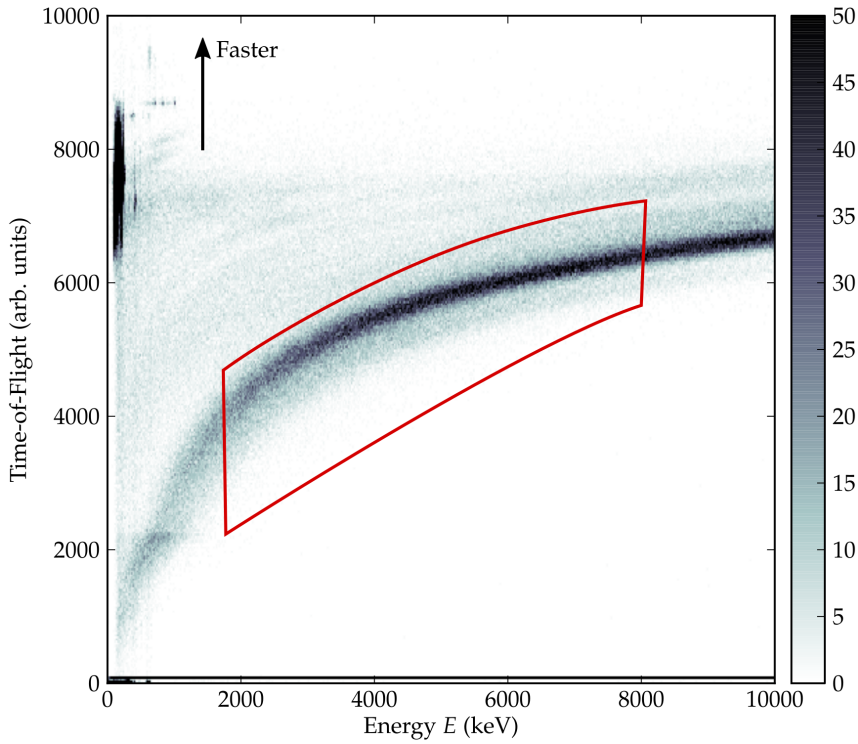

Figure 4.2. Fusion-evaporation residue (ER) identification matrix in the ^{34}S + ^{209}Bi reaction using the E-ToF method. The energy in the DSSDs is measured from the X side of the detector. The approximate gate used in the analysis is indicated by the red region. Please see the text for further details.

distributed in the low-rigidity side of the DSSDs (right-hand side when looking towards the detector from the separator side). Therefore, the five X strips at the end of the low-rigidity side of the rightmost DSSD were not used in the correlation analysis due to the high rate of TRs.

4.2.2 α-particle energy spectrum

The energy spectrum of the α particles from the ^{34}S + ^{209}Bi reaction measured in the DSSDs vetoed with the gas counter (MWPC) and the Planar detector signals is shown in Fig. 4.4. The events in the spectrum were considered to originate mostly from the α decay of the implanted nuclei (hereafter also called: α-like events). Several contaminant peaks that appear in the spectrum were identified in the ER-α correlation analysis and were assigned to α decays of ^{214m}Fr ($T_{1/2}$ = 3.35 ms), ^{214}Fr ($T_{1/2}$ = 5.0 ms), ^{213}Rn ($T_{1/2}$ = 19.5 ms), ^{212m}At ($T_{1/2}$ = 314 ms), ^{212}At ($T_{1/2}$ = 5.0 ms), ^{211m}Po ($T_{1/2}$ = 25.2 s)

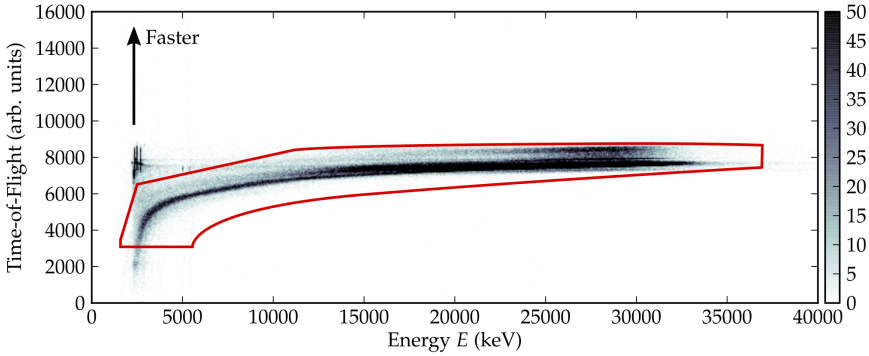

Figure 4.3. Transfer-reaction product (TR) identification matrix in the ^{34}S + ^{209}Bi reaction using the E-ToF method. The energy in the DSSDs is measured from the Y side of the detector. The approximate gate used in the analysis is indicated by the red region. Please see the text for further details.

and ^{211}Po ($T_{1/2}$ = 516 ms). Their recoils (herafter called: transfer recoils, TRs) had mostly high-energy deposit as measured in the DSSDs and short time-of-flight (see Fig. 4.3) indicating that they were produced in transfer reactions. Furthermore, the peaks at energies of about 5.12 MeV, 5.22 and 5.31 MeV were attributed to ^{208}Po, ^{206}Po and ^{210}Po, respectively. The ^{206,208,210}Po activities were present in the detector prior to this experiment because they were produced in the α-decay chains starting from ^{218,220,222}Th nuclei, respectively. The short-lived Th nuclei have been originally produced using a different reaction in a previous experiment for calibration purposes.

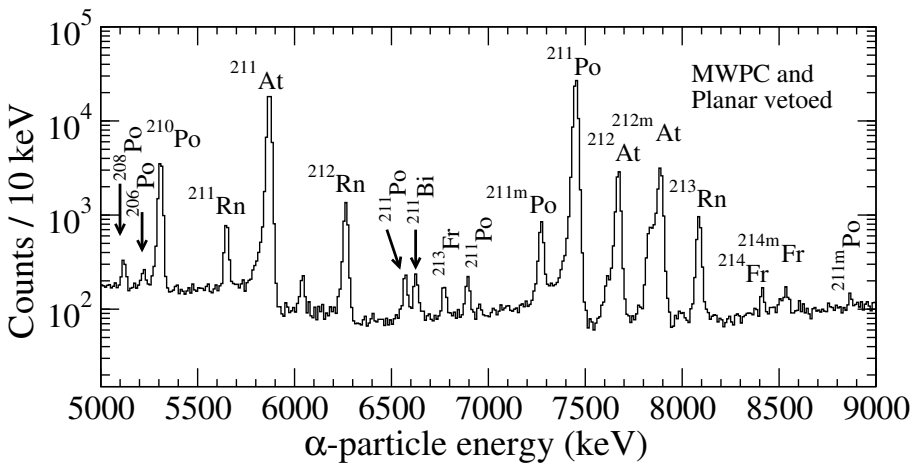

Figure 4.4. Energy spectrum of the α particles from the ^{34}S + ^{209}Bi reaction measured in the DSSDs and vetoed with the gas counter (MWPC) and the Planar detector.

4.2.3 ER-α correlations

Correlated events occurring in the same pixel of the DSSDs of the type ER-α were searched for in the data using various search times with the energy assumed to be in the range 5 MeV$\leq E_\alpha \leq$ 9 MeV. The correlations found with a maximum search time of 200 s is shown in Fig. 4.5 as the ER-α time difference on a logarithmic scale versus the α-particle energy. The short-lived component that is indicated with a dashed red line (Region 1) is from the decays of the transfer-reaction products that are still visible in this plot due to the low-energy tail of the TR recoils passing through the same gate conditions as the ERs. Based on the very short correlation times (<< 1 s) these events were excluded from further analysis and only the remaining part of the data (Region 2 in the figure) was inspected further.

A projection onto the horizontal axis of the two-dimensional ER-α correlation plot of Fig. 4.5 by only including Region 2 is shown in Fig. 4.6(a). Compared to the gas-vetoed α-particle energy spectrum of Fig. 4.4, an additional α activity at an energy of 7.57(3) MeV has emerged. When the search time is reduced to 30 s, the number of random correlations is greatly reduced and the corresponding α-particle energy spectrum shown in Fig. 4.6(b) is obtained. A few small α peaks have now appeared in the energy range 7.90-8.20 MeV, where the most prominent peaks are visible at energies of 8.09(3) MeV and 8.19(3) MeV.

The time distributions of the correlated ER-α(8.19 MeV) and ER-α(8.09 MeV) events were investigated in more detail and are shown in Fig 4.7(a) and (b), respectively. It can be seen from the time spectra that both of the fast α activities at the energies of 8.19(3) MeV (60 events) and 8.09(3) MeV (27 events) correspond to a radioactive decay with a similar half-life that was determined to be 6(2) s. The maximum search time has been expanded to 21600 s = 6 h to include the distributions arising from the random correlations that have contributions that cannot be neglected in the analysis of the fast 6-s activities. The locations of the maxima of the random correlations correspond to the average counting rate of the fusion-like ERs in the individual DSSD pixels during the experiment (3700 s; $2.7 \cdot 10^{-4}$ Hz/pixel). The half-lives and number of events of the fast α activities were extracted by using fits shown as the black dashed lines of a two-component density distribution function given by Eq. 3.17. The blue and red components correspond to the fast (real) and slow (random) activities obtained from the fits, respectively.

The time distribution of the ER-α(7.57(3) MeV) correlations were investigated in the same manner as in Fig. 4.7 and 42 events were estimated for the fast activity from the two-component fit made according to Eq. 3.17 to the time distribution. The initial assigments of the 7.57-MeV α activity to the decay of ^{240}Cf and the assignment of the 8.19-MeV and 8.09-MeV activities to the decay of the new isotope ^{240}Es were made based on the measured half-lives and α-particle energies with further support given by investigations of ER-α_1-α_2 correlations that are described in the next section.

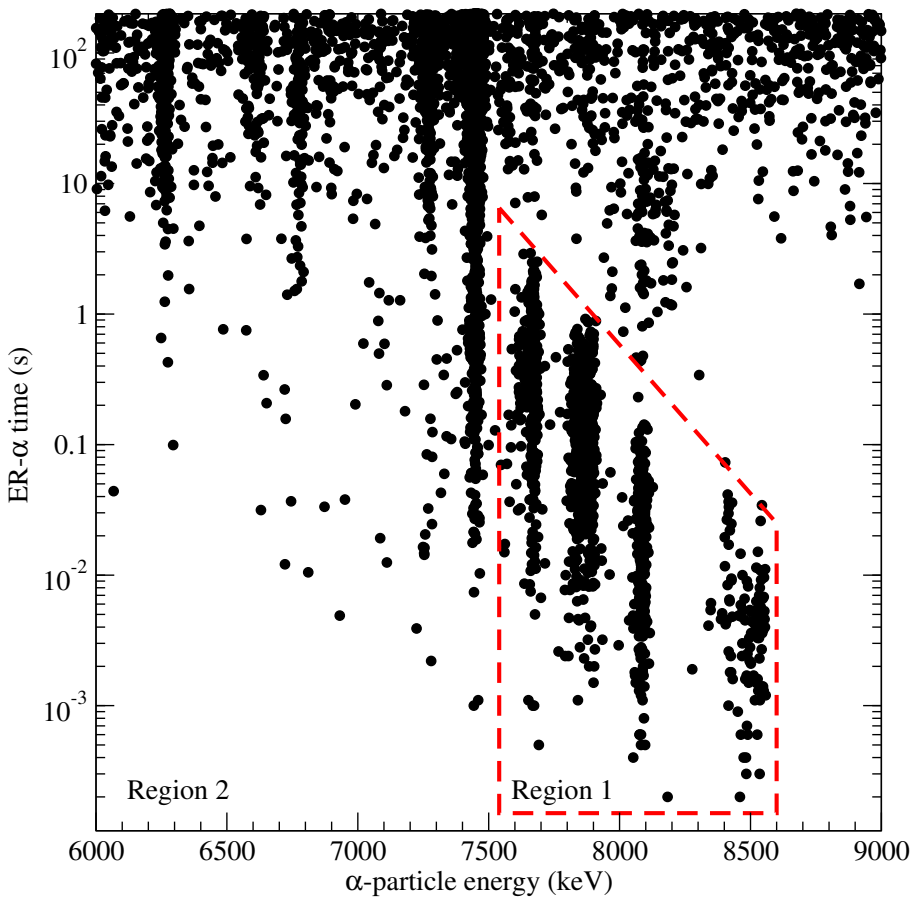

Figure 4.5. Two-dimensional plot of the correlated ER-α times on a logaritmic axis from the ^{34}S + ^{209}Bi reaction as a function of the α-particle energy measured in the DSSDs and vetoed with the gas counter (MWPC) and the Planar detector. The maximum search time for the ER-α pairs was 200 s. Region 1 that was assigned to decay events of transfer-reaction products is indicated with a dashed red line. See text for more details.

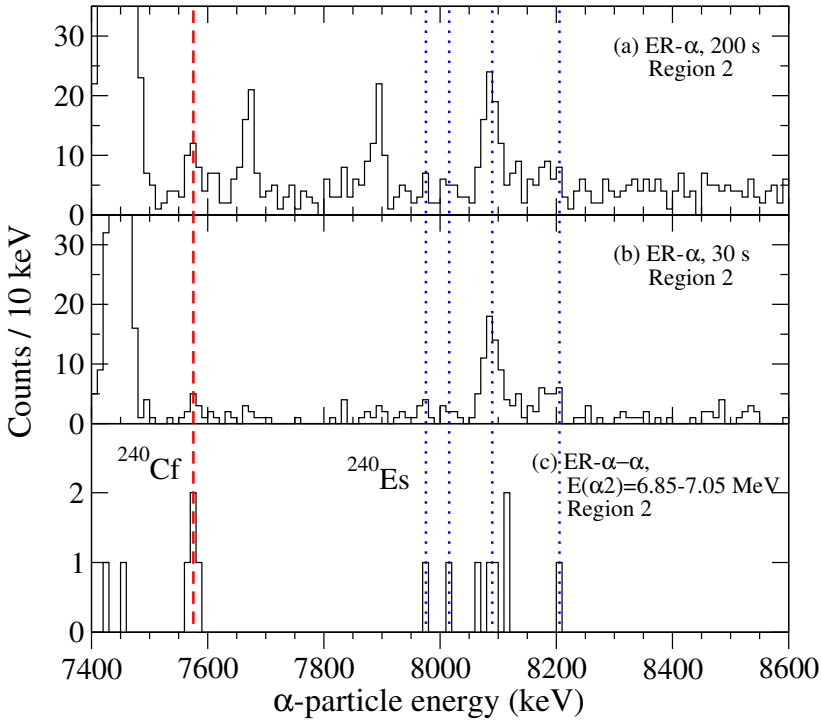

Figure 4.6. Energy spectra of the correlated α particles from the ^{34}S + ^{209}Bi reaction measured in the DSSDs and vetoed with the gas counter (MWPC) and the Planar detector; (a) α-particle events following a recoil implantation within 200 s; (b) α-particle events following a recoil implantation within 30 s; (c) as in (a) but followed by a second α decay event within 1200 s where the $E(\alpha_2)$ corresponds to the known α-particle energy of ^{236}Cm. The fast components that were identified as decays of transfer-reaction products as shown in Fig. 4.5 (Region 1) have been excluded from the spectra. The α-particle energies assigned to ^{240}Cf and ^{240}Es are marked by dashed red and dotted blue lines, respectively. See text for more details.

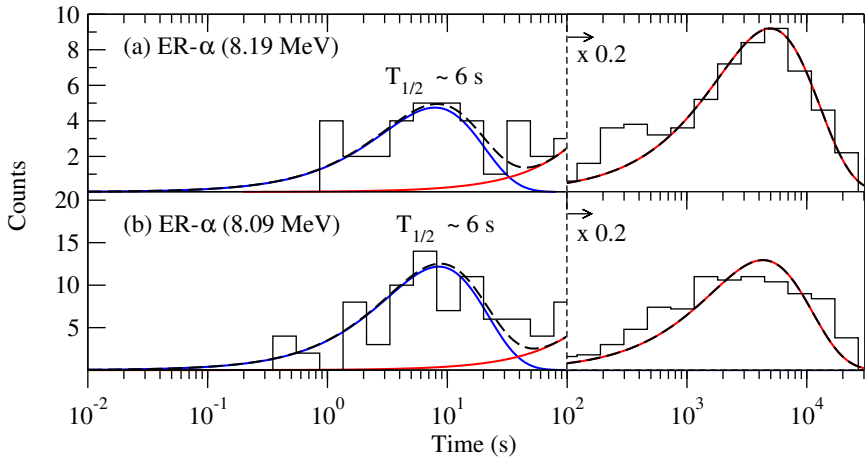

Figure 4.7. The time distributions of the correlated ER-α events where the measured α-particle energy was (a) 8.19(3) MeV and (b) 8.09(3) MeV. The dashed black line is the sum function of the two components where the blue (red) curve corresponds to the fast (slow, random) component of the fit. Note the change in the scale at 100 s. The maximum search time of the ER-α correlations was 6 h.

Prompt γ rays detected in the focal-plane germanium detectors in coincidence with the TR correlated α particles within a search time of 2 s is shown in Fig 4.8(a). The peak at an energy of 63 keV originates from the 4_1^+ to $5_{g.s.}^+$ transition in ^{208}Bi that is populated in the α decay of the transfer-reaction product ^{212m}At. The same 63-keV peak is also visible in panel (b) of Fig. 4.8 where the prompt γ rays in coincidence with the ER correlated α particles of Region 1 of Fig. 4.5 are shown because the low-energy tail of the TRs still pass through the gate conditions that were set for the ERs.

In Fig. 4.8(c) the γ rays (or X-rays) in prompt coincidence with the ER correlated 8.09-MeV α particles with a search time of 30 s (excluding Region 1 of Fig. 4.5) are shown. Six photon events at the energies of 125(3) keV (three events), 112(3) keV, 89(3) keV and 67(3) keV were detected with the 8.09-MeV α particles. Two of the energies are similar to the X-ray energies from Bk ($E(K_{\alpha 1})$ = 112 keV, $E(K_{\beta 1})$ = 127 keV and $E(K_{\beta 3})$ = 125 keV, [Firestone96]), however, the relative intensities are inconsistent with the assumption that the 125-keV events would be X-rays. In addition, no prompt γ rays were detected with the higher energy 8.19-MeV α particles. Therefore, the 125-keV events were tentatively assigned to be γ rays depopulating the excited states in ^{236}Bk after the α decay of ^{240}Es. The attribution of the 125-keV to the decay scheme is tentative due to the low statistics. An internal conversion coefficient for the 125-keV transition was estimated to be 4(3) by using an estimated absolute γ ray efficiency for the germanium detectors of 25(5)% that was based on simulations [Andreyev04]. It is possible that the 112-keV event is a X-ray from Bk and, as such, would support the assignment of the 8.09-MeV α particles to the α decay of ^{240}Es.

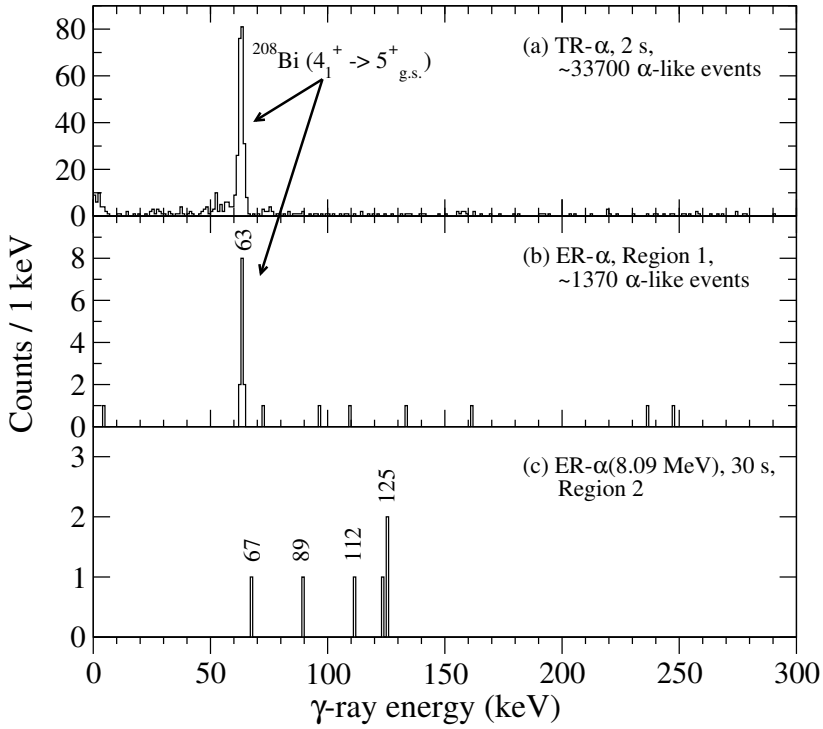

Figure 4.8. Energy spectra of the prompt γ rays measured in the focal-plane germanium detectors in coincidence with (a) the α particles following a TR implantation within 2 s; (b) the α particles following an ER implantation in Region 1 of Fig. 4.5; (c) the 8.09-MeV α particles following an ER implantation in Region 2 of Fig. 4.5 within 30 s as also shown in Fig. 4.6(b). The total number of TR/ER-correlated α-like events are indicated in (a) and (b).

4.2.4 ER-α-α correlations

Following the pairs of ER-α correlations, second α particles were searched for in the same pixel of the DSSDs. The maximum search times in the ER-α_1-α_2 events were $\Delta t_{\mathrm{ER}-\alpha_1} < 200$ s between the ER implantation and the first α_1 event and $\Delta t_{\alpha_1-\alpha_2} < 1200$ s between the α_1 and α_2 decay events. The correlated events that were found are shown in Fig. 4.9 as a two-dimensional α_1-α_2 correlation plot (α_2 energy against the α_1 energy). Most of of the events originate from random correlations due to the high number of α decays of the transfer-reaction products at the expected α-particle energies that have been marked with dashed red lines. Several of the mother α-particle events are followed by daughter α-particle energies that appear not to have a random origin in the range of 6.85-7.05 MeV that has been indicated by the green solid lines.

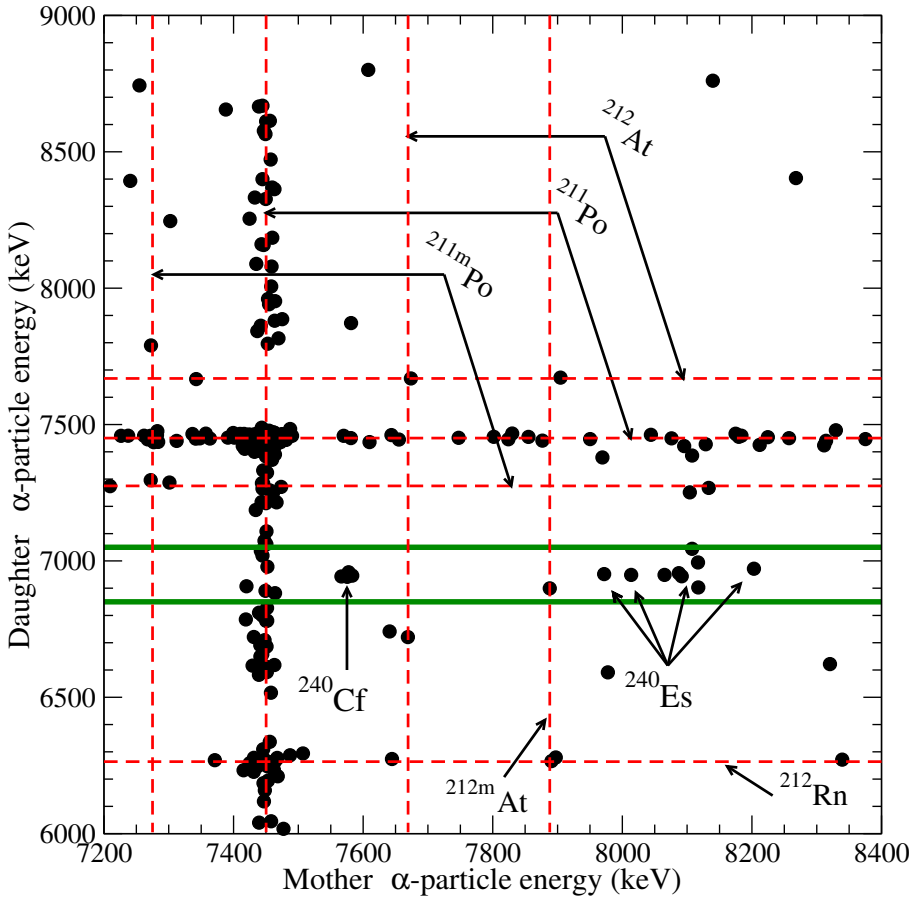

Figure 4.9. The mother (α_1) and daughter (α_2) particle energies of the correlated ER-α_1-α_2 events in the ^{34}S + ^{209}Bi reaction. The maximum search times were 200 s for the first pair (ER-α_1) and 1200 s = 1 h for the second pair (α_1-α_2). The expected random correlations arising from the α decays of the transfer-reaction products are indicated with dashed red lines. The $E_{\alpha 2}$ range between the green lines corresponds to the known α-particle energy of ^{236}Cm. See text for more details.

A projection of Fig. 4.9 is shown in Fig. 4.6(c). where the energy spectrum of the mother α events is displayed for those events where the daughter α-particle energy is in the range of 6.85-7.05 MeV. Based on the good agreement of the measured α-particle energies and the average lifetime $\Delta t_{\alpha_1-\alpha_2} \approx 430$ s with the literature values, the chains were attributed to populate ^{236}Cm that decays further by α decay (E_α = 6.954(20) MeV, $T_{1/2}$ = 410(50) and b_α = 18(2)% [Khuyagbaatar10]).

Four of the correlated ER-α_1(7.57 MeV)-α_2(^{236}Cm) events shown in Fig. 4.9 and Fig. 4.6(c) were attributed to the α decay of ^{240}Cf in the α-decay chain α_1(^{240}Cf)-α_2(^{236}Cm). The cross section of the direct production of ^{240}Cf as an ER in the p2n exit channel of the ^{34}S+^{209}Bi fusion reaction was estimated to be at least an order of magnitude smaller than the 3n channel according to calculations made with the HIVAP code [Reisdorf81]. Consequently, the contribution of directly produced ^{240}Cf was estimated to yield less than one event of the type ER-α_1(7.57 MeV)-α_2(^{236}Cm). Thus, within statistical uncertainties, most of the correlated α decay events of ^{240}Cf are likely to originate from the EC decay of the new isotope ^{240}Es.

Five more chains of the type ER-α_1-α_2(^{236}Cm) were observed where four had $E_{\alpha 1}$ = 8.09 MeV and one chain had $E_{\alpha 1}$ = 8.19 MeV. These five chains were attributed to the α decay of ^{240}Es. After α decay to the daughter ^{236}Bk, it decays further by EC decay to ^{236}Cm that finally decays by α decay. The fact that such genetic decay chains leading to known α decay of ^{236}Cm are observed at these two previously unassigned α energies strongly supports the assignment of these two α activities found also in ER-α correlations of Fig. 4.6(b) to the α decay of ^{240}Es. In addition, two decay chains that appear to be of non-random origin were observed where energy of the first α particle corresponded to about $E_{\alpha 1}$ = 8.02 MeV and $E_{\alpha 1}$ = 7.97 MeV. These two α energies show up as weak peaks that were observed in the ER-α correlations at the α energies of 8.02(3) MeV and 7.97(3) MeV in Fig. 4.6(b) and have half-lives of about 5.2 s and 4.4 s, respectively. Based on the observed ER-α_1-α_2(^{236}Cm) correlations and the similar half-lives, also these two groups of α particles were tentatively assigned to the α decay of ^{240}Es. No α decays of ^{236}Bk were detected following the ER correlated α decays associated to ^{240}Es.

Finally, following the ER correlated 8.19-MeV and 8.09-MeV α particles corresponding to ^{240}Es, two correlated α-decay chains of α(^{232}Pu)-α(^{228}U)-α(^{224}Th)-α(^{220}Ra)-α(^{216}Rn)-α(^{212}Po) were observed with similar α particle energies and reasonable lifetimes in the careful event-by-event analysis. The low number of the observed long chains was expected, since ^{232}Pu (α-decay daughter of ^{236}Cm) has an α-decay branch of only about 20% (see *e.g.* [Laue00] and references therein). Some of the α decays in the long chains were missed because of the possibility for the α particle to escape the detector or to be marked as piled-up events due to the very short half-lives of ^{216}Rn, ^{212m}Po or ^{212}Po.

4.2.5 ER-fission and ER-α-fission correlations

Fission-like events were searched for in correlated events of the types ER-fission and ER-α-fission. The fission-like events following ER implantation signals were required to have a high energy deposited in the Y-side of the DSSDs ($E > 50$ MeV) and in anticoincidence with MWPC signals. The time distributions of the correlated ER-fission events is shown in Fig: 4.10(a). Similar to the ER-α times in Fig. 4.7(a) and (b), two separate components were observed in the distributions. The long-lived component that was fitted with a one-component density distribution function from Eq. 3.17 shown with a red line was attributed to random correlations.

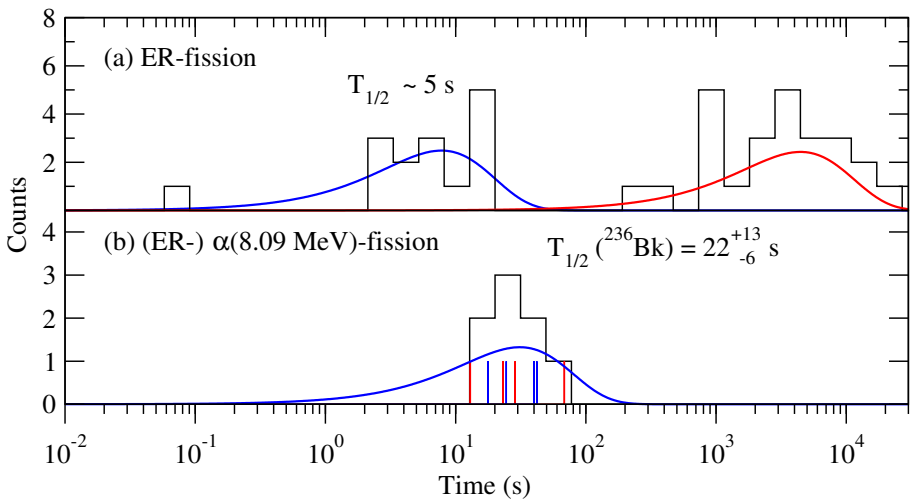

Figure 4.10. The time distributions of (a) the ER correlated fission-like events without α-like or escaped α-like signals between the ER and the fission; (b) the fission-like events following an ER correlated α particle with an energy of 8.09(3) MeV or an escaped α-particle event. In panel (a) and (b) the blue curve corresponds to the fast (real) components that were plotted with the time distribution functions using the calculated half-lives obtained from the maximum-likelihood method and the number of events. In (a) the slow (random) component was fitted with a one-component time distribution function showing negligible contribution to the fast (real) activity. Additionally, in (b) the events where full-energy (escape) α decays were seen are marked with blue (red) lines. See text for details.

The fifteen fission-like events shown in 4.10(a) were assigned to belong to the decay of ^{240}Es based on their half-life. The half-life of the events was calculated using the maximum-likelihood method to be 5(2) s that is within error bars and similar to the half-life observed for its α decay. It is well known that unpaired nucleons cause extra hindrance against fission of many orders of magnitude [Hoffman89, Heßberger17].

Therefore, these fission-like events are very unlikely to originate directly from the ground state of the odd-odd nucleus ^{240}Es. Additionally, they cannot originate from the ground state of ^{240}Cf that has a spontaneous-fission branch of only $b_{\mathrm{SF}}(^{240}\mathrm{Cf})$= 1.5(2)% [Khuyagbaatar10] due to the large number of observed fission events compared to the total number of events that was deduced from the ER-α correlations. Moreover, the observed half-life of the fission activity is much shorter than that of ^{240}Cf. Consequently, these fission-like events were attributed to occur directly from the excited states of ^{240}Cf that are populated in the EC decay of ^{240}Es. Thereby, they were assigned to the ECDF branch of ^{240}Es.

Finally, four event chains of the type ER-α-fission were observed where all of the ER-α events were correlated with 8.09-MeV α events assigned to the α decay of ^{240}Es. No other ER-α-fission events were observed with a search time of the first pair in the chain of $\Delta t_{\mathrm{ER}-\alpha} \leq 200$ s. In addition, four more chains were identified in event-by-event analysis of the fission-like events as being ER-α(escape)-fission events, where the α particles escaped in the backward direction from the DSSD detector depositing only part of their energy. In three of the escaped α events, a coincident energy deposit was registered in one of the PIN detectors that are surrounding the DSSDs in the backward direction in a box configuration. The time distribution of these fission-like events relative to the second decay member (α or α(escape)) is shown in Fig. 4.10(b). Based on the similar time distributions of the eight events and the α-particle detection efficiency of the DSSDs and the PIN detectors, these eight event chains were attributed to originate from a single activity. The half-life calculated using the maximum-likelihood method for the eight events was $T_{1/2} = 22^{+13}_{-6}$ s. By taking into account only the four events where the full energy of the α particles was measured, a half-life estimate of $T_{1/2} = 22^{+22}_{-8}$ s was obtained. Because only α decays of the known ^{236}Cm was detected following the correlated α decay events of ^{240}Es, a high EC-decay branch is indicated in ^{236}Bk. Thus, all of these eight correlated fission-like events were attributed to the ECDF branch of ^{236}Bk.

The exact full energy of the fission-like events could not be extracted reliably due to the limited energy range in the DSSDs, the pulse-height defect and calibration that was extrapolated from the α calibration. Therefore, most of the energies of the fission events were saturated. Further support of the classification of the high-energy events as fission events was found by searching for coincidences with γ rays detected at the focal plane. Fission is typically followed by the emission of multiple γ rays from the de-exciting daughter nuclei. It should be noted that γ rays were detected in coincidence with most of the fission-like events in the fast components of Fig. 4.10(a), whereas, most of the fission-like events in the random component do not have any γ rays in coincidence. Furthermore, at least one γ ray was detected in coincidence with all of the eight fission-like events shown in Fig. 4.10(b).

4.3 Discussion

Combining all of the information obtained from the ER-α, ER-α-α, ER-fission and ER-α-fission correlations allowed decay schemes for the new isotopes ^{240}Es and ^{236}Bk to be constructed. In addition, the measured correlated fission-like events showed that there is an ECDF branch present in both of the new isotopes. The experimental probabilities of the ECDF were determined for ^{240}Es and ^{236}Bk and are compared to the systematic behaviour of Es, Bk and Am isotopes.

4.3.1 Decay schemes

The proposed decay schemes for the new isotopes ^{240}Es and ^{236}Bk is shown in Fig. 4.11. The branching ratios of $b_\alpha = 70(10)\%$ and $b_{\mathrm{EC}} = 30(10)\%$ for ^{240}Es were determined based on the total number of produced ^{240}Es and ^{236}Bk nuclei obtained from the ER-α correlations using all four α groups assigned to ^{240}Es, taking into account the EC and ECDF branches, and corrected with the full-energy α detection efficiency of the DSSDs of $\epsilon_\alpha = 55\%$. The total number of events could also be extracted from the ER-α-α correlations and agree within error bars with the values presented here, however, the statistical uncertainties are much larger. The $P_{\mathrm{ECDF}} = 16(6)\%$ of ^{240}Es was estimated from the ER-fission events together with the ER-α_1(^{240}Cf correlations to estimate the EC-decay branch in ^{240}Es.

Using the highest energy (8.19(3) MeV) α particles attributed to the α decay of ^{240}Es of , an α-decay Q value of 8.33(3) MeV was calculated. The measured half-life of 6(2) s was determined from the ER-α correlations of the two most intense α activities of 8.09(3) MeV and 8.19(3) MeV of ^{240}Es. The half-life estimated from the ER-fission correlations to be 5(2) s with less statistics is well within the error bars. The measured half-life is close to the theoretically calculated estimate of ≈ 7 s given in [Möller97]. However, the predicted decay branches [Möller97] of $b_\alpha = 13\%$ and $b_\beta = 87\%$ are not consistent with the measured values. The measurement indicates that the decay proceeds faster and mostly via α decay. The maximum α-particle energy of 8.03 MeV calculated from the predicted Q value of 8.17 MeV from [Möller97] is close to the measured value, given that the theoretical (extrapolated) masses typically have systematical uncertainties of the order of hundreds of keV. From the relative intensities of the α particles it seems that the α decay to an excited state with the 8.09-MeV α (about 60% of the α decay intensity) particles is favoured and corresponds to a decay between states of similar structure. The 8.19-MeV α particles decay to a lower state in ^{236}Bk that could be the ground state. However, it is also possible that most of the intensity decays with the 8.09-MeV α particle emission and the 8.19-MeV peak is formed due to summing effects in the DSSD with internal conversion electrons. This interpretation is further supported by the observed increased width of the 8.19-MeV α peak relative to the 8.09-MeV α peak.

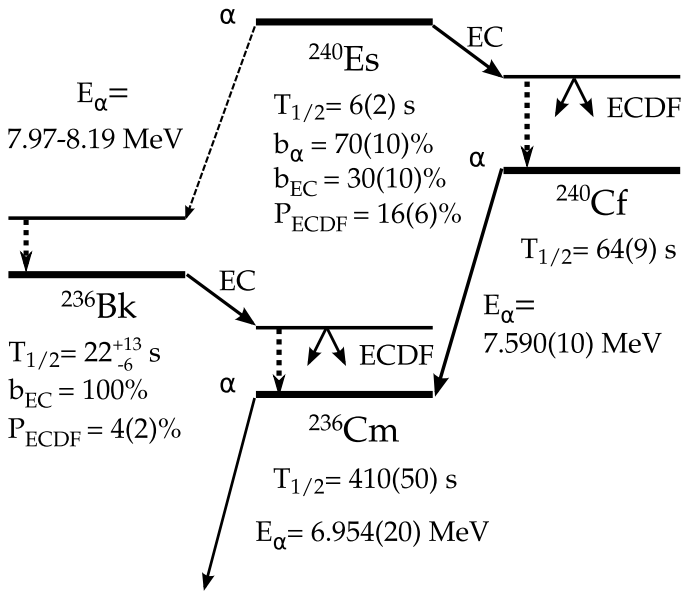

Figure 4.11. The proposed decay scheme for the new isotopes ^{240}Es and ^{236}Bk. The indicated measured values for ^{240}Es and ^{236}Bk are from this work, ^{240}Cf from [Silva70] and ^{236}Cm from [Khuyagbaatar10]. See text for more details.

The hitherto unknown isotope ^{236}Bk was populated in the α decay of ^{240}Es. As shown in Fig 4.11, only the EC branch in ^{236}Bk could be observed via its ECDF branch. The measured half-life $T_{1/2} = 22^{+13}_{-6}$ s has a high uncertainty as it is based on only eight correlated ER-α-fission events. The $P_{\mathrm{ECDF}} = 4(2)\%$ of ^{236}Bk was estimated from the ER-α-fission events together with the ER-α_1(^{240}Es)-α_2(^{236}Cm) correlations to estimate its EC-decay branch and assuming that b_{EC}(^{236}Bk) = 100%. Decay branches of $b_\alpha = 18\%$, $b_\beta = 82\%$ and α-particle energy of about 7.63 MeV have been predicted for ^{236}Bk in [Möller97] with a half-life of about 42 s. The calculated decay branches of ^{236}Bk are more in agreement with the experimental results than in the case of ^{240}Es. It is possible that the α-decay branch of ^{236}Bk was too small to be observed in this experiment or the α-particle energies may overlap with the α decays of the transfer-reaction product ^{211}Po.

Due to the lack of statistics and the typically complicated level structures of the odd-odd nuclei, the present data did not allow precise assignments of the properties of the states such as the spins and parities in ^{240}Es or ^{236}Bk. However, some tentative predictions and assignments can be suggested based on theoretical calculations and systematics that are available in the region. The active orbitals near the Fermi surface in this region are the $\pi\frac{7}{2}^+$[633] (from $i_{13/2}$) and $\pi\frac{3}{2}^-$[521] (from $f_{7/2}$) for the protons and $\nu\frac{5}{2}^+$[633] (from $g_{9/2}$) and $\nu\frac{5}{2}^-$[752] (from $j_{15/2}$) for the neutrons. Based on the lighter N=141 isotones, heavier Es isotopes and theoretical calculations [Parkhomenko04, Zhang12]

the ground-state proton and neutron configurations of ^{240}Es could be $\pi\frac{7}{2}^{+}[633]$ and $\nu\frac{5}{2}^{+}[633]$, respectively. Possible alternatives are $\pi\frac{3}{2}^{-}[521]$ for the proton and $\nu\frac{5}{2}^{-}[752]$ for the neutron. In turn, the likely active Nilsson orbitals for ^{236}Bk are $\pi\frac{3}{2}^{-}[521]$ for the protons and $\nu\frac{5}{2}^{-}[752]$ for the neutrons, based on the heavier Bk isotopes and the lighter $N = 139$ isotones. Possible alternatives for ^{236}Bk could be $\pi\frac{7}{2}^{+}[633]$ and $\nu\frac{5}{2}^{+}[633]$.

All of the possible configurations from the aforementioned orbitals for the ground-state spins and parities are given in Table 4.2. The possible combined total angular momenta are given and the state expected to have the lowest energy is underlined in each case was estimated by using the Gallagher-Moszkowski rules [Gallagher58] for the coupling of the angular momenta in an odd-odd nucleus. From these combinations the ground state of ^{240}Es can be expected to be 1^{+} from the $\pi\frac{7}{2}^{+}[633] \otimes \nu\frac{5}{2}^{+}[633]$ coupling or 1^{-} from the $\pi\frac{3}{2}^{-}[521] \otimes \nu\frac{5}{2}^{+}[633]$ being a possible alternative. The ground state of ^{236}Bk can be expected to be 4^{+} from the $\pi\frac{3}{2}^{-}[521] \otimes \nu\frac{5}{2}^{-}[752]$ coupling. Alternatively, a ground-state spin and parity of 6^{-} could be possible from the $\pi\frac{7}{2}^{+}[633] \otimes \nu\frac{5}{2}^{-}[752]$ configuration. The assignments here are purely tentative due to the low statistics and the lack of precise experimental data about the spins and parities of the ground states in this region.

Table 4.2. Possible ground-state Nilsson orbital configurations for the protons and neutrons in ^{240}Es and ^{236}Bk and the resulting total angular momenta I^{π} after the coupling. In each case, the spin and parity that is expected to lie lowest in energy using the Gallagher-Moszkowski rules [Gallagher58] is underlined.

Configuration	$I = \lvert\Omega_{\pi} - \Omega_{\nu}\rvert$	$I = \Omega_{\pi} + \Omega_{\nu}$	Nucleus
$\pi\frac{7}{2}^{+}[633] \otimes \nu\frac{5}{2}^{+}[633]$	$\underline{1^{+}}$	6^{+}	^{240}Es, ^{236}Bk
$\pi\frac{7}{2}^{+}[633] \otimes \nu\frac{5}{2}^{-}[752]$	1^{-}	$\underline{6^{-}}$	^{236}Bk, ^{240}Es
$\pi\frac{3}{2}^{-}[521] \otimes \nu\frac{5}{2}^{-}[752]$	1^{+}	$\underline{4^{+}}$	^{236}Bk, ^{240}Es
$\pi\frac{3}{2}^{-}[521] \otimes \nu\frac{5}{2}^{+}[633]$	$\underline{1^{-}}$	4^{-}	^{240}Es, ^{236}Bk

The internal conversion coefficients obtained using the BrIcc calculator [Kibédi08] for a 125(3)-keV transition in a Bk (Z=97) nucleus are 4.0(3) and 7.3(9) for transitions of M1 and E2 character, respectively. A measured value of 4(3) was determined from the number of prompt 125-keV events that were observed with the 8.09(3) MeV α particles, under the assumption that the events are γ rays. The measured value is closer to the calculated value for a transition with M1 character that would be expected between two states of the same parity and with a spin difference of unity. Such a structure of the excited states would be expected in ^{236}Bk at low excitation energies from all of the tentative configuration assignments given in Table 4.2. However, the uncertainty in the determined internal conversion coefficient is very large and partly overlaps with the calculated estimate for an E2 transition. Furthermore, an energy difference of 102(3) keV was calculated from the Q values using the two higher α particle energies

of 8.19(3) MeV and 8.09(3) MeV, which is within error bars but not exactly consistent with the γ-ray energy of 125(3) keV. Due to the very low statistics the 125-keV γ ray could be placed in the level scheme only tentatively.

4.3.2 Electron-capture delayed fission probabilities

Often in the earlier studies of ECDF, the measured ECDF probabilities (P_{ECDF}) have been presented as a function of Q_{EC}, which results in an exponential dependence as expected in quantum mechanical tunneling. However, a more elaborate way is to present the P_{ECDF} by also taking into account the fission barrier in the daughter nucleus. In this way it is possible to extract information on the fission barriers in nuclei [Veselský12]. A simple mathematical concept and a variable that describes the structure of a fission barrier is the height of the fission barrier (B_{sf}) used to calculate probabilities of spontaneous fission in nuclei. The dependence of the P_{ECDF} on the quite simple difference $Q_{\mathrm{EC}} - B_{\mathrm{sf}}$ was already introduced earlier (see *e.g.* [Hall90b, Möller09] and the references therein). However, this dependence is still not well understood. Starting from simple empirical descriptions, the exponential dependence of the P_{ECDF} on $Q_{\mathrm{EC}} - B_{\mathrm{sf}}$ has been shown [Hall90b, Ghys15] to follow from approximations on the fission decay width that depends heavily on the energy available in the EC decay (Q_{EC}) and the structure of the fission barrier.

The previously measured ECDF probabilities (closed symbols) in Es (black), Bk (blue) and Am (red) isotopes together with the values obtained in this work (open symbols) are shown in Fig. 4.12 as a function of the difference in the theoretical Q_{EC} value [Möller97] of the mother nucleus and the theoretical fission barrier height B_{sf} [Möller15] in the daughter nucleus of the EC decay. The finite-range droplet model (FDRM) and the finite-range liquid drop model (FRLDM) were used in the calculations of Q_{EC} and B_{sf}, respectively. According to the previous experimental studies in a chain of four neutron-deficient odd-odd einsteinium isotopes of ^{242}Es [Shaughnessy00], ^{244}Es [Shaughnessy02] and ^{246,248}Es [Shaughnessy01], a relatively high P_{ECDF} was predicted for the next lighter isotope ^{240}Es as indicated by the exponential fit of the P_{ECDF} as a function of $Q_{\mathrm{EC}} - B_{\mathrm{sf}}$ that is shown with a black dashed line. The data on the odd-odd Es isotopes represents the longest chain of isotopes of one element where the P_{ECDF} have been measured.

Similar behavior as in the Es isotopes was predicted for the Bk isotopes from the data that is available for ^{240}Bk [Galeriu83] and ^{238}Bk [Kreek94] as shown by the blue dashed line in Fig. 4.12. The measured values for ^{240}Es and ^{236}Bk follow the exponentially increasing trend and no deviations from this behaviour can be observed.

The measured values of the P_{ECDF} in a chain of three odd-odd Am isotopes of ^{234}Am [Hall90b], ^{232}Am ([Andreyev13] and references therein) and a recently reported value for ^{230}Am [Wilson17] have been included in Fig. 4.12. The lower limit of the $P_{\mathrm{ECDF}} > 30\%$ in ^{230}Am is the highest ECDF branch measured so far in all

nuclei. Note that three separate values of P_{ECDF} are given for ^{232}Am that are not consistent with each other within uncertainties as discussed in [Wilson17]. Several lines on the logarithmic scale as in the case of Es and Bk isotopes could be fitted depending on what data point is used for ^{232}Am. The most recent and the lowest value of $6.9(10) \cdot 10^{-4}$ [Hall90a] is considered to be the most accurate. A line drawn through the two values for ^{234,232}Am would nicely follow a similar dependence (slope) as seen in Es and Bk isotopes but would greatly underestimate the P_{ECDF} measured in ^{230}Am.

Several interesting features can be identified from the measured values of P_{ECDF} presented in Fig. 4.12. For instance, by following the dashed lines and extrapolating to the next lighter isotopes of ^{238,236}Es, ^{234,232,230}Bk and ^{228}Am, one could expect that the probability for the fission in the EC-decay branch saturates, *i.e.* $P_{\mathrm{ECDF}} \rightarrow 1$. This means that the fission will dominate over other mechanisms of de-excitation of the excited states in the nucleus. In such cases the role of the fission barrier may be negligible. The expected locations of the $Q_{\mathrm{EC}} - B_{\mathrm{sf}}$ values calculated in these isotopes have been indicated by the arrows on the upper x-axis. It should be noted that the discovery of the α-decaying isotope ^{234}Bk was recently reported in [Kaji16] where the evaluation of the P_{ECDF} was unfortunately not possible despite the large number of fission events that were observed. However, from the reported α-decay chains it can be deduced that the P_{ECDF} is not yet saturated in ^{234}Bk.

Another outstanding feature in Fig. 4.12 is the relative difference of the P_{ECDF} probabilities between the isotopic chains of Es, Bk and Am. This implies that the simple macroscopic variable $Q_{\mathrm{EC}} - B_{\mathrm{sf}}$ may not fully describe the process. One important factor that is not included in the variable is the actual shape of the fission barrier. For example, "two-humped" or "multi-humped" fission barriers exist especially in heavy-nuclei [Möller15] that strongly affect the tunneling through these total barriers. Thus, the shape and width of the fission barrier can have a large impact on the value of P_{ECDF}. On the other hand, the measured P_{ECDF} as a function of the variable $Q_{\mathrm{EC}} - B_{\mathrm{sf}}$ could in turn provide information also about the shape of the total fission barrier [Andreyev13]. The relative decrease in the P_{ECDF} when moving from Es to Bk and further to Am isotopes could be associated with the widening of the total fission barriers when going from Cf to Cm and further to Pu, respectively.

Finally, it can be seen from Fig. 4.12 that the increase in the P_{ECDF} of ^{230}Am is rapid when compared to the heavier Am isotopes ^{232,234}Am as well as to the slopes of the lines (on a logarithmic scale) that are shown for Es and Bk isotopes. This effect could be due to the population of the excited states well above the barrier that could break the simple dependence of P_{ECDF} on the variable $Q_{\mathrm{EC}} - B_{\mathrm{sf}}$. In the semi-empirical descriptions it was assumed that only states close to the barrier height can be populated in the EC decay [Hall90b, Ghys15]. Above the fission barrier the influence of the beta-decay strength function (S_{β}) may play a stronger role in this process [Wilson17]. In ^{230}Am the difference $Q_{\mathrm{EC}} - B_{\mathrm{sf}} = 2.61$ MeV is the highest among the data points that are shown in Fig. 4.12 meaning that excited states well above the fission barrier height in ^{230}Pu can be populated.

It should also be noted that other mass models and estimates of the fission barrier heights can be used and the resulting dependence of the P_{ECDF} on the variable $Q_{\mathrm{EC}} - B_{\mathrm{sf}}$ may change. These differences between various different fission models have been recently investigated in [Ghys15].

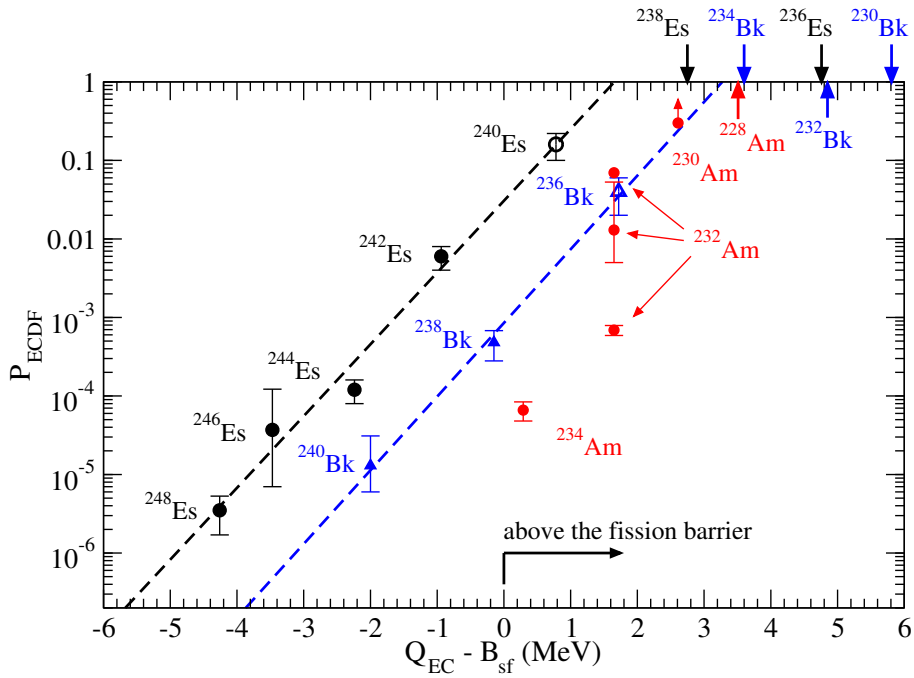

Figure 4.12. The electron-capture delayed fission (ECDF) probability (P_{ECDF}) as a function of the difference $Q_{\mathrm{EC}} - B_{\mathrm{f}}$ in the neutron-deficient Es (black), Bk (blue) and Am (red) isotopes. The data points for ^{240}Es and ^{236}Bk (open symbols) are from this work , the other measured P_{ECDF} (closed symbols) are from [Andreyev13, Wilson17] and references therein. The $Q_{\mathrm{EC}} - B_{\mathrm{f}}$ values of ^{238,236}Es, ^{234,232,230}Bk and ^{228}Am are marked with arrows where P_{ECDF} have not been measured and are expected to saturate ($P_{\mathrm{ECDF}} \rightarrow 1$). The calculated values of Q_{EC} (parent) and B_{sf} (daughter) are from [Möller97, Möller15], using the finite-range droplet model (FRDM) and the finite-range liquid drop model (FRLDM), respectively. Note that for the $P_{\beta\mathrm{DF}}$ of ^{232}Am three separate values are presented. See text for more details.

4.4 Future prospects

A large amount of information on the decay properties of the new isotopes ^{240}Es and ^{236}Bk were extracted in this work from the experimental data that was obtained from the fusion-evaporation reaction with a relatively small cross section and containing low statistics. The identification of the isotopes was made challenging by the random contributions from the transfer-reaction products. However, more statistics would be needed to understand the complicated structure of these odd-odd isotopes in more detail. A new and dedicated decay spectroscopy experiment would be needed in order to improve on the uncertainties in the α-particle energies, the decay branches and the values of P_{ECDF}. In addition, sparse information is available on the nuclei in this region of the nuclear chart that could be investigated in future experiments using different fusion-evaporation reactions.

Further experimental data on the P_{ECDF} and its dependence on $Q_{\mathrm{EC}} - B_{\mathrm{sf}}$ in the more neutron-deficient isotopes of Es, Bk and Am would provide more information on the very complicated ECDF decay process. In particular, the inconsistency of the measured values of P_{ECDF} in ^{232}Am would require a new measurement. Furthermore, a new measurement of the P_{ECDF} in ^{234}Am would give more confidence for predicting the slope of the dependence of P_{ECDF} on $Q_{\mathrm{EC}} - B_{\mathrm{sf}}$ in the Am isotopes.

An interesting open question remains whether the P_{ECDF} values presented in Fig. 4.12 become saturated already in the next lighter isotopes in the chains. However, experimental studies will become more challenging when approaching the proton dripline because the cross sections via fusion-evaporation reactions decrease quickly. Furthermore, the β-decay branches will decrease compared to the α-decay branches, the spontaneous fission branches of the ground states in the mother nucleus may start to compete with β^+/EC decay and the spontaneous fission may become dominant in the even-even daughter nuclei that may have very short half-lives. Finally, estimating the β^+/EC-decay branches in the EC-decay daughter nuclei may impose their own challenges.

Chapter 5

In-beam spectroscopy of ^{244}Cf

In this chapter the details of the experiment, data analysis, results and discussion related to the in-beam spectroscopic study of the neutron-deficient californium nucleus ^{244}Cf are presented. The main aim of the experiment was to study the excited states and the identification of the ground-state rotational band in ^{244}Cf and to examine its decay properties. Additionally, an attempt to measure the excited states and to study the decay properties of the odd-A nucleus ^{243}Cf was made in the same experiment. The experimental results from this work are compared to the systematic behaviour of the even-even N=146 isotones as well as to available theoretical calculations that have been performed for nuclei in the region.

5.1 Experimental details

The experiment was carried out in November, 2015 at the Accelerator Laboratory of the Department of Physics, University of Jyväskylä, Finland. The isotopes ^{244}Cf and ^{243}Cf were produced as evaporation residues (ER) of the ^{246}Cf* compound nucleus that was formed in the fusion reaction ^{48}Ca+^{198}Pt. The ^{48}Ca^{10+} ion beam was produced in an ECR ion source and accelerated by the K=130 MeV cyclotron. The self-supporting ^{198}Pt targets were enriched to 95% and had thicknesses of 644 μg/cm^2 and 858 μg/cm^2. The total time of the irradiation was about 220 h. Typical beam intensity during the experiment ranged from 20 to 40 pnA. A carbon foil with a thickness of 40 μg/cm^2 was used as a "charge reset" foil on the downstream side of the target. The RITU gas-filled recoil separator was coupled to the JUROGAMII germanium array at the target position to measure the prompt γ rays and the GREAT spectrometer system was used at the focal plane.

The fusion-evaporation reactions ^{198}Pt(^{48}Ca,2n)^{244}Cf and ^{198}Pt(^{48}Ca,3n)^{243}Cf were used in this study to produce the ^{244}Cf and ^{243}Cf isotopes of interest, respectively. The excitation functions of the 2n and 3n channels in the reactions were determined by measuring the production rate at different beam energies at the beginning of the experiment.

5.1.1 Calibration

The horizontal (Y) strips on the back (downtream) side of the DSSDs were used with low gain in order to measure the recoil and α-particle kinetic energies. In contrast, the vertical (X) strips were used with higher gain in order to be sensitive to measure low-energy internal conversion electrons. The X strips of the DSSDs were calibrated using an external ^{133}Ba electron source. The Y strips of the DSSDs were calibrated with an external mixed three-line α source. The daughter nucleus in α-decay deposits only part of its recoil energy in the DSSDs due to pulse-height defect. Therefore, the α-particle energies measured in the DSSDs were corrected for by subtracting 70 keV from the measured α-particle energies to match to the known energies of the most intense α decays that originated from ^{240,242}Cm. The energy resolution of the DSSDs was determined from the sum spectrum of all of the Y strips to be about 25 keV at 7.05 MeV. The PIN silicon detectors were also used with low gain to detect escaping α particles from the DSSDs and calibrated with an external mixed three-line α source.

The detectors in the JUROGAMII germanium array were calibrated for their energy and relative efficiency using ^{152}Eu and ^{133}Ba sources that were placed at the target position. The Planar detector was calibrated using the γ rays from an open ^{133}Ba source placed inside the vacuum chamber upstream from the DSSDs. The two Clover detectors placed at the sides of the focal-plane vacuum chamber and the large-volume GREAT Clover on the top of the chamber were energy calibrated using ^{152}Eu and ^{133}Ba sources placed outside the vacuum chamber.

5.2 Results

The analysis of the experimental data was performed using the GRAIN software package. The software trigger conditions for creating the events was set on any of the individual DSSD strips with an event length of 5 µs offset by a −2.5 µs delay. The triggering of another event within 2.5 µs time window was prevented by using an artificial deadtime condition on the software trigger. The time structure of the event definition is illustrated in Fig. 5.1.

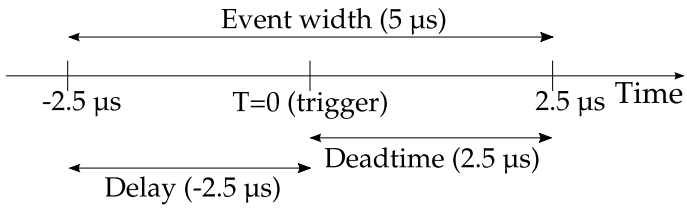

Figure 5.1. Definitions of the event structure that was used in the data analysis in the GRAIN software.

5.2.1 Recoil identification

The fusion-evaporation products (hereafter: ER, recoil) from the ^{48}Ca + ^{198}Pt reaction were distinguished from other reaction products by using the time-of-flight information (ToF) between the MWPC and the DSSD, the energy loss in the MWPC (ΔE) and the final energy deposit in the DSSD (E). Matrices of the ToF versus E and ΔE versus the ToF are shown in Fig. 5.2(a) and (b), respectively. The approximate locations of the two-dimensional gate conditions that were placed for the recoils are indicated by the red areas. The remaining recoils that did not pass these conditions were discarded from further correlation analysis. The locations of the final recoil gates that were used in the analysis were found by searching for the subsequent α decays in the same DSSD pixel corresponding to the α energies of ^{244,243}Cf.

5.2.2 α-particle energy spectrum

The measured energy spectrum of the α particles measured in DSSDs from the ^{48}Ca + ^{198}Pt reaction vetoed with the gas counter (MWPC) and the Planar detector is shown in Fig. 5.3. A contaminant peak at an α-particle energy of about 6.11 MeV was attributed to ^{242}Cm (E_α = 6.110(3) MeV [Asaro52]) originating from the long α-decay chain that starts from ^{254}No that was studied in a preceding experiment. The peaks at energies of about 5.12 MeV and 5.31 MeV were attributed to the α decays of ^{208}Po and ^{210}Po, respectively. The ^{208}Po and ^{210}Po activities were produced in the α-decay chains starting from ^{220}Th and ^{222}Th, respectively, that were produced in a preceding experiment for calibration purposes. These three α activities were still present because the same DSSD detectors were used in this work.

The remaining peaks in the spectrum were assigned based on their energies and the observed half-lives (See Section 5.2.5) to ^{244}Cf ([Sikkeland67a]); E_α = 7.21(2) MeV, $T_{1/2}$ = 19.4(6) min, ^{243}Cf ([Sikkeland67a]; E_α = 7.06(2) MeV, $T_{1/2}$ = 10.3(5) min) and ^{240}Cm ([Singh08]; E_α = 6.290(5) MeV, $T_{1/2}$ = 27(1) d). ^{240}Cm is a long-lived daughter nucleus produced in the α decay of ^{244}Cf. The measured α peaks were fitted with Gaussian functions and correspond to energies of E_α = 7.21(3) MeV

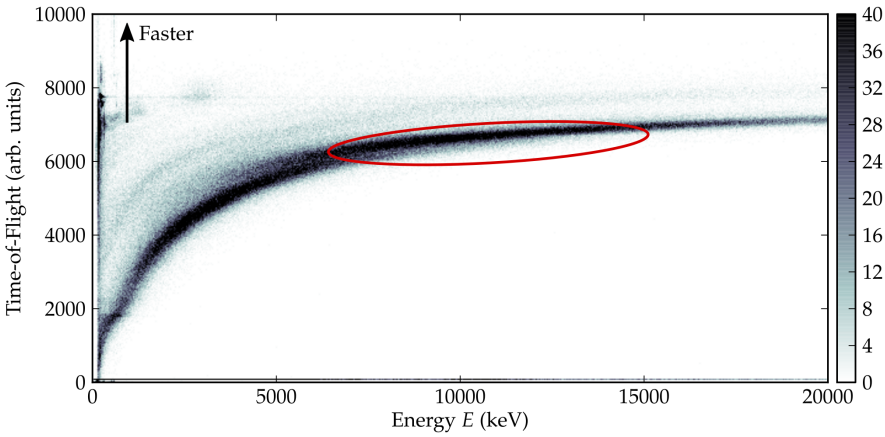

(a) Time-of-flight (ToF) between the MWPC and the DSSD versus the energy deposited in the DSSD (E).

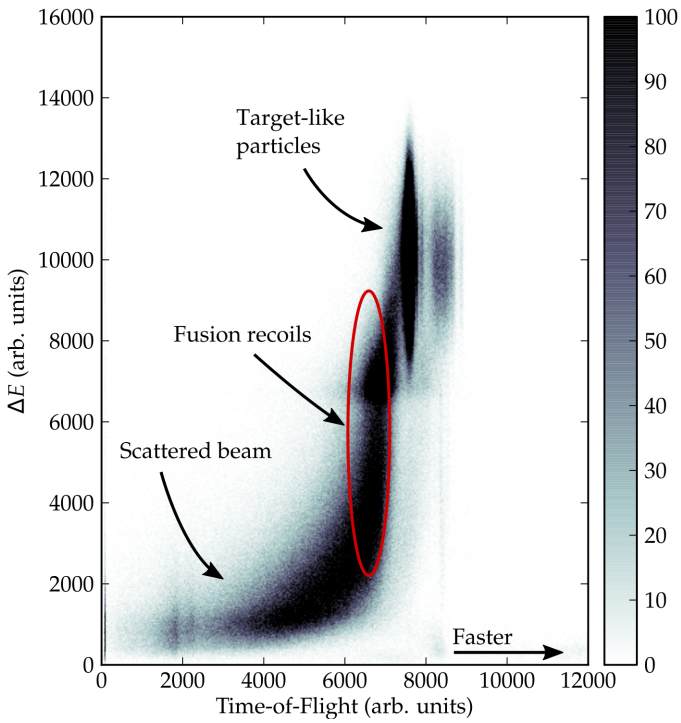

(b) Energy loss in the MWPC (ΔE) versus the time-of-flight (ToF) between the MWPC and the DSSD.

Figure 5.2. Recoil identification matrices in the ^{48}Ca + ^{198}Pt reaction using the (a) E-ToF and (b) ToF-ΔE methods. The approximate gates used in the analysis are indicated by the red regions. Please see the text for further details.

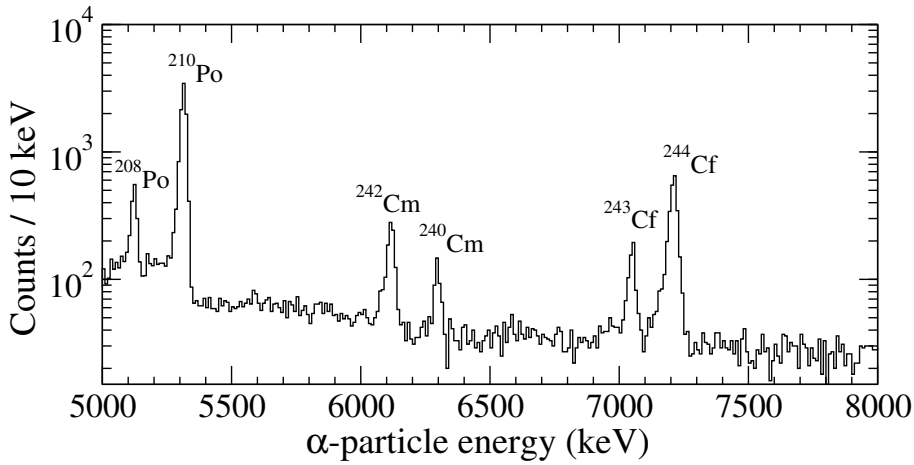

Figure 5.3. Energy spectrum of the α particles from the ^{48}Ca + ^{198}Pt reaction measured on the Y side of the DSSDs and vetoed with the gas counter (MWPC) and the Planar detector.

and $E_\alpha = 7.05(3)$ MeV for ^{244}Cf and ^{243}Cf, respectively. The uncertainty in the measurement is mostly due to the lack of a proper internal calibration that may cause systematic error on the measured energies. The α-decay branch in ^{239}Cm (the α-decay daughter of ^{243}Cf) has been reported to be very small and was not observed in this work. An upper limit of $b_\alpha(^{239}\text{Cm}) = 1.0 \cdot 10^{-5}$ is given in [Qin08].

It should be noted that 7.17(1) MeV α-particles attributed to the α decay of ^{243}Cf that were observed in the low-energy shoulder of the 7.21-MeV α activity of ^{244}Cf in [Fields67] were not seen in [Sikkeland67b, Sikkeland67a] or in this work. The energy resolution of the DSSD detectors used in this work was sufficiently high so that an α peak at the energy of 7.17 MeV should have been resolved if the intensity ratio is 2.5 (ratio of 7.06 MeV compared to 7.17 MeV) as given in [Fields67]. Nevertheless, it is possible that the intensity ratio is higher or the α-particle energy overlaps with the 7.21-MeV peak from ^{244}Cf making the observation of the 7.17-MeV α particles not possible in this work.

5.2.3 α-decay branch of ^{244}Cf

A measurement of the electron-capture (EC) decay branch in ^{244,243}Cf was not possible in this work due to the long half-lives and very low α-decay branching ratios of ^{243}Bk [Thompson50c] ($T_{1/2} = 4.6(2)$ h, $b_\alpha = 0.1\%$) and ^{244}Bk [Chetham-Strode56a] ($T_{1/2} = 4.35(15)$ h, $b_\alpha = 6(2) \cdot 10^{-3}\%$). Therefore, an α-decay branching ratio of $b_\alpha = 14.0\,\%$ for ^{243}Cf that has been estimated in the literature [Nesaraja14, Browne14]

using data from [Sikkeland67a] and [Fields67] was adopted. It should be noted that an estimate of EC/α = 10 is given in [Sikkeland67a].

A measurement of the α-decay branch of ^{244}Cf has not been reported previously. An estimate of b_α = 70(20) % that was based on theoretically calculated β-decay half-lives was recommended in [Akovali98]. In this work the α-decay branch of ^{244}Cf was estimated from experimental data from an earlier study of the decay properties of ^{248}Fm [Ketelhut10]. A value of b_α = 75(6) % was determined by comparing the number of α decays from ^{248}Fm and ^{244}Cf from a gas-vetoed α-particle energy spectrum measured during the experiment that is shown in Fig. 5.4. The uncertainty that is given is only based on the determination of the peak areas. Systematic error may be caused by possible losses when the data acquisition was not collecting data of α decays from ^{244}Cf due to its long half-life which was not taken into account. Therefore, the actual α-decay branch can be somewhat higher than the value presented here.

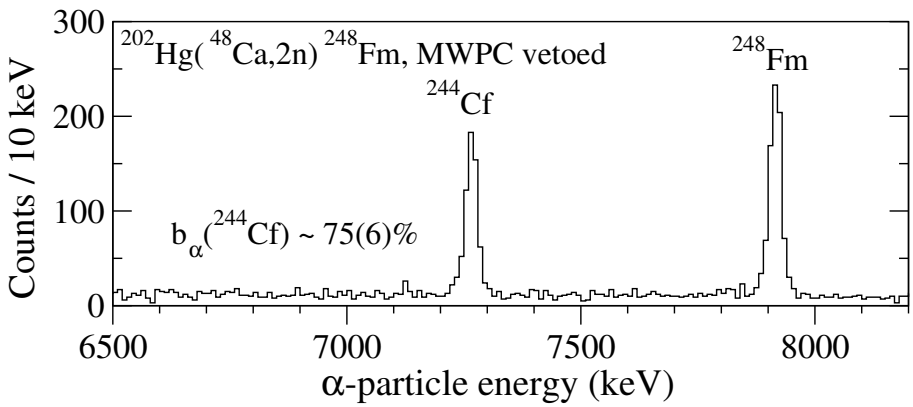

Figure 5.4. Energy spectrum of the α particles from the ^{48}Ca + ^{202}Hg fusion reaction measured in the DSSDs and vetoed with the gas counter (MWPC) from an earlier study of ^{248}Fm [Ketelhut10]. Note that the energies plotted on the x-axis are not corrected for the partially detected recoil energy of the daughter nucleus ($\approx$ 70 keV due to the pulse-height defect).

5.2.4 Excitation functions

The production of ERs in the fusion reaction of ^{48}Ca+^{198}Pt was measured as a function of the excitation energy of the compound nucleus ^{246}Cf* ranging from E^* = 23 up to 31 MeV in the beginning of the experiment to optimise the yield of the ^{244}Cf and ^{243}Cf nuclei of interest. The ^{48}Ca beam was accelerated to energies of 207, 208, 211 and 213 MeV. The thickness of the ^{198}Pt target used in the cross section measurements was 644 µg/cm^2 with an enrichment of 95%. Other possible isotopic abundances in the

target are *e.g.* ^{196,194}Pt. Fusion-evaporation reaction channels with ^{196,194}Pt would lead to more neutron-deficient products and are expected to have much lower cross sections. Two carbon foils with thicknesses of 216 and 413 µg/cm^2 were used in front of the target for the reduction of beam energies in the 211-MeV runs. The excitation energies E^* were calculated by using the atomic mass data from AME2003 [Audi03] and the LISE++ code [Tarasov04], and correspond to the excitation energies at the centre of the target. The energy loss of the beam particles in the first half of the target was $\Delta E \approx 2.5$ MeV. The beam energies at the centre of the target correspond to excitation energies of the compound nucleus ^{246}Cf* of about 23, 26, 27, 30 and 31 MeV.

The following factors were used to estimate the cross section [Sarén]: RITU transmission, DSSD coverage and DSSD full-energy α detection efficiency of 33(5) %, 83(5) % and 55(5) %, respectively. The main uncertainty in the data points comes from the beam dose estimate that is obtained from the integral of the total rate of the recoils observed at the focal plane and from the uncertainty in RITU transmission. Only the uncertainty of the beam energy from the cyclotron ($\pm 0.5\% \cdot E_{\mathrm{beam}}$) was taken into account when calculating the uncertainties in the excitation energies E^*. The α-decay branches of $b_\alpha = 75(6)$ % and $b_\alpha = 14.0$ % were used for ^{244}Cf and ^{243}Cf, respectively.

The measured cross sections for the 2n and 3n evaporation channels are shown in Fig. 5.5 and listed in Table 5.1 with more details. The maximum values for the measured production cross-sections of σ(2n, max) = 120(40) nb and σ(3n, max) = 170(80) nb were found at the excitation energies of about 26(1) MeV and 30(1) MeV at the centre of the target, respectively.

Table 5.1. A list of the measured cross sections of the fusion-evaporation reactions ^{198}Pt(^{48}Ca,2n)^{244}Cf and ^{198}Pt(^{48}Ca,3n)^{243}Cf determined in this work. The bombarding energy of the ^{48}Ca beam E_{beam} is as obtained from the cyclotron. The excitation energies E^* of the compound nucleus ^{246}Cf* correspond to the energies at the centre of the target. The thickness of the ^{198}Pt target was 644 µg/cm^2.

E^* (MeV)	E_{beam} (MeV)	Degrader (C, µg/cm^2)	σ(^{244}Cf, 2n) (nb)	σ(^{243}Cf, 3n) (nb)
23(1)	211(1)	413	30(20)	–
26(1)	211(1)	216	120(40)	–
26(1)	207(1)	–	110(40)	70(20)
27(1)	208(1)	–	110(40)	90(30)
30(1)	211(1)	–	60(30)	170(80)
31(1)	213(1)	–	9(3)	80(30)

The calculated cross section estimates obtained from the HIVAP [Reisdorf81] code for the 2n and 3n evaporation channels in the used reaction are also shown in Fig. 5.5 for comparison. The input parameters of the calculations were optimised to describe the fusion reactions of ^{34}S+^{208}Pb (dashed curves) and ^{48}Ca+^{208}Pb (dotted curves). The calculations overestimate the cross sections by roughly an order of magnitude.

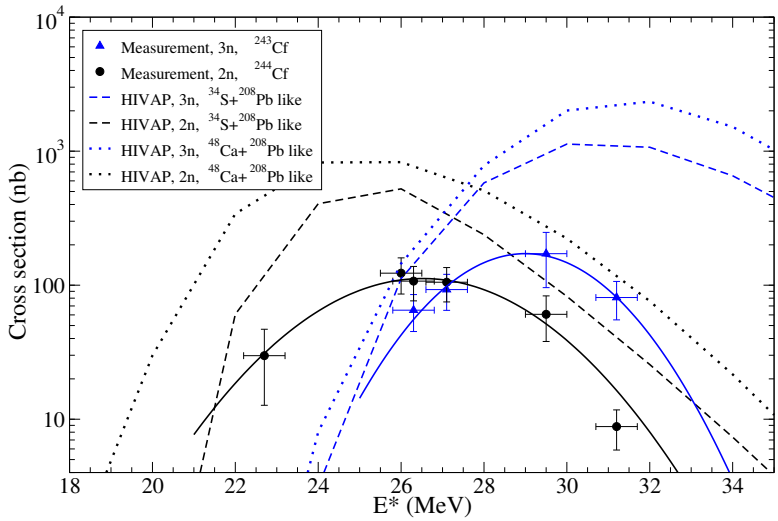

Figure 5.5. The measured cross sections of the ^{244,243}Cf produced in the fusion reaction ^{48}Ca+^{198}Pt as a function of the excitation energy E^* at the centre of the target of the compound nucleus ^{246}Cf*. The solid lines are fits to guide the eye. The dashed and dotted lines are estimates that have been calculated using the HIVAP code with the input parameters adjusted to describe the reactions of ^{34}S+^{208}Pb and ^{48}Ca+^{208}Pb, respectively. See text for details.

However, the predicted excitation energies E^* of the maxima, the overall shapes and relative magnitudes of the excitation functions are rather well reproduced by the HIVAP calculations.

5.2.5 Correlation analysis and half-lives

Correlated events where an ER implantation was followed by an α decay in the same pixel of the DSSDs was made with a maximum search time of up to 100 min. The α-particle events were assumed to have an energy in the range of 5 MeV$\leq E_\alpha \leq$8 MeV and in anticoincidence with gas counter (MWPC) or Planar detector signals. The resulting correlated α-particle energy spectrum is shown in Fig. 5.6. The total numbers of the correlated ER-α(^{244}Cf) and ER-α(^{243}Cf) pairs were about 2000 and 400, respectively.

In order to improve on the statistics in the tagged γ-ray spectra, also the PIN array of silicon detectors were used in the correlation analysis and the tagging procedure. A two-dimensional histogram of the energies of the correlated events where a recoil implantation was followed by an escape-α event measured on the X side of the DSSDs and a coincident event in the PIN detector within 100 min is shown in Fig. 5.7. The sum of the two energies indicated with the red area containing about 1000 events corresponds

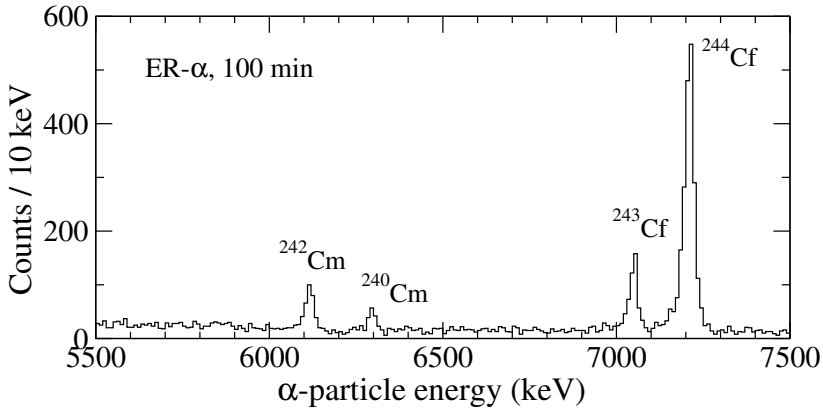

Figure 5.6. Energy spectrum of the ER correlated α particles following a recoil implantation within 100 min from the ^{48}Ca + ^{198}Pt reaction measured on the Y side of the DSSDs and vetoed with the gas counter (MWPC) and the Planar detector.

to the full-energy α particles from the α decays of ^{244,243}Cf. The α particles attributed to the α decays ^{240,242}Cm and ^{210,208}Po are also clearly visible. It should be noted that the statistics obtained in the experiment were not sufficient to make a proper energy calibration of the full-energy α particles as measured from the DSSD+PIN correlations. Therefore, the energy resolution obtained from the sum of the two energies is much worse than in the full-energy α peaks of the spectrum in Fig. 5.6. Furthermore, the α particles corresponding to ^{244,243}Cf cannot be distinguished properly. However, the contribution of the α decays from ^{243}Cf in the observed escape-α events is of the order of a factor of 1/5 roughly estimated from the ratio of the observed correlated full-energy α-particles of 2000/400.

The half-lives of the activities assigned to ^{244,243}Cf were determined from the time differences of the correlated ER-α events that are shown in Fig. 5.8. In the cases of ^{244}Cf (Fig. 5.8(a)) and ^{243}Cf (Fig. 5.8(b)) α-particle energy gates of E_α=7.12–7.27 MeV and E_α=6.98–7.09 MeV (compare with Fig. 5.6) were used, respectively. Only the full-energy α-particle events were used in the half-life analysis. The search time was expanded to include the random background components. Double exponential functions of the form given in Eq. 3.15 were used to fit the measured ER-α time spectra of Fig. 5.8(a) and (b). The half-lives deduced from the fitted parameters of the decay constant (λ) and the rate of the component arising from the random correlations (r) were $T_{1/2}$=19.3(12) min and r=8.4 $\cdot$ 10^{-5} for ^{244}Cf and $T_{1/2}$=10.9(5) min and r=8.4 $\cdot$ 10^{-5} for ^{243}Cf. The measured values are consistent within error bars with previously reported values [Sikkeland67a] of $T_{1/2}$ = 19.4(6) min for ^{244}Cf and $T_{1/2}$ = 10.3(5) min for ^{243}Cf. The random background rates from both of the fits are well in agreement with the average counting rate of the ERs in the individual DSSD pixels during the experiment of about 1 $\cdot$ 10^{-4} Hz/pixel.

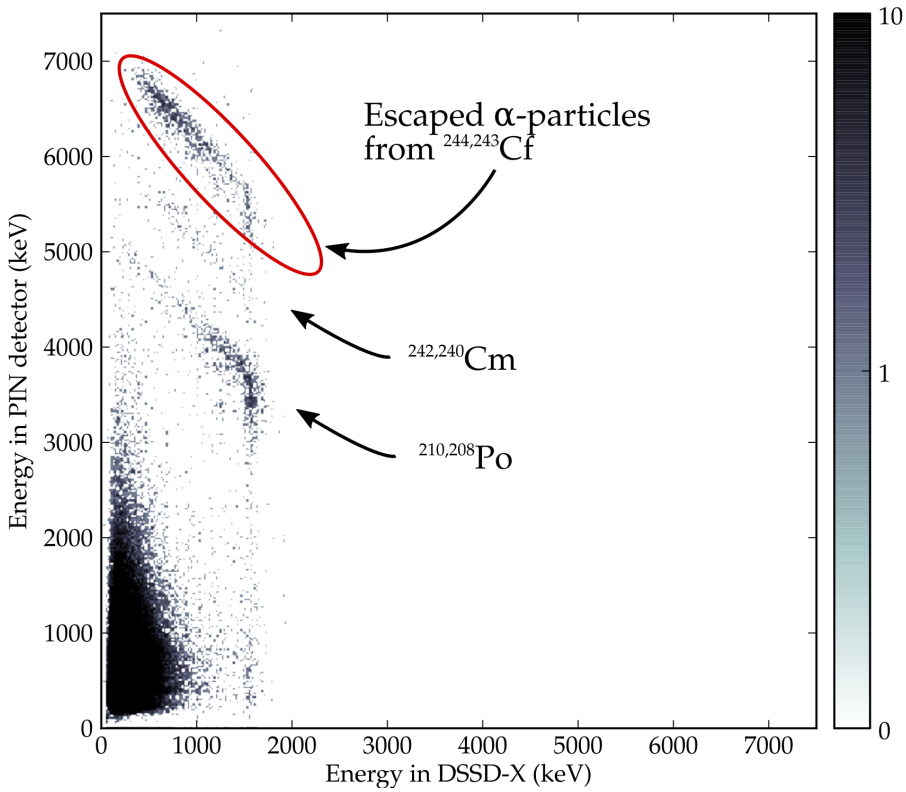

Figure 5.7. Energies of the correlated α-like events in the PIN detectors versus the energy deposited in the X side of the DSSDs following a recoil implantation within 100 min. All of the events have been vetoed with the gas counter (MWPC) and the Planar detector.

5.2.6 Ground-state rotational band of ^{244}Cf

The prompt γ-ray singles spectrum measured at the target position with JUROGAMII and associated with fusion-evaporation residues (recoil-gated γ-ray singles) is shown in Fig. 5.9(a). An additional time gate to select γ rays was made by placing two-dimensional polygonal gate conditions on a matrix of the MWPC-DSSD ToF vs. the time difference between the JUROGAMII γ-ray event and the recoil implantation in the DSSD. The obtained recoil-gated γ-ray singles or the γ-γ coincidence spectra were not clean enough to clearly identify and distinguish the transitions in ^{244}Cf, ^{243}Cf and other reaction products. However, X-rays originating the produced Cf nuclei are clearly visible. In addition, a large number of X-rays from Pt as well as the $2_1^+ \rightarrow 0_{\text{g.s.}}^+$ and $2_2^+ \rightarrow 2_1^+$ transitions from the Coulomb excitation of the ^{198}Pt target can be seen. The 407-keV peak is very broad mostly due to the Doppler correction that is applied to the

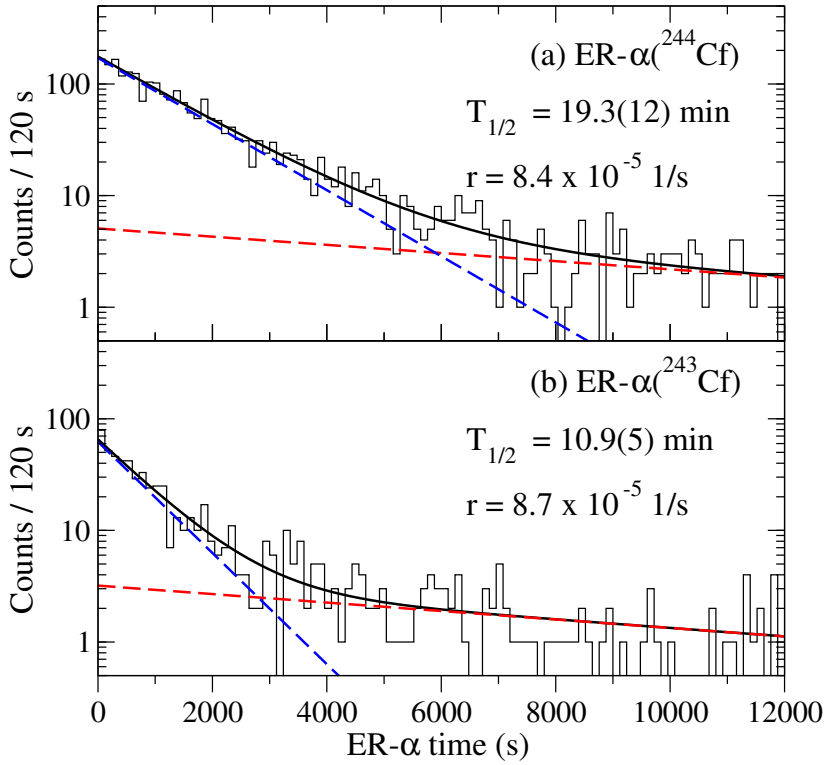

Figure 5.8. The measured time differences of the correlated ER-α events corresponding to (a) ^{244}Cf and (b) ^{243}Cf with a maximum search time of up to $12{\cdot}10^3$ s shown. The dashed lines in blue (decay constant $\lambda + r$) and red (decay constant r) correspond to the two components of the fitted decay curve according to Eq. 3.15 that is shown in black.

γ-ray energies that are measured in the JUROGAMII detector rings positioned at different angles with respect to the beam direction but also due to the straggling effects in the target and the fact that Coulomb excitation is a binary reaction.

The recoil-decay tagging (RDT) method was used to obtain γ-ray spectra corresponding only to ^{244}Cf. The prompt γ-ray singles spectrum tagged with the α decays of ^{244}Cf is shown in Fig. 5.9(b) and up to γ-ray energies of 1 MeV in Fig. 5.10. In addition, the PIN array was used in the tagging procedure with the approximate gate shown in Fig. 5.7 to improve the statistics by detecting those α particles that escape the DSSDs depositing only part of their full energy which are then stopped in the PINs. In this γ-ray spectrum the X-rays from ^{244}Cf are still clearly visible. The measured γ-ray spectrum shows a clear sequence of eight transitions with regular spacing. Such a cascade is characteristic of a rotational band of a deformed nucleus. The transitions associated with the ground-state rotational band have been labelled with their transition

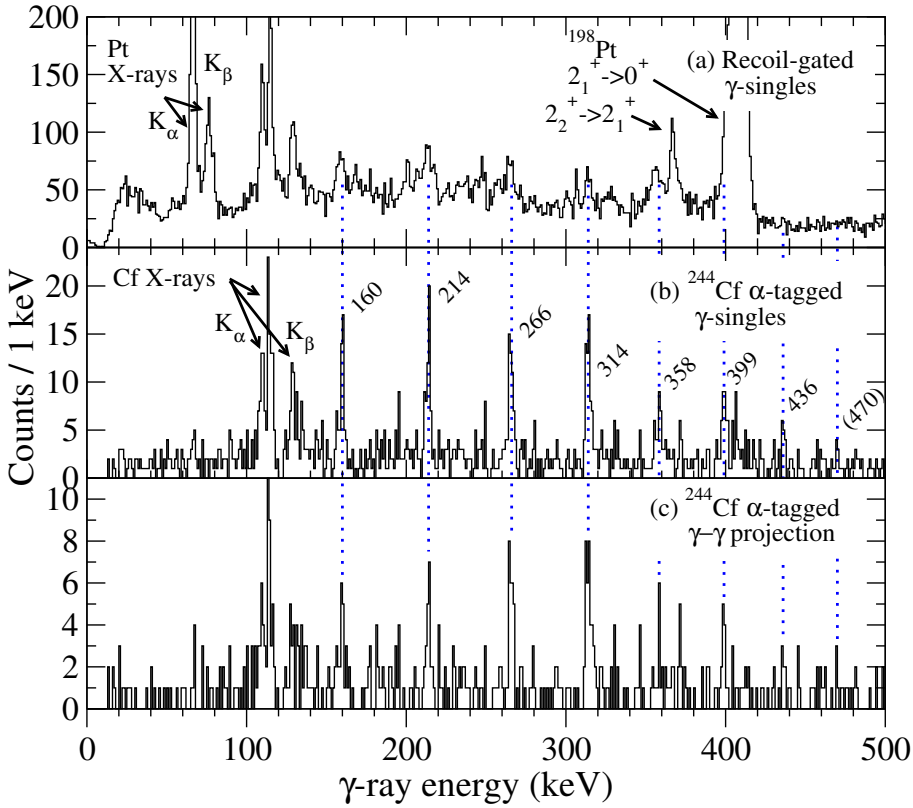

Figure 5.9. Prompt γ rays measured at the target position with JUROGAMII. (a) Recoil-gated γ-ray singles; (b) ^{244}Cf α-tagged (DSSD+PIN) γ-ray singles; (c) Projection of the ^{244}Cf α-tagged (DSSD) γ-γ coincidence matrix. The locations of the peaks corresponding to the ground-state rotational band have been indicated by the dotted lines.

energies and marked with dotted lines. At least one peak at an energy of 704(1) keV visible in Fig. 5.10 possibly originates from a side band feeding the low-spin states of the ground-state rotational band.

The assignment of the regularly spaced transitions to the ground-state rotational band of ^{244}Cf is further supported by Fig. 5.9(c) where a total projection of the ^{244}Cf α-tagged γ-γ coincidence matrix is shown. Only the full-energy α decays in the DSSD corresponding to ^{244}Cf were used in the tagging procedure to produce the spectrum to reject possible contamination from transitions belonging to ^{243}Cf. The rotational sequence remains visible and the background is greatly reduced in the projected γ-γ spectrum and by gating on the transitions in the γ-γ matrix they appear to be a cascade of coincident transitions. However, due to the low statistics in the γ-γ coincidence data,

the assignment of the 470-keV γ ray to the band should be taken as tentative. It should be noted that the peak at 407 keV corresponding to the $2_1^+ \rightarrow 0_{g.s.}^+$ transition from the Coulomb excitation of the ^{198}Pt target completely disappears in the γ-γ spectrum. The statistics in the γ-γ coincidences were not sufficient to determine which state is fed by the 704-keV transition. It is highly likely that the transition feeds one of excited states with the lowest spins in the ground-state rotational band and the coincident transitions are not seen due to the fact that the low-energy transitions are highly converted.

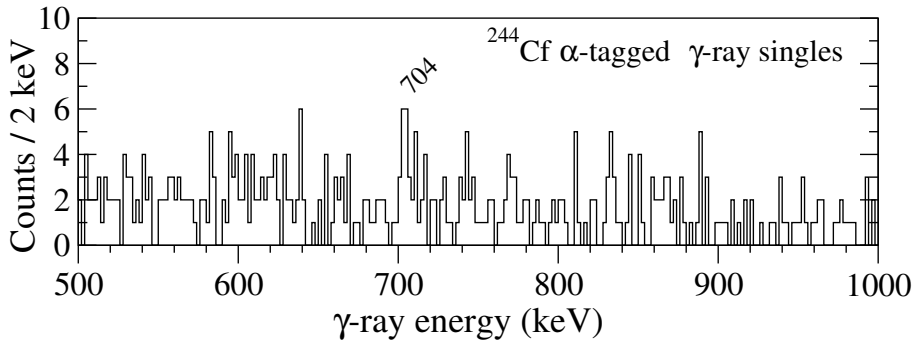

Figure 5.10. Prompt γ rays with energies up to 1 MeV measured at the target position with JUROGAMII and tagged with ^{244}Cf α decays in the DSSDs+PINs.

The measured peak energies of the transitions in the ground-state rotational band are listed in Table 5.2 with the tentative spin assignments and relative intensities corrected with the γ-ray detection efficiencies and the internal conversion coefficients calculated using BrIcc [Kibédi08] under the assumption of transitions with E2 character. The peak energies and areas were extracted from fits to the ^{244}Cf α-tagged γ-ray singles spectrum of Fig. 5.9(b). Transitions up to the tentative spin and parity of $I^\pi = 20^+$ were identified with reasonable confidence. The 314-keV transition is possibly a doublet based on the increased width and higher than expected intensity of the transition. The width of the peak is more apparent in the γ-γ coincidence spectra. Therefore, the peak area of the 314-keV transition was estimated with two Gaussian functions with the peak widths fixed to 2 keV. Determination of the 399-keV peak area is challenging from the spectrum due to the overlap with the wide 407-keV peak from ^{198}Pt.

The two lowest transitions of $4^+ \rightarrow 2^+$ and $2^+ \rightarrow 0^+$ in the ground-state rotational band could not be observed because they proceed mostly via internal conversion. The calculated internal conversion coefficients [Kibédi08] are 1045(19) and 19.4(10) for the 45-keV and 103-keV transitions of E2 character, respectively. The unobserved transition energies were determined by extrapolating from the fitted kinematic ($\mathcal{J}^{(1)}$) and dynamic ($\mathcal{J}^{(2)}$) moments of inertia of the rotational band according to the Harris formalism [Harris65] using Eq. 2.6, 2.7 and 2.11. The same procedure was followed that has been used *e.g.* in the studies of the rotational properties of ^{256}Rf [Greenlees12] and ^{252}No [Herzberg01, Sulignano12].

Table 5.2. The measured transition energies and tentative assignments for the ground-state rotational band of ^{244}Cf. The extrapolated $4^+ \rightarrow 2^+$ and $2^+ \rightarrow 0^+$ transitions are also shown. The relative intensities have been corrected for γ-ray detection efficiency and internal conversion.

$J_i \rightarrow J_f$	E_γ (keV)	Relative intensity (%)
$(2^+ \rightarrow 0^+)$	45(1)†	
$(4^+ \rightarrow 2^+)$	103(1)†	
$(6^+ \rightarrow 4^+)$	160(1)	100(22)
$(8^+ \rightarrow 6^+)$	214(1)	60(10)
$(10+ \rightarrow 8^+)$	266(1)	54(8)
$(12^+ \rightarrow 10^+)$	314(1)‡	30(10)
$(14^+ \rightarrow 12^+)$	358(1)	31(8)
$(16^+ \rightarrow 14^+)$	399(1)	33(11)
$(18^+ \rightarrow 16^+)$	436(1)	13(6)
$(20^+ \rightarrow 18^+)$	470(1)	7(6)

† Transition energy extrapolated from the Harris fit.
‡ Transition is assumed to be a doublet.

The measured $\mathcal{J}^{(1)}$ and $\mathcal{J}^{(2)}$ as a function of the rotational frequency ($\hbar\omega$) calculated using Eq. 2.5 and 2.8 are shown in Fig. 5.11. The transition with the lowest observed energy of 160 keV was assumed in the fitting procedure to originate from a state with $I^\pi = 6^+$ that is typical in this region in the isotones as well as in the region of the heavier elements such as No and Fm. Any other choice for the initial spin assignment of this transition would not give reasonable results from the fitting. The Harris parameters $(\mathcal{J}_0, \mathcal{J}_1)$ obtained from the fit of $\mathcal{J}^{(1)}$ to the five lowest transitions of the rotational band using Eq. 2.6 were $\mathcal{J}_0 = 67.3(2)\,\hbar^2\text{MeV}^{-1}$ and $\mathcal{J}_1 = 250(10)\,\hbar^2\text{MeV}^{-3}$. The resulting fit of $\mathcal{J}^{(1)}$ that has been plotted using Eq. 2.6 is shown in Fig. 5.11. The dashed line corresponding to $\mathcal{J}^{(2)}$ has been plotted using Eq. 2.7 and the same parameters that were obtained from the fit to the low-spin part of $\mathcal{J}^{(1)}$ data. The transition energies extrapolated for the two lowest transitions by using the obtained Harris parameters and Eq. 2.11 were $E_\gamma(4^+ \rightarrow 2^+) = 103(1)$ keV and $E_\gamma(2^+ \rightarrow 0^+) = 45(1)$ keV.

Further support for the 103-keV transition energy of the $4^+ \rightarrow 2^+$ transition was found by estimating the intensity ratio of the Cf K_α/K_β X-rays. The ratio matches closely to the literature value and does not show an excess of possible γ-rays from the $4^+ \rightarrow 2^+$ transition that could overlap with the K_α peaks. On the other hand, with the internal conversion coefficient calculated with BrIcc for the transition assuming an E2 character being as high as 19.4(10) would mean that only few γ rays could be observed with the level of statistics that is available in this work. It should also be noted that the 103-keV region in the α-tagged γ-ray spectra is very clean from background and does not show any peaks.

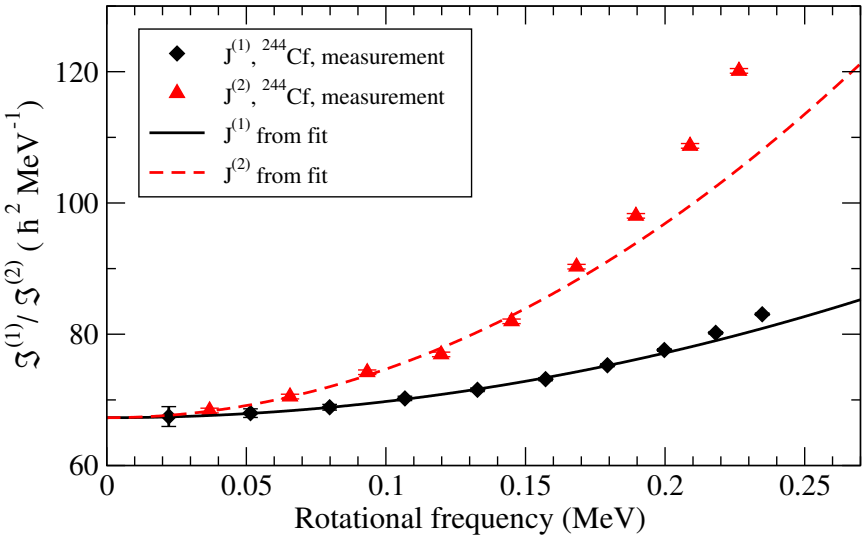

Figure 5.11. The kinematic $\mathcal{J}^{(1)}$ and dynamic $\mathcal{J}^{(2)}$ moments of inertia of the ground-state rotational band of ^{244}Cf as a function of the rotational frequency ($\hbar\omega$). The lines are plotted with Eq. 2.6 and Eq. 2.7 by using the Harris parameters obtained from a fit to the low-spin part of the $\mathcal{J}^{(1)}$ data with Eq. 2.6. See the text for more details.

5.3 Discussion

The proposed level scheme that was deduced for ^{244}Cf in this work is shown in Fig. 5.12 showing the ground-state rotational band up to a tentative spin of $I^{\pi} = 20^{+}$. Observation of the rotational band and the excitation energy determined for the first excited 2^{+} state shows that it has a similar deformation when compared to other nuclei in the region. In fact, prolate quadrupole deformation parameters (β_2) of 0.239 [Sobiczewski01] and 0.249 [Möller16] have been obtained from the theoretical calculations for ^{244}Cf.

The observed high-energy γ-ray transition of 704 keV in the spectra could not be placed exactly in the level scheme due to low statistics. The absence of γ-γ coincidences suggests that it feeds one of the low-spin states of the ground-state rotational band. It possibly originates from a negative parity side band and the transition could have E1 character if coming from a state with spin and parity of 1^{-}. Alternatively the spin and parity could be $3^{-}, 5^{-}, \ldots$ if it is feeding an excited state higher in energy in the ground-state rotational band. This negative parity band could be an $K^{\pi} = 0^{-}, 1^{-}$ octupole-vibrational band built from the strong coupling of an octupole phonon excitation to the quadrupole deformed core [Donner66]. Such rotational band-head states with negative parity and odd spins have been identified and interpreted at low excitation energies of 0.6-1.0 MeV in the even-even $N = 146$ isotones of *e.g.* ^{240}Pu [Hackman98, Wiedenhöver99] and ^{238}U [Ward96].

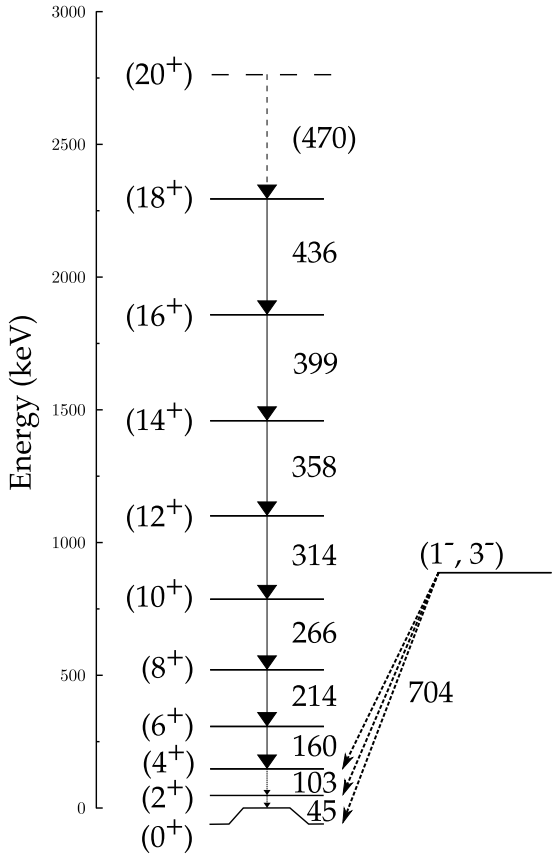

Figure 5.12. The proposed level scheme of ^{244}Cf from this work showing the transition energies and the tentative spin and parity assignments.

Another possibility for the origin of the 704-keV γ-ray transition is a two quasi-particle (2-qp) excitation that would lie at an excitation energy of about $E^* = 1$ MeV. According to theoretical calculations [Delaroche06] a neutron 2-qp state with a configuration of ($K_1^{\pi_1}$=5/2$^+$, $K_2^{\pi_2}$=7/2$^-$) giving possible spins and parities of I^π=1$^-$, 6$^-$ has been predicted at an excitation energy of about E^*=0.9 MeV.

The statistics obtained for ^{243}Cf were not sufficient in this work to associate any prompt γ-ray transitions to this nucleus. The low α-decay branch in ^{243}Cf did not allow to take full advantage of the use of the recoil-decay-tagging method in order to extract a clean prompt γ-ray spectrum corresponding to ^{243}Cf.

5.3.1 Systematics in the $N = 146$ isotones

The measurement of the transitions in the ground-state rotational band of ^{244}Cf up to a tentative spin and parity of $I^{\pi} = 20^{+}$ in this work allows a comparison to be made for the first time with a complete set of even-even neutron-deficient uranium and transuranium $N = 146$ isotones and their rotational properties.

The measured kinematic $\mathcal{J}^{(1)}$ and dynamic $\mathcal{J}^{(2)}$ moments of inertia of the ground-state rotational bands as a function of the rotational frequency ($\hbar\omega$) in the even-even N=146 isotones are shown in Fig. 5.13(a) and 5.13(b), respectively. The results that were obtained in this work on ^{244}Cf (open symbols) are compared to previous measurements (closed symbols) of ^{238}U [Ward96], ^{240}Pu [Hackman98], ^{242}Cm [Abu Saleem04] and ^{246}Fm [Piot12]. The lines are drawn using Eq. 2.6 and 2.7 and the Harris parameters that were obtained from fits made to the low-spin part of the measured $\mathcal{J}^{(1)}$ data of each nucleus in the same way as was described for ^{244}Cf in Section 5.2.6.

The absolute values of the kinematic moments of inertia at low-spin are closely related to the energy of the first excited 2^{+} state. In turn, the energy of the first excited 2^{+} state can be further related to the quadrupole deformation [Pomorski73]. Moreover, in the region of the deformed shell gaps the lowering of the 2^{+} states can be related to reduced pairing correlations [Sobiczewski01]. The reduction in the pairing correlations result in an increase in the moment of inertia. Fig. 5.13(a) shows that among the presented even-even $N = 146$ isotones, ^{242}Cm has the highest value of the kinematic moment of inertia at low spin ($\mathcal{J}^{(1)}$) just above that of ^{240}Pu. The $\mathcal{J}^{(1)}$ value of ^{244}Cf obtained in this work is closer to and only a little higher than that of ^{238}U. Finally, ^{246}Fm has the lowest $\mathcal{J}^{(1)}$ value of the group. More interesting features are revealed by comparing the behaviour of the dynamic moments of inertia ($\mathcal{J}^{(2)}$) of these isotones.

From the $\mathcal{J}^{(2)}$ data shown in Fig. 5.13(b) and Fig. 5.11 it is evident that there is a sharp increase in the dynamic moment of inertia in ^{244}Cf at a rotational frequency of about $\hbar\omega = 0.2$ MeV. A similar up-bend has been observed clearly in ^{238}U and is very likely to occur also in ^{246}Fm based on the highest transitions that have been observed in the ground-state band and a next tentative transition in the band [Piot]. In contrast, ^{242}Cm and ^{240}Pu that have a higher kinematic moment of inertia $\mathcal{J}^{(1)}$ do not show any signs of up-bend in the dynamic moment of inertia $\mathcal{J}^{(2)}$ up to rotational frequencies as high as $\hbar\omega = 0.25$ MeV. One possible physical explanation for the up-bending behaviour is the alignment of coupled protons or neutrons in the high-j orbitals to the rotational axis of the nucleus due to the Coriolis effect. With high angular momentum the strong Coriolis force can break the pairing correlations of the coupled nucleons resulting in band-crossing phenomena and changes in the moment of inertia of the system.

In a few cases it has been studied experimentally whether the alignment is caused by the protons or the neutrons in high-j orbitals. For example, it has been shown by g-factor measurements that the up-bend at $\hbar\omega \approx 0.25$ MeV of the ground-state band in ^{238}U and ^{232}Th ($N = 142$) results mostly from the alignment of a pair of protons in the $i_{13/2}$

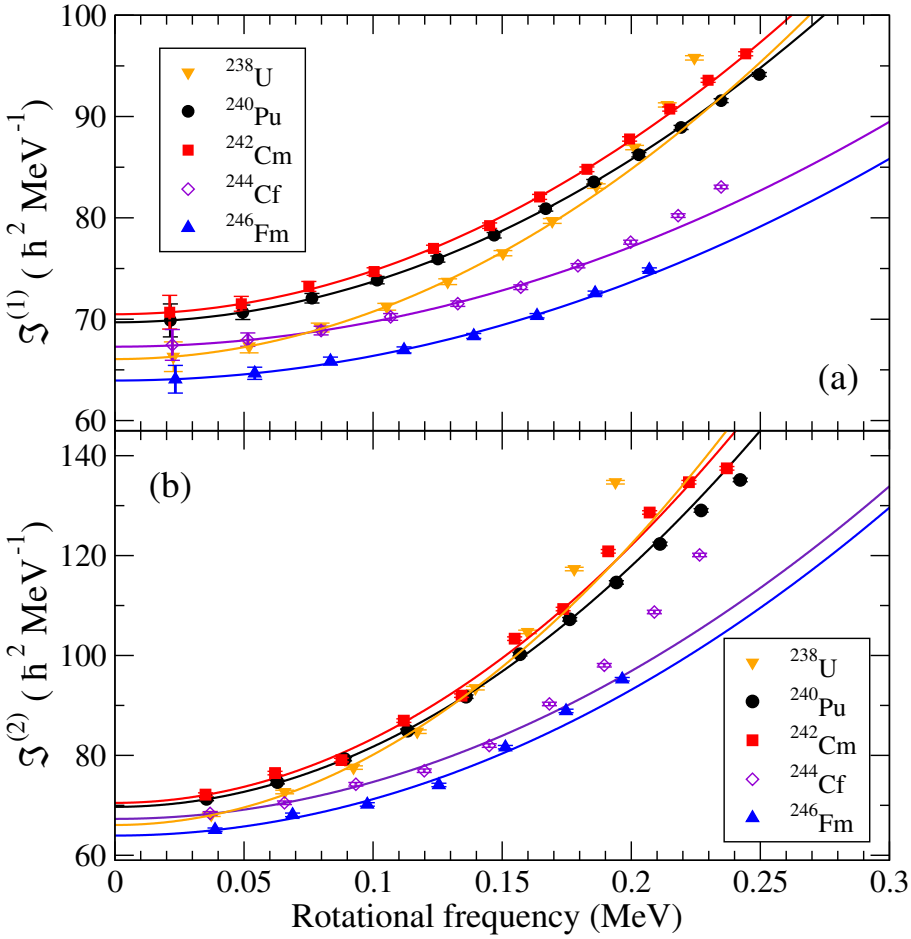

Figure 5.13. The (a) kinematic $\mathcal{J}^{(1)}$ and (b) dynamic $\mathcal{J}^{(2)}$ moments of inertia of the ground-state rotational bands as a function of rotational frequency ($\hbar\omega$) in the even-even N=146 isotones ^{238}U [Ward96], ^{240}Pu [Hackman98], ^{242}Cm [Abu Saleem04], ^{244}Cf (from this work) and ^{246}Fm [Piot12]. The lines represent (a) fits to the low-spin part of the $\mathcal{J}^{(1)}$ data using the γ-ray transition energies with Eq. 2.6 and (b) $\mathcal{J}^{(2)}$ plotted using Eq. 2.7 and the Harris parameters obtained in (a). See the text for more details.

orbital according to [Zhu10, Häusser82]. However, in ^{232}Th a small contribution from neutron alignment was estimated [Häusser82]. Additionally, in [Hota14] it has been shown that in the $N = 151$ isotones of ^{245}Pu, ^{247}Cm and ^{249}Cf the alignment behaviour is mostly caused by $i_{13/2}$ protons on the basis of odd-neutron orbital blocking arguments. Similar studies and results were proposed [Abu Saleem04] on ^{241}Cm ($N = 145$) and ^{237}Np ($N = 144$) based on blocking arguments. In [Hurst10] the alignment in ^{235}Np ($N = 142$) was studied and the role of $j_{15/2}$ neutrons has been proposed, although, the proton contribution could not be ruled-out. Therefore, it seems that in most cases the alignment effects are in fact caused by the protons active in high-j orbitals and experimental evidence for the neutrons contributing to the alignment effect is sparse or not conclusive. In theoretical calculations on the rotational properties such a clear distinction between the proton and neutron alignment is not evident, as discussed further in the next section.

5.3.2 Theoretical calculations

Only a few recent theoretical calculations have been made on the rotational properties of the ground-state bands in the region of the heavy even-even N=146 isotones that are discussed and closely related to this work.

The cranked relativistic Hartree-Bogoliubov (RHB) theory has been applied by Afanasjev *et al.* [Afanasjev13] to perform extensive calculations in the actinides and light superheavy elements including the heavy N=146 isotones. It is remarkable that the absolute values of $\mathcal{J}^{(1)}$ and the relative differences between all of the even-even N=146 isotones presented in Fig. 5.13(a) are rather well reproduced at low spin. However, an up-bend is predicted in all of the isotones by the calculations and the up-bend in ^{238}U and ^{240}Pu is predicted to occur at lower rotational frequency than in ^{242}Cm, ^{244}Cf and ^{246}Fm. Furthermore, in all of the cases the calculations indicate that both the neutron and proton contributions to the alignment occur simultaneously at the same frequency. Moreover, the calculated contribution of the neutrons to the kinematic moment of inertia is larger than that of the protons in all of the isotones. The calculated $\mathcal{J}^{(1)}$ of ^{244}Cf as a function of the rotational frequency is shown in Fig. 5.14 with the contributions from the protons (red) and neutrons (green) shown in the inset. It should be noted that octupole correlations are not taken into account in the calculations. In ^{240}Pu it has been suggested that the non-observation of the alignment is due to strong octupole correlations [Wiedenhöver99, Wang09]. Likewise, a self-consistent mean-field calculation of ^{240}Pu with the SLy4 interaction that does not include octupole correlations predicts an up-bend in $\mathcal{J}^{(2)}$ [Bender03].

Considering the ground-state deformations and the role of the octupole correlations, it is interesting to note that in [Agbemava16] a non-zero octupole deformation (β_3) is predicted for the ground states of ^{242}Cm and ^{240}Pu as well as for ^{238}U by using the RHB and covariant density functional theory (CDFT). Despite the possibly similar calculated octupole correlations in their ground states, experimentally ^{238}U shows

alignment effects starting at rotational frequencies of about $\hbar\omega \approx 0.2$ MeV, whereas, ^{240}Pu and ^{242}Cm do not.

Another theoretical study has been made using the cranked Hartree-Fock-Bogoliubov method with the Gogny D1S force on the even-even actinides [Delaroche06]. In their work, the experimentally observed up-bend in ^{244}Cf is not predicted. In the case of ^{240}Pu an up-bend is again predicted possibly due to the missing treatment of the octupole correlations. In ^{246}Fm the predicted up-bend is delayed up to a rotational frequency of $\hbar\omega \approx 0.3$ MeV. The predicted results are consistent with experimental results for ^{238}U showing an up-bend at $\hbar\omega \approx 0.2$ MeV and no alignment features in ^{242}Cm at $\hbar\omega \leq 0.3$ MeV.

In another recent theoretical study of nuclei in the region of ^{252,254}No [Liu12] the up-bend in ^{246}Fm at $\hbar\omega \approx 0.2$ MeV is predicted correctly, although, the absolute value of $\mathcal{J}^{(1)}$ at low spin is overestimated. In that work, Total Routhian Surface (TRS) calculations based on the cranked shell model including pairing correlations were made. Another theoretical calculation using spectroscopic quality energy-density functionals based on the Skyrme Hartree-Fock-Bogoliubov and Lipkin-Nogami methods were used to calculate the rotational bands of nuclei in the nobelium region [Shi14] in which an up-bend in ^{246}Fm was predicted. Unfortunately, the calculations reported in the latter two studies did not include the lighter $N = 146$ isotones that are discussed in this work.

New calculations were performed by Y. Shi and J. Dobaczewski for the ground-state band of ^{244}Cf by following the same theoretical methods and framework as were used in [Shi14]. The results for the kinematic $\mathcal{J}^{(1)}$ moment of inertia from the calculation are shown with a dashed black line in Fig. 5.14 together with the measured data points from this work. Calculations of $\mathcal{J}^{(1)}$ from [Afanasjev13] using the NL3* parametrisation are included in the same figure with a dash-dotted red line. The inset shows the proton (red) and neutron (green) contributions to the moment of inertia. It is evident, that the up-bend in $\mathcal{J}^{(1)}$ is predicted by both calculations. According to [Afanasjev13], the alignment would occur at the same frequency for protons and neutrons and that the neutrons have a larger contribution. Strikingly, the absolute value of $\mathcal{J}^{(1)}$ at low-spin calculated by Y. Shi *et al.* is very close to the experimental value and well within the uncertainties.

In all of the available extensive theoretical calculations [Afanasjev13, Delaroche06, Bender03] both neutrons and protons in high-j orbitals contribute to the up-bend in the the moments of inertia. Moreover, in [Afanasjev13] the contributions of the different nucleons to the alignment have been extracted and presented explicitly and they appear to mostly align simultaneously at the same rotational frequency. On the contrary, measurements to date have shown no clear evidence for the neutron alignments meaning that only protons in high-j orbitals would be responsible for the alignment. More theoretical calculations including the effects of octupole correlations are needed in this region in order to understand and reproduce the experimentally observed alignment properties in the presented $N = 146$ isotones.

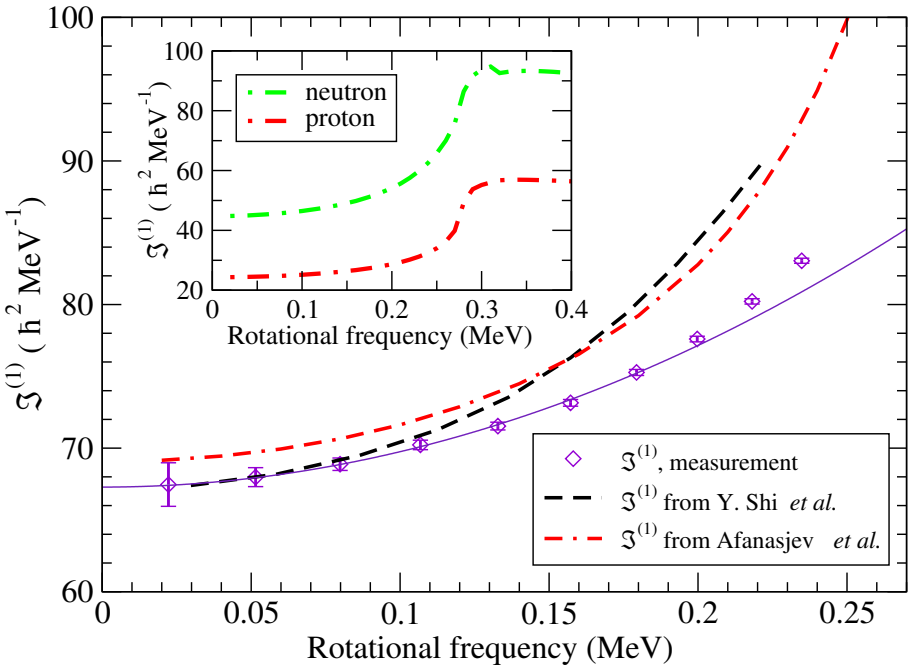

Figure 5.14. The kinematic $\mathcal{J}^{(1)}$ moment of inertia of the ground-state rotational band of ^{244}Cf as a function of the rotational frequency ($\hbar\omega$). The measured values from this work are compared to theoretical calculations provided by courtesy of A. Afanasjev using the NL3* parametrisation (dash-dotted red line) [Afanasjev13] with the inset showing the calculated proton (red) and neutron (green) contributions. Calculations performed in a similar way as described in Y. Shi *et al.* [Shi14] (dashed black line) are also included. The solid line represents a fit to the low-spin part of $\mathcal{J}^{(1)}$ data using the measured γ-ray transition energies with Eq. 2.6. See text for details.

5.4 Future prospects

This study was challenging mostly due to the long half-lives of ^{244}Cf and ^{243}Cf and the need to use RDT in order to obtain clean prompt γ-ray spectra. The recoil gating method was not sufficient due to the poor separation of the ERs from target-like reaction products. In addition, the small α-decay branch of ^{243}Cf does not allow to use the recoil-decay tagging up to its full potential. It would be interesting to try to disentangle the complex level-scheme structure of the odd-A nucleus ^{243}Cf and to study its poorly known decay properties with higher statistics in a future experiment. A dedicated experiment using a higher bombarding energy than in this work would be needed to enhance the production of ^{243}Cf nuclei in the 3n reaction channel. Alternatively, more data would be needed to determine the origin of the high-energy γ-ray transitions in ^{244}Cf that could be feeding the low-spin states in the ground-state rotational band.

Furthermore, it would be of interest to extend the systematic studies of the excited states to the neighbouring Cf nuclei such as ^{246}Cf and ^{242}Cf. The first excited 2^+ energy in the neutron mid-shell Cf isotopes is expected to be at the minimum in either ^{246}Cf or ^{248}Cf [Theisen15]. In contrast to *e.g.* Fm and No isotopes that exhibit features of a deformed shell gap occurring at $N = 152$, the shell gap appears to be shifted down to $N = 148$ or $N = 150$ in californium [Theisen15]. To date, there are no theoretical explanations for this effect and it is not yet fully understood. In addition, more data would be needed in the ground-state rotational band of ^{246}Fm in order to confirm the possible up-bend.

Chapter 6

Summary

In this work the hitherto unknown neutron-deficient nuclei ^{240}Es and ^{236}Bk were synthesised by using the fusion-evaporation reaction ^{209}Bi(^{34}S,3n)^{240}Es and the RITU gas-filled recoil separator coupled to the GREAT spectrometer. The half-lives of the isotopes were measured to be 6(2) s (^{240}Es) and 22^{+13}_{-6} s (^{236}Bk). The α particles with energies of E_α = 8.19(3) MeV and 8.09(3) MeV were assigned to the α decay of ^{240}Es. Furthermore, two weaker α activities with E_α = 8.02(3) MeV and 7.97(3) MeV were tentatively assigned to ^{240}Es. The assignments were supported by the observed correlated α-decay chains leading down to the previously known ^{236}Cm. Electron-capture (EC) decay and electron-capture delayed fission (ECDF) branches were assigned to both isotopes and P_{ECDF} were estimated to be 16(6)% and 4(2)% for ^{240}Es and ^{236}Bk, respectively.

The measured ECDF branches in both of the new isotopes extend the experimental data that is available in the heavier odd-odd Es and Bk isotopes. Furthermore, the ECDF branches showed a continuation in the exponential increase of the ECDF probabilities (P_{ECDF}) as a function of $Q_{\mathrm{EC}} - B_{\mathrm{sf}}$ when approaching the proton dripline. This dependence has not yet been fully understood and may strongly be affected by the shape of the fission barrier. Obtaining more experimental data on P_{ECDF} values in the more neutron-deficient isotopes of these elements would shed more light on this complicated decay process.

The second part of this work was devoted to an in-beam γ-ray spectroscopic study of ^{244}Cf. In the experiment, the neutron-deficient californium nuclei ^{244,243}Cf were produced in the fusion-evaporation reactions ^{198}Pt(^{48}Ca,2n)^{244}Cf and ^{198}Pt(^{48}Ca,3n)^{243}Cf, respectively. The excitation functions of the two reaction channels were measured. The half-lives of ^{244}Cf and ^{243}Cf were estimated from the ER-α correlations to be $T_{1/2}$ = 19.3(12) min and $T_{1/2}$ = 10.9(5) min, respectively. The α-decay branch of ^{244}Cf was estimated in this work by using data from a previous experiment to be b_α = 75(6) %,

however, due to the long half-life the actual α-decay branch can be somewhat higher than the value presented here. The excited states in ^{244}Cf were studied for the first time in this work. The ground-state rotational band was identified up to a tentative spin and parity of $I^{\pi} = 20^{+}$.

The deduced moments of inertia of the ground-state rotational band of ^{244}Cf indicate an up-bend due to a possible alignment of nucleons in high-j orbitals at a frequency of about $\hbar\omega = 0.2\,\mathrm{MeV}$. The results were compared to other even-even $N = 146$ isotones as well as to theoretical calculations where available. The observed up-bend in ^{244}Cf was successfully predicted by some of the theoretical calculations. However, the calculations are challenged to correctly describe all of the rotational features in the $N = 146$ isotones due to possible contributions from octupole correlations.

Bibliography

[Abu Saleem04] K. Abu Saleem *et al.* Phys. Rev. C **70**, 024310 (2004). doi:10.1103/PhysRevC.70.024310.

[Afanasjev13] A. V. Afanasjev *et al.* Phys. Rev. C **88**, 014320 (2013). doi:10.1103/PhysRevC.88.014320.

[Agbemava16] S. E. Agbemava *et al.* Phys. Rev. C **93**, 044304 (2016). doi:10.1103/PhysRevC.93.044304.

[Ahmad77] I. Ahmad *et al.* J. Inorg. Nucl. Chem. **39**, 1509 (1977). doi:10.1016/0022-1902(77)80089-4.

[Akovali98] Y. A. Akovali. Nuclear Data Sheets **84**, 1 (1998). doi:10.1006/ndsh.1998.0009.

[Andreyev04] A. N. Andreyev *et al.* Nucl. Inst. Meth. Phys. Res. A **533**, 422 (2004). doi:10.1016/j.nima.2004.07.205.

[Andreyev13] A. N. Andreyev *et al.* Rev. Mod. Phys. **85**, 1541 (2013). doi:10.1103/RevModPhys.85.1541.

[Asaro52] F. Asaro *et al.* Phys. Rev. **87**, 277 (1952). doi:10.1103/PhysRev.87.277.

[Audi03] G. Audi *et al.* Nucl. Phys. A **729**, 337 (2003). doi:10.1016/j.nuclphysa.2003.11.003.

[Bass74] R. Bass. Nucl. Phys. A **231**, 45 (1974). doi:10.1016/0375-9474(74)90292-9.

[Beausang92] C. W. Beausang *et al.* Nucl. Inst. Meth. Phys. Res. A **313**, 37 (1992). doi:10.1016/0168-9002(92)90084-H.

[Bender03] M. Bender *et al.* Nucl. Phys. A **723**, 354 (2003). doi:10.1016/S0375-9474(03)01081-9.

[Berlovich69] E. Ye. Berlovich *et al.* Phys. Lett. B **29**, 155 (1969). doi:10.1016/0370-2693(69)90004-5.

[Bohr39] N. Bohr *et al.* Phys. Rev. **56**, 426 (1939). doi:10.1103/PhysRev.56.426.

[Bohr53] A. Bohr *et al.* Dan. Mat.-Fys. Medd. **27**, No. 16, pp. 1 (1953).

[Browne14] E. Browne *et al.* Nuclear Data Sheets **122**, 293 (2014). doi:10.1016/j.nds.2014.11.003.

[Chatillon06] A. Chatillon *et al.* Eur. Phys. J. A **30**, 397 (2006). doi:10.1140/epja/i2006-10134-5.

[Chetham-Strode56a] A. Chetham-Strode, Jr. Ph.D. thesis, University of California (1956).

[Chetham-Strode56b] A. Chetham-Strode, Jr. *et al.* Phys. Rev. **102**, 747 (1956). doi:10.1103/PhysRev.102.747.

[Delaroche06] J.-P. Delaroche *et al.* Nucl. Phys. A **771**, 103 (2006). doi:10.1016/j.nuclphysa.2006.03.004.

[Devaraja15] H. M. Devaraja *et al.* Phys. Lett. B **748**, 199 (2015). doi:10.1016/j.physletb.2015.07.006.

[Donner66] W. Donner *et al.* Z. Phys. **197**, 440 (1966). doi:10.1007/BF01325911.

[Duchêne99] G. Duchêne *et al.* Nucl. Inst. Meth. Phys. Res. A **432**, 90 (1999). doi:10.1016/S0168-9002(99)00277-6.

[Erler12] J. Erler *et al.* Nature **486**, 509 (2012). doi:10.1038/nature11188.

[Fermi34] E. Fermi. Z. Phys. **88**, 161 (1934). doi:10.1007/BF01351864.

[Fields67] P. R. Fields *et al.* Phys. Lett. **24B**, 340 (1967). doi:10.1016/0370-2693(67)90240-7.

[Firestone96] R. B. Firestone *et al.* Table of Isotopes. John Wiley & Sons, Inc., 8th edition (1996).

[Forsberg16a] U. Forsberg. Ph.D. thesis, Lund University (2016).

[Forsberg16b] U. Forsberg *et al.* Nucl. Phys. A **953**, 117 (2016). doi:10.1016/j.nuclphysa.2016.04.025.

[Fry13] C. Fry *et al.* Atomic Data and Nuclear Data Tables **99**, 96 (2013). doi:10.1016/j.adt.2012.04.001.

[Galeriu83] D. Galeriu. J. Phys. G. Nucl. Phys. **9**, 309 (1983). doi:10.1088/0305-4616/9/3/011.

[Gallagher58] C. J. Gallagher *et al.* Phys. Rev. **111**, 1282 (1958). doi:10.1103/PhysRev.111.1282.

[Gamow28] G. Gamow. Z. Phys. **51**, 204 (1928). doi:10.1007/BF01343196.

[Gamow30] G. Gamow. Proc. R. Soc. Lond. A **126**, 632 (1930). doi:10.1098/rspa.1930.0032.

[Geiger11] H. Geiger *et al.* Philosophical Magazine **22**, 613 (1911). doi:10.1080/14786441008637156.

[Georgiev93] A. Georgiev *et al.* IEEE Trans. Nucl. Sci **40**, 770 (1993). doi:10.1109/23.256659.

[Ghiorso54] A. Ghiorso *et al.* Phys. Rev. **93**, 257 (1954). doi:10.1103/PhysRev.93.257.

[Ghiorso55] A. Ghiorso *et al.* Phys. Rev. **99**, 1048 (1955). doi:10.1103/PhysRev.99.1048.

[Ghys15] L. Ghys *et al.* Phys. Rev. C **91**, 044314 (2015). doi:10.1103/PhysRevC.91.044314.

[Greenlees12] P. T. Greenlees *et al.* Phys. Rev. Lett. **109**, 012501 (2012). doi:10.1103/PhysRevLett.109.012501.

[Gurney28] R. W. Gurney *et al.* Nature (London) **122**, 439 (1928). doi:10.1038/122439a0.

[Hackman98] G. Hackman *et al.* Phys. Rev. C **57**, R1056 (1998). doi:10.1103/PhysRevC.57.R1056.

[Hahn38] O. Hahn *et al.* Die Naturwissenschaften **26**, 755 (1938).

[Hahn39] O. Hahn *et al.* Die Naturwissenschaften **27**, 11 (1939).

[Hall90a] H. L. Hall *et al.* Phys. Rev. C **42**, 1480 (1990). doi:10.1103/PhysRevC.42.1480.

[Hall90b] H. L. Hall *et al.* Phys. Rev. C **41**, 618 (1990). doi:10.1103/PhysRevC.41.618.

[Harris65] S. M. Harris. Phys. Rev. **138**, B509 (1965). doi:10.1103/PhysRev.138.B509.

[Häusser82] O. Häusser *et al.* Phys. Rev. Lett. **48**, 383 (1982). doi:10.1103/PhysRevLett.48.383.

[Haxel49] O. Haxel *et al.* Phys. Rev. **75**, 1766 (1949). doi:10.1103/PhysRev.75.1766.2.

[Herzberg01] R.-D. Herzberg *et al.* Phys. Rev. C **65**, 014303 (2001). doi:10.1103/PhysRevC.65.014303.

[Herzberg08] R.-D. Herzberg *et al.* Prog. Part. Nucl. Phys. **61**, 674 (2008). doi:10.1016/j.ppnp.2008.05.003.

[Heßberger17] F. P. Heßberger. Eur. Phys. J. **A53**, 75 (2017). doi:10.1140/epja/i2017-12260-3.

[Heyde04] K. Heyde. Basic Ideas and Concepts in Nuclear Physics, An Introductory Approach. Taylor & Francis (2004).

[Hoffman89] D. C. Hoffman. Nucl. Phys. A **502**, 21c (1989). doi:10.1016/0375-9474(89)90652-0.

[Hota14] S. S. Hota *et al.* Phys. Lett. B **739**, 13 (2014). doi:10.1016/j.physletb.2014.10.021.

[Hulme32] H. R. Hulme. Proc. Roy. Soc. A **138**, 643 (1932). doi:10.1098/rspa.1932.0208.

[Hurst10] A. M. Hurst *et al.* Phys. Rev. C **81**, 014312 (2010). doi:10.1103/PhysRevC.81.014312.

[Kaji16] D. Kaji *et al.* J. Phys. Soc. Japan **85**, 015002 (2016). doi:10.7566/JPSJ.85.015002.

[Kantele95] J. Kantele. The Handbook of Nuclear Spectrometry. Academic Press Limited, London, UK (1995).

[Ketelhut10] S. Ketelhut. Ph.D. thesis, University of Jyväskylä (2010).

[Khuyagbaatar10] J. Khuyagbaatar *et al.* Eur. Phys. J. A **46**, 59 (2010). doi:10.1140/epja/i2010-11026-9.

[Kibédi08] T. Kibédi *et al.* Nucl. Inst. Meth. Phys. Res. A **589**, 202 (2008). doi:10.1016/j.nima.2008.02.051. `http://bricc.anu.edu.au/`.

[Krane88] K. S. Krane. Introductory Nuclear Physics. John Wiley & Sons (1988).

[Kreek94] S. A. Kreek *et al.* Phys. Rev. C **49**, 1859 (1994). doi:10.1103/PhysRevC.49.1859.

[Kuznetsov99] V. I. Kuznetsov *et al.* Physics of Particles and Nuclei **30**, 666 (1999). doi:10.1134/1.953123.

[Laue00] C. A. Laue *et al.* Phys. Rev. C **61**, 067603 (2000). doi:10.1103/PhysRevC.61.067603.

[Lazarev95] Yu. A. Lazarev *et al.* Nucl. Phys. A **588**, 501 (1995). doi:10.1016/0375-9474(95)00002-I.

[Lazarus01] I. H. Lazarus *et al.* IEEE Trans. Nucl. Sci **48**, 567 (2001). doi:10.1109/23.940120.

[Leino81] M. Leino *et al.* Phys. Rev. C **24**, 2370 (1981). doi:10.1103/PhysRevC.24.2370.

[Leino95] M. Leino *et al.* Nucl. Inst. Meth. Phys. Res. B **99**, 653 (1995). doi:10.1016/0168-583X(94)00573-7.

[Liu12] H. L. Liu *et al.* Phys. Rev. C **86**, 011301 (2012). doi:10.1103/PhysRevC.86.011301.

[Liukkonen92] E. Liukkonen. In 13th Int. Conf. on Cyclotrons, Vancouver, 22–27 (1992).

[Mayer49] M. G. Mayer. Phys. Rev. **75**, 1969 (1949). doi:10.1103/PhysRev.75.1969.

[Meierfrankenfeld11] D. Meierfrankenfeld *et al.* Atomic Data and Nuclear Data Tables **97**, 134 (2011). doi:10.1016/j.adt.2010.11.001.

[Meitner39] L. Meitner *et al.* Nature **143**, 239 (1939). doi:10.1038/143471a0.

[Metta69] D. N. Metta *et al.* J. Inorg. Nucl. Chem. **31**, 1245 (1969). doi:10.1016/0022-1902(69)80235-6.

[Milsted65] J. Milsted *et al.* Nucl. Phys. **71**, 299 (1965). doi:10.1016/0029-5582(65)90719-4.

[Möller97] P. Möller *et al.* Atomic Data and Nuclear Data Tables **66**, 131 (1997). doi:10.1006/adnd.1997.0746.

[Möller09] P. Möller *et al.* Phys. Rev. C **79**, 064304 (2009). doi:10.1103/PhysRevC.79.064304.

[Möller15] P. Möller *et al.* Phys. Rev. C **91**, 024310 (2015). doi:10.1103/PhysRevC.91.024310.

[Möller16] P. Möller *et al.* Atomic Data and Nuclear Data Tables **109–110**, 1 (2016). doi:10.1016/j.adt.2015.10.002.

[Myers69] W. D. Myers *et al.* Annals of Physics **55**, 395 (1969). doi:10.1016/0003-4916(69)90202-4.

[Nesaraja14] C. D. Nesaraja *et al.* Nuclear Data Sheets **121**, 695 (2014). doi:10.1016/j.nds.2014.09.005.

[Nilsson55] S. G. Nilsson. Dan. Mat.-Fys. Medd. **29**, No. 16 (1955).

[Nilsson95] S. G. Nilsson *et al.* Shapes and Shells in Nuclear Structure. Cambridge University Press, Cambridge, UK (1995).

[Ninov96] V. Ninov *et al.* Z. Phys. A **356**, 11 (1996). doi:10.1007/s002180050141.

[Öhrström16] L. Öhrström *et al.* Pure and Applied Chemistry **88**, 1225 (2016). doi:10.1515/pac-2016-0501.

[Page03] R. D. Page *et al.* Nucl. Inst. Meth. Phys. Res. B **204**, 634 (2003). doi:10.1016/S0168-583X(02)02143-2.

[Parkhomenko04] A. Parkhomenko *et al.* Acta Phys. Pol. B **35**, 2447 (2004).

[Paul95] E. S. Paul *et al.* Phys. Rev. C **51**, 78 (1995). doi:10.1103/PhysRevC.51.78.

[Piot] J. Piot. Private communication.

[Piot12] J. Piot *et al.* Phys. Rev. C **85**, 041301(R) (2012). doi:10.1103/PhysRevC.85.041301.

[Pomorski73] K. Pomorski *et al.* Nucl. Phys. A **205**, 433 (1973). doi:10.1016/0375-9474(73)90698-2.

[Qi14] C. Qi *et al.* Phys. Lett. B **734**, 203 (2014). doi:10.1016/j.physletb.2014.05.066.

[Qin08] Z. Qin *et al.* Radiochimica Acta **96**, 455 (2008). doi:10.1524/ract.2008.1517.

[Radford95a] D. C. Radford. Nucl. Inst. Meth. Phys. Res. A **361**, 306 (1995). doi:10.1016/0168-9002(95)00184-0.

[Radford95b] D. C. Radford. Nucl. Inst. Meth. Phys. Res. A **361**, 297 (1995). doi:10.1016/0168-9002(95)00183-2.

[Rahkila08] P. Rahkila. Nucl. Inst. Meth. Phys. Res. A **595**, 637 (2008). doi:10.1016/j.nima.2008.08.039.

[Rasmussen59] J. O. Rasmussen. Phys. Rev. **113**, 1593 (1959). doi:10.1103/PhysRev.113.1593.

[Reisdorf81] W. Reisdorf *et al.* Z. Phys. A **300**, 227 (1981). doi:10.1007/BF01412298.

[Rossi Alvarez93] C. Rossi Alvarez. Nuclear Physics News **3**, 10 (1993). doi:10.1080/10506899308221154.

[Rudolph16] D. Rudolph *et al.* EPJ Web of Conferences **117**, 01001 (2016). doi:10.1051/epjconf/201611701001.

[Sarén] J. Sarén. Private communication.

[Sarén11] J. Sarén *et al.* Nucl. Inst. Meth. Phys. Res. A **654**, 508 (2011). doi:10.1016/j.nima.2011.06.068.

[Schmidt84] K.-H. Schmidt *et al.* Z. Phys. A **316**, 19 (1984). doi:10.1007/BF01415656.

[Schmidt86] K.-H. Schmidt *et al.* Phys. Lett. B **168**, 39 (1986). doi:10.1016/0370-2693(86)91456-5.

[Schmidt00] K. H. Schmidt. Eur. Phys. J. A **8**, 141 (2000). doi:10.1007/s100500070129.

[Shaughnessy00] D. A. Shaughnessy *et al.* Phys. Rev. C **61**, 044609 (2000). doi:10.1103/PhysRevC.61.044609.

[Shaughnessy01] D. A. Shaughnessy *et al.* Phys. Rev. C **63**, 037603 (2001). doi:10.1103/PhysRevC.63.037603.

[Shaughnessy02] D. A. Shaughnessy *et al.* Phys. Rev. C **65**, 024612 (2002). doi:10.1103/PhysRevC.65.024612.

[Shi14] Y. Shi *et al.* Phys. Rev. C **89**, 034309 (2014). doi:10.1103/PhysRevC.89.034309.

[Sikkeland67a] T. Sikkeland *et al.* Phys. Lett. **24B**, 333 (1967). doi:10.1016/0370-2693(67)90236-5.

[Sikkeland67b] T. Sikkeland *et al.* Phys. Lett. **24B**, 331 (1967). doi:10.1016/0370-2693(67)90235-3.

[Silva70] R. J. Silva *et al.* Phys. Rev. C **2**, 1948 (1970). doi:10.1103/PhysRevC.2.1948.

[Simon86] R. S. Simon *et al.* Z Phys. A **325**, 197 (1986). doi:10.1007/BF01289651.

[Singh08] B. Singh *et al.* Nuclear Data Sheets **109**, 2439 (2008). doi:10.1016/j.nds.2008.09.002.

[Sobiczewski01] A. Sobiczewski *et al.* Phys. Rev. C **63**, 034306 (2001). doi:10.1103/PhysRevC.63.034306.

[Strutinsky67] V. M. Strutinsky. Nucl. Phys. A **95**, 420 (1967). doi:10.1016/0375-9474(67)90510-6.

[Sulignano12] B. Sulignano *et al.* Phys. Rev. C **86**, 044318 (2012). doi:10.1103/PhysRevC.86.044318.

[Tarasov04] O. B. Tarasov *et al.* Nucl. Phys. A **746**, 411c (2004). doi:10.1016/j.nuclphysa.2004.09.063. http://lise.nscl.msu.edu/.

[Theisen15] Ch. Theisen *et al.* Nucl. Phys. A **944**, 333 (2015). doi:10.1016/j.nuclphysa.2015.07.014.

[Thoennessen11] M. Thoennessen *et al.* Nature **473**, 25 (2011). doi:10.1038/473025a.

[Thompson50a] S. G. Thompson *et al.* Phys. Rev. **77**, 838 (1950). doi:10.1103/PhysRev.77.838.2.

[Thompson50b] S. G. Thompson *et al.* Phys. Rev. **78**, 298 (1950). doi:10.1103/PhysRev.78.298.2.

[Thompson50c] S. G. Thompson *et al.* Phys. Rev. **80**, 781 (1950). doi:10.1103/PhysRev.80.781.

[Thompson50d] S. G. Thompson *et al.* Phys. Rev. **80**, 790 (1950). doi:10.1103/PhysRev.80.790.

[Thompson54] S. G. Thompson *et al.* Phys. Rev. **93**, 908 (1954). doi:10.1103/PhysRev.93.908.

[Vandenbosch73] R. Vandenbosch *et al.* Nuclear Fission. Academic Press (1973). doi:10.1016/B978-0-12-710850-6.50001-0.

[Veselský12] M. Veselský *et al.* Phys. Rev. C **86**, 024308 (2012). doi:10.1103/PhysRevC.86.024308.

[Wang09] X. Wang *et al.* Phys. Rev. Lett. **102**, 122501 (2009). doi:10.1103/PhysRevLett.102.122501.

[Ward96] D. Ward *et al.* Nucl. Phys. A **600**, 88 (1996). doi:10.1016/0375-9474(95)00490-4.

[Weisskopf51] V. F. Weisskopf. Phys. Rev. **83**, 1073 (1951). doi:10.1103/PhysRev.83.1073.

[Weizsäcker35] C. F. v. Weizsäcker. Z. Phys. **96**, 431 (1935). doi:10.1007/BF01337700.

[Wiedenhöver99] I. Wiedenhöver *et al.* Phys. Rev. Lett. **83**, 2143 (1999). doi:10.1103/PhysRevLett.83.2143.

[Wilson17] G. L. Wilson *et al.* Phys. Rev. C **96**, 044315 (2017). doi:10.1103/PhysRevC.96.044315.

[Wu92a] C. S. Wu *et al.* Phys. Rev. C **45**, 2507 (1992). doi:10.1103/PhysRevC.45.2507.

[Wu92b] C. S. Wu *et al.* Phys. Rev. C **45**, 261 (1992). doi:10.1103/PhysRevC.45.261.

[Zhang12] Z.-H. Zhang *et al.* Phys. Rev. C **85**, 014324 (2012). doi:10.1103/PhysRevC.85.014324.

[Zhu10] S. Zhu *et al.* Phys. Rev. C **81**, 041306(R) (2010). doi:10.1103/PhysRevC.81.041306.